UC Berkeley

Title

Synchrotron techniques for studying microstructure in geologic materials

Permalink

https://escholarship.org/uc/item/20f9149b

Author

Devoe, Michelle

Publication Date

2024

Synchrotron techniques for studying microstructure in geologic materials

by

Michelle Cyr Devoe

A dissertation submitted in partial satisfaction of the

requirements for the degree of

Doctor of Philosophy

in

Earth and Planetary Science

in the

Graduate Division

of the

University of California, Berkeley

Committee in charge:

Professor Hans-Rudolf Wenk, Chair
Professor Jill Banfield
Professor Andrew Minor

Spring 2024

Synchrotron techniques for studying microstructure in geologic materials

Abstract

Synchrotron techniques for studying microstructure in geologic materials

by

Michelle Cyr Devoe

Doctor of Philosophy in Earth and Planetary Science

University of California, Berkeley

Professor Hans-Rudolf Wenk, Chair

With the advent of x-rays in the late 1800s and crystal x-ray diffraction in the early 1900s, the field of crystallography took off and by now, the crystal structures of most minerals have been well-characterized. When subjected to stress, the response of the crystal is dependent upon the material properties. When an aggregate of randomly oriented anisotropic crystals is subjected to a differential stress, crystallographic preferred orientation can develop. Seismic anisotropy detected in areas of high deformation, such as proximal to subducting slabs and along the core-mantle boundary, has been attributed to the development of crystallographic preferred orientation (CPO), a process in which anisotropic crystals rotate into a similar alignment in response to differential stress, creating an anisotropic bulk aggregate. Stress can also distort the crystal lattice by creating defects in the lattice, such as point defects and dislocations, which create areas of localized elastic strain surrounding the defect. The orientation of the macrostress may affect the residual strain in the crystal lattice. And the evolution of this plasticity around a feature, such as a fracture, can provide information regarding fracture mechanics of the material, how the material responds to a free surface, and elucidate healing mechanics. In this dissertation, three experiments studying microstructure in geologic materials using synchrotron x-rays and their implications for Earth's systems are explored.

In Chapter 1, the texture development of high-pressure hydrous trigonal phase D [$MgSi_2O_4(OH)_2$], monoclinic phase Egg [$AlSiO_3(OH)$], and orthorhombic δ-AlO(OH) are investigated using radial diamond anvil cell (DAC) x-ray diffraction. Phase D, synthesized from serpentine, developed an (001) maximum of 7.4 m.r.d, indicating basal slip, and aligning the basal planes perpendicular to the principal axis of compression. Phase Egg, synthesized from kaolinite, developed a strong (001) maximum of 10.3 m.r.d., also indicative of basal slip as the primary deformation mechanism. δ-AlO(OH) developed an (010) maximum of 3.0 m.r.d. parallel to the compression direction. For all phases, the sheet-like planes aligned themselves perpendicular to the compression axis. Visoplastic self-consistent polycrystal

plasticity modeling confirmed that (001) slip in phase D at 50% strain produces a texture very similar to the texture observed in the deformed aggregate. The hydrous phases investigated here have P-wave anisotropy and shear-wave splitting values comparable or greater than other mantle phases. The stiffness coefficients of deformed bulk aggregate were also calculated.

In Chapter 2, scanning Laue microdiffraction is used to measure the residual strain in thin sections of natural and experimentally deformed quartzites from which the paleostress orientation is inferred. Samples with low levels of plastic deformation, which possess small, uniform diffraction peak shape return principal strain orientations reasonable with the known or expected deformation conditions, such as a vein quartzite from a hydrothermal structure in Hong Kong (HSM), showing the principal axis of compression perpendicular to the long axes of the grains, and rolled Ti, which shows the principal axis of compression parallel to the normal direction and principal axis of extension parallel to the rolling direction. In samples with high levels of plastic deformation, such as quartzite from a hydrothermal explosion structure in Hong Kong (Ko1) or quartzite deformed in a piston apparatus (H2), the principal strain axes of compression and extension show two maxima oriented along the vertical axis inclined at 45° to the Z-direction. This strain pattern, seen across four different rock samples, is believed to be an artifact that results from the inability to detect subpixel shifts in the peak position due to the non-Gaussian intensity distribution of the peak shape. However, the source of this exact strain pattern remains a point of investigation.

In Chapter 3, scanning Laue microdiffraction is used to measure the elastic strain around a Mode I crack along (10-14) in a slice of calcite in a time series of three consecutive scans over the course of 44 hours following load removal. An increasingly compressive strain perpendicular to the fracture surface that migrates and accumulates around the crack plane is observed. Correspondingly, an increasingly tensile strain coplanar to the fracture surface is also observed. Peak broadening is recorded in the areas showing high strain. This suggests the movement of plasticity such as defects toward the fracture surface over time, in addition to the increased compressive strain perpendicular to the crack plane with relaxation of the bulk of the crystal, indicative of healing. The orientation of common low-temperature glide planes $\mathbf{r}$ = {10-14} <20-2-1> and $\mathbf{f}$ = {-1012} <0-22-1> systems, and twinning on $\mathbf{e}$ = {-1018} <40-41> in calcite are oriented to intersect with the crack along (10-14) and could facilitate such movement.

This dissertation is dedicated to my family.
"Not knowing when the Dawn will come,
I open every Door,
Or has it Feathers, like a Bird,
Or Billows, like a Shore" —
— Emily Dickinson (1896)

Contents

Acknowledgments

There are numerous people I would like to thank for helping this dream become a reality.

Firstly, my family. Thank you for your unconditional love and support. Without your encouragement, I would not have even applied to Berkeley. Thanks for keeping me on the game board and showing me which way was up when I was upside down, and for always helping me see the light.

Rudy. Thank you for your faith in me, your guidance, wisdom, compassion, and critique. You have made me a better scientist, critical thinker, writer, and human being. Thank you for being always available, engaged, and kind over the past five years. I'm excited to see what you will discover next. As you say, "It never ends!"

Beamline scientists Nobumichi Tamura, Martin Kunz, Kat Armstrong, and Bora Kalkan. Thank you for answering my numerous, never-ending (sometimes repeat!) questions about the beamline, diffraction, and troubleshooting. It is at the ALS and with your support I have developed beneficial critical thinking, troubleshooting, and research skills as an experimentalist. The ALS became a second home for me during my PhD where I made many friendships and learned a lot. I was able to make mistakes and ask questions. I have grown so much while on the ALS grounds, it has been an incredible opportunity and experience to learn from you. Thank you for your support.

Erik Rybacki for your help performing the deformation of the quartzites using the Paterson apparatus. Data from these experimentally deformed samples were key to understanding the strain artifacts.

Harry Lisabeth and Seiji Nakagawa for introducing me to fracture mechanics, your collaboration, and your help with how to lead a smart experiment.

Lung Chan for your support and the use of the Hong Kong quartzites which were key examples for demonstrating the capability and limitation of scanning Laue microdiffraction for measuring residual strain.

Kai Chen and Yao Li and Jiawei Kou for your help with XtalCAMP, and now with PYXIS on how to best measure the strain in complex samples.

Jill Banfield. Jill, you are an inspiration to me. Thank you for your mentorship and guidance, and for your time serving on my committee.

Andy Minor for introducing me to the world of materials characterization and for taking the time to serve on my committee.

John Grimsich for your help with not only the SEM, thin section making, powder XRD, but also with troubleshooting all other mechanical things, like how to shave off a piece of Zr, how to unstuck a bike lock, and knowing the best spots to explore in the Sierras. You are truly a treasure trove of knowledge and the department is lucky to have you.

Kristin Bennett for your friendship and advice on life after PhD, careers, and generally being an inspirational human and corporate woman in science.

Next, my friends. So many friends I can't list them all here. But you all have made my time here significant and treasured. It is through conversations, time spent, adventures

shared with you that I've formed deep friendships, learned new skills, shared humor. I'm so grateful for all of you for making my time here in the East Bay meaningful and significant.

Also I'd like to thank Krissy Moehl, my running coach, who showed me how to get strong in my body which has empowered me to feel confident and capable, and has had a trickle-down effect to all other areas of my life. And my therapist Ethan for teaching me how to keep my boat steady when the waves get rough.

It takes a village! I'm so grateful to all of you. Thank you.

Chapter 1

Introduction

1.1 Background

The discovery of x-ray diffraction by a crystal in 1912 by Laue, Friedrich, and Knipping clarified two things: that crystals possess a periodic array of atoms, or Bravais space lattice, and the wavelength of x-rays is similar to the period of lattice spacing (Friedrich et al., 1912; Laue, 1920). These two properties combined allow for x-rays to be used to study the structure of crystals. Following this discovery, the field of crystallography took off, and now over 100 years later, the crystal structures of most minerals have been well-characterized. The fundamental understanding that each crystal has a regular, periodic array of atoms makes it such that deviation in the predicated atomic spacing indicates strain in the lattice, which can be caused by vacancies, interstitial ions, and stress-induced dislocations, for example. When a crystal or an aggregate of crystals is subjected to stress, deformation can occur and create microstructures: microscopic structures in a crystal lattice or in an aggregate of crystals that result from stress. The crystal's response to stress can be studied using x-rays.

1.2 Texture

Under high pressure and temperature conditions, an aggregate of anisotropic crystals subjected to differential stress can develop crystallographic preferred orientation (CPO) (i.e. texture). Strain can be accommodated by diffusion or by the movement of dislocations along crystal planes called "slip." Slip causes the crystals to rotate, and with enough time and stress, CPO develops if enough single crystals rotate into a similar alignment relative to the direction of differential stress (Taylor, 1934a, 1934b). An aggregate of randomly oriented anisotropic crystals (i.e. "grains") behaves isotropically, however when CPO develops, the aggregate becomes elastically anisotropic which means a seismic wave's interaction with the aggregate is direction-dependent. Since the 1960s, our understanding of the Earth has evolved from a simple layered structure comprised of isotropic layers with lateral heterogeneities to now consider a seismically anisotropic lithosphere, transition zone, mantle, and

even inner core (e.g. Montagner, 1998).

CPO develops in areas of high deformation with a direction of flow and associated differential stress, including adjacent to plumes of mantle convection, along a subducting slab, and along the core-mantle boundary (e.g. Long and Silver, 2008; Chandler et al., 2021b; Tsujino et al., 2016). Seismic anisotropy near subducting slabs in the transition zone, the region of the asthenosphere demarcated by the seismic discontinuities that occur at 410 km and 660 km due to the phase transformations from olivine to wadsleyite and ringwoodite and then to bridgmanite, respectively, (e.g. Jeanloz and Thompson, 1983; Ita and Stixrude, 1992; Helffrich, 2000) has been attributed to the development of texture along the downgoing slab (Van der Lee and Nolet, 1997; Long, 2013).

The deformation of mantle minerals including their tendency to develop texture and the deformation mechanisms responsible for their alignment during deformation, are investigated theoretically using atomistic-scale modeling (e.g. Goryaeva et al., 2016, 2017), and experimentally using high pressure experiments (e.g. Raleigh, 1968, Kohlstedt and Goetze, 1974, Wenk et al., 2004, Merkel and Yagi, 2005, Merkel et al., 2006, Miyagi et al., 2010, Wenk et al., 2011, Miyagi and Wenk, 2016).

Synchrotron x-ray diffraction using a diamond anvil cell (DAC) in radial geometry is a well-established technique to study the mechanical properties of minerals at very high pressures and temperatures (e.g Wenk et al., 2000, 2006a). A polycrystalline sample is loaded into an x-ray transparent gasket (Merkel & Yagi, 2005), which imposes confining pressure, between two diamonds that also exert an axial compressive stress on the sample (Merkel et al., 2000). The DAC is loaded into the x-ray beam such that the beam is perpendicular to the loading axis, as opposed to axial geometry in which the x-ray beam is parallel to the loading axis. An x-ray beam with high enough energy and flux to penetrate the thickness of the sample and gasket is necessary to produce a detectable signal, which is why synchrotron diffraction is useful for this experiment, in addition to rapidity of data acquisition enabled by the synchrotron method. Stress imposed on the sample by the diamond anvils causes the crystals to deform. The intersection of the detector and the cone of diffraction produced from crystal planes in the deformed aggregate that satisfy the Bragg condition (Bragg, 1913; Bragg & Bragg, 1913) produce Debye rings in a diffraction pattern. Kinsland and Bassett, 1975 described how to use the ellipticity of the Debye diffraction rings to calculate strength of the material (Singh et al., 1998). And azimuthal intensity variations along a Debye ring are indicative of preferred orientation. The orientation distribution function describing the distribution of crystal planes relative to the stress is calculated using Rietveld refinement (Lutterotti et al., 2014; Wenk et al., 2014) and the deformation mechanisms are modeled using viscoplastic self-consistent modeling (Lebensohn & Tomé, 1993). The deformation mechanisms are then incorporated into geodynamic models to approach a more realistic system of deformation paths (e.g. Dawson and Wenk, 2000; Blackman et al., 2002; Chandler et al., 2021b.

However, mainly the deformation behavior of anhydrous phases belonging to a pyrolitic mantle model have been studied experimentally when already in the 1960s, anisotropic hydrous phases stable in the transition zone were synthesized (Ringwood and Major, 1967;

Eggleton et al., 1978; Liu, 1986). Volumetric estimates of hydrous phases remain sparse. One estimate suggests phase D could comprise up to 64% of a fully-saturated peridotite (Iwamori, 2004) and thus could contribute significantly to the anisotropy in the transition zone. Chapter 2 presents the results on the deformation of hydrous phases in a diamond anvil cell and their potential contribution to transition zone seismic anisotropy.

1.3   Residual strain and paleostress

Stress can induce plastic deformation, introducing defects and activate slip systems, which distort the lattice and cause changes to interplanar spacings. Residual strain, the areas of localized compression and tension around dislocations in a lattice that remain even after the macrostress has been removed, has been has been of interest to material scientists for decades as it affects the strength of materials (Noyan & Cohen, 1987). Residual strain can be measured with destructive methods such as the hole-drilling method, where the dimensional changes of an object are measured after a piece of it has been removed (e.g. Noyan & Cohen, 1987), focused ion beam (FIB) milling (e.g. Lunt & Korsunsky, 2015), and non-destructive methods such as neutron diffraction (e.g. Withers & Webster, 2001), x-ray diffraction peak broadening (Ungar et al., 2001), and electron backscatter diffraction (EBSD) (e.g. Britton & Wilkinson, 2011).

Here residual strain has been measured using synchrotron Laue (polychromatic) microdiffraction and attributed to the stress history. Starting in 2009, Kunz et al. measured the strain in the lattice of minerals in granite sampled proximal to a mylonite shear zone and estimated the magnitude of the stress responsible to cause such a distortion. Then, Chen et al. (2016) used Laue microdiffraction to settle a long-standing debate about the origin of the boudinage structure in Bastogne, Belgium by determining the orientation of the paleostress using and Eigen decomposition of the deviatoric strain tensor. Wenk et al. (2020) have demonstrated the capability of the methodology to determine the orientation of paleostress using foliated quartzites from the Bergell Alps, the orientation of principal compression known to be perpendicular to the foliation plane.

Compared to radial DAC studies, which can measure the stress in the deformed bulk aggregate, scanning Laue microdiffraction is used to generate high-resolution strain maps over several grains and can associate strain with an individual grain to visualize intergranular and intragranular strain gradients.

In scanning Laue microdiffraction, a polychromatic x-ray beam is used to satisfy the Laue condition. A standard thin section (30 µm thick) is used as a sample, mounted on a translational stage inclined 45° to the incident beam, directly below the detector. A small area (millimeters) is programmed, and the stage translates to raster the sample across the x-ray beam in a step-wise fashion. A Laue diffraction image is captured at each step, where each Bragg reflection is associated with a crystal plane. Distortions of the crystal lattice are calculated from the relative deviations of the Bragg reflections compared to an unstrained lattice, and are used to calculate the deviatoric strain tensor. An Eigen decomposition is

used to determine the principal strain orientations and magnitudes. This information is then portrayed spatially by displaying the data from each step as a single pixel on the map (Tamura et al., 2003; Tamura, 2014; Li et al., 2020). Principal strain orientations are then viewed in the aggregate by plotting the strain axes on pole figures in sample coordinates (Wenk et al., 2020).

In scanning Laue microdiffraction, strain is measured based on the relative peak positions on the diffraction pattern, which is related to the elastic strain, or the distortion of the crystal lattice. Plastic deformation in the sample manifests as broadening and distortion of peak shape (e.g. Barabash et al., 2003). Because the deviatoric strain tensor is related to the peak positions, the presence of plastic strain can complicate the measurement of strain in the crystal lattice. In Chapter 3, scanning Laue microdiffraction data is presented for quartzites from variable deformation environments and discrepancies caused by the plastic strain in the sample are discussed.

1.4 Residual strain and crack healing in calcite

Crack mechanics in calcite is of interest due to its relevance in controlling permeability, fluid-transport, sediment compaction in hydrocarbon basins and geothermal reservoirs (Royne et al., 2011; McNamara et al., 2016), as well as fault evolution in seismically active areas (Marone et al., 1995). Understanding crack propagation and closure is critical in controlling mineralization and predicting seismic risk in these environments, yet crack mechanics of calcite ($CaCO_3$) are not well understood.

Several methods exist to study the residual strain fields around cracks in metals and alloys including destructive methods like strain gauges (Irwin, 1957) in which a hole is punched out and the dimensional change in shape of the material is measured. Neutron diffraction (Hutchings et al., 1990) and now synchrotron x-ray diffraction and microscopy (Steuwer & Daniels, 2011; Withers, 2015) have also been used to measure the magnitude and spatially reconstruct the strain field surrounding cracks.

In Chapter 4, I discuss how I used scanning Laue microdiffraction is used to measure the strain field in-situ surrounding a crack in a slide of calcite. The experimental geometry used to measure residual elastic strain in thin section is modified to suit the measurement of residual strain around a planar feature (fracture plane). To remove asymmetrical sampling of the planar feature due to the 45° angle of incidence, the slide is oriented 90° to the incident beam to ensure the planar feature is probed equivalently over the scan dimensions. The data from three scans of the cracktip area are collected immediately following load removal, spanning the course of 44 hours, to observe the evolution of healing at the cracktip area.

1.5 Conclusion

The minerals that comprise the Earth develop microstructures in response to stress. In this dissertation, I will explore a variety of microstructures, including deformation textures of hydrous high-pressure Mg and Al silicates, plasticity in calcite, and residual strain in quartz, using synchrotron x-ray diffraction techniques to further our understanding of how these systems respond to stress, the techniques that can be used to study these microstructures, and the implications of the microstructures in context.

Chapter 2

Deformation of hydrous mantle phases

2.1 Introduction

Seismic tomography has illuminated the structures of the mantle, such as the subducted Farallon plate beneath North America (Van der Lee & Nolet, 1997), and large low shear velocity provinces (LLSVP) beneath the Pacific (Madrigal et al., 2016) and the African plates (Wang & Wen, 2007). It also has illustrated the heterogeneous nature of the mantle, and particularly the transition zone, between 410-660 km depth, with significant P and S-wave velocity variability (Van der Lee & Nolet, 1997) and local anisotropy (Wookey et al., 2002; Long, 2013). Anisotropy in the mantle has been attributed to the development of crystallographic preferred orientation (CPO). CPO, or texture, develops through the rotation of anisotropic single crystals into a similar, low-energy alignment relative to the direction of differential stress such as slab subduction and mantle convection, results in an anisotropic bulk aggregate (e.g. Blackman et al., 1996; Dawson and Wenk, 2000; Blackman et al., 2002; Wenk et al., 2006b; Wenk et al., 2011; Chandler et al., 2021b). The strong seismic anisotropy that is likely due to CPO is present in subduction zones (e.g. Currie et al., 2004; Long and van der Hilst, 2006; Long and Silver, 2008), and at the core-mantle boundary (e.g. Panning & Romanowicz, 2006), for example.

Studies on texture development in the mantle have focused on the anhydrous components of a pyrolitic mantle, namely olivine, ringwoodite, wadsleyite, bridgmanite, ferropericlase and post-perovskite (e.g. Wenk et al., 2004; Merkel et al., 2006; Miyagi et al., 2010; Girard et al., 2016; Miyagi and Wenk, 2016; Chandler et al., 2021a). However, the discovery of high pressure hydrous magnesium silicates like phase D [$MgSi_2O_4(OH)_2$] (Fig. 2.1a) (Liu, 1986) and aluminum silicates like phase Egg [$AlSiO_3(OH)$] (Fig. 2.1b) (Eggleton et al., 1978) in the 1960s and 1970s, and later δ-AlO(OH) (Fig. 2.1c) (Suzuki et al., 2000), has demonstrated the stability of hydrous phases at mantle conditions. If the components of the mantle were entirely saturated, it has been estimated that phase D could comprise up to 63% of the mantle (Iwamori, 2004). The true volumetric percentage would be be much lower because most the mantle is under-saturated, but could still significantly influence mantle anisotropy.
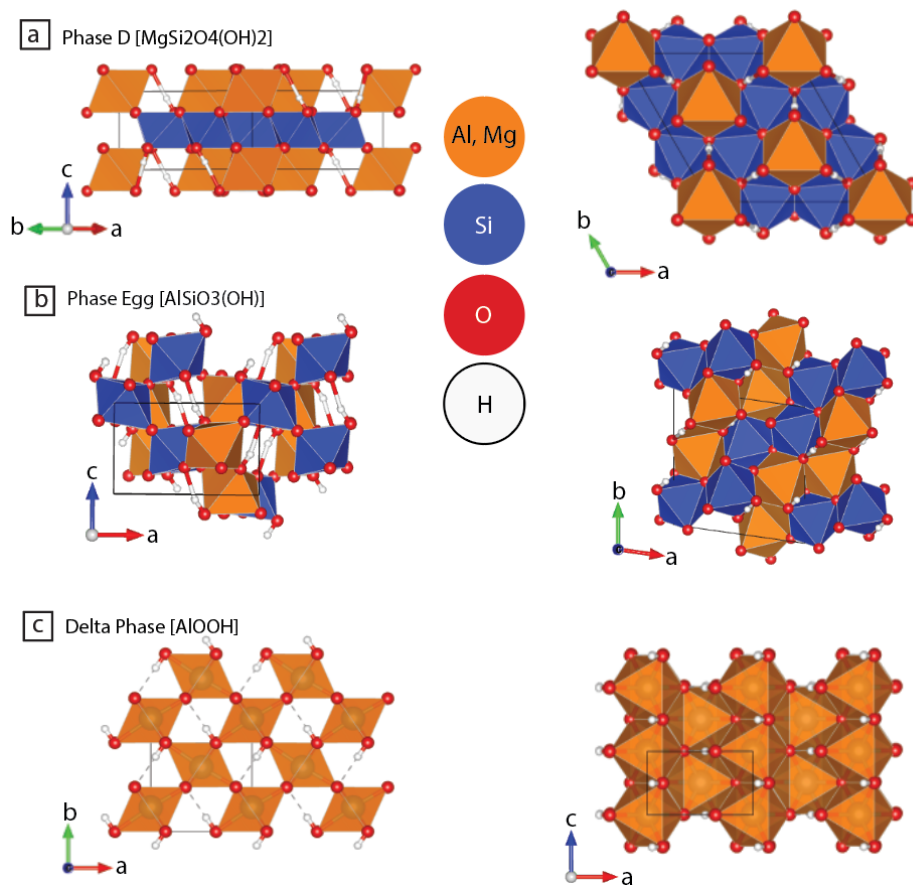
Figure 2.1: *Polyhedral crystal structure models of phases (a) D, (b) Egg, and (c) δ-AlO(OH).*

Phase D, formed from high pressure and temperature transformation of serpentine, is a trigonal Mg silicate containing alternating layers of SiO_6 octahedra stacked along the c-axis, alternating with a single layer of $Mg(O,OH)_6$ octahedra. $Mg(O,OH)_6$ octahedra occupy one third of the octahedral sites, placed in the center of the Si octahedral ring. O-H-O bonds form between Mg octahedra of a single layer (Yang et al., 1997) (Fig. 2.1a). Here I use the triple cell (P-3m), with lattice parameters a=7.9708 Å and c=4.0585 Å, to account for hydrogen disorder in the D phase at lower mantle pressures (Mainprice et al., 2007), as hydrogen symmetrization is observed at pressures greater than achieved in this study (40 GPa) (Tsuchiya et al., 2005).

Phase Egg, named after Eggleton who first synthesized it (Eggleton et al., 1978), is a monoclinic ($P2_1/n$) Al silicate comprised of layers of chain segments of edge-sharing SiO_6 octahedra connected to chain segments of edge-sharing $Al(O,OH)_6$ octahedra. These layers stack upwards along the c-axis, and are connected by corner-sharing and O-H-O bonds that

form between the octahedra of the different layers (Fig. 2.1b). The lattice parameters are a=6.9672 Å, b=7.1835 Å, c=4.3287 Å, and γ= 98.202° (Schulze et al., 2018). Here I use the monoclinic first setting, with c as the unique axis to be consistent with the convention used in the Rietveld texture refinement of the software MAUD (Lutterotti et al., 1997;Lutterotti et al., 2014; Wenk et al., 2014).

δ-AlO(OH) is an aluminum oxide hydroxide that shares its composition with diaspore (α-AlO(OH)) and boehmite (γ-AlO(OH)). δ-AlO(OH) is orthorhombic ($P2_1nm$) with lattice parameters of a=4.7128 Å, b=4.2221 Å, and c=2.8315 Å. The structure of δ-AlO(OH) is considered isotypic with β-CrOOH, with columns of edge-sharing $Al(O,OH)_6$ octahedra along the c-axis, linked to other columns by corner-sharing (Fig. 2.1c). O-H-O bonds form between octahedra of the different columns (Komatsu et al., 2006).

Since the discovery of hydrous high pressure phases, several phases have been added to the "Alphabet series", the name for the magnesium high pressure hydrous silicate transformation series, starting with phase A in the lowest pressure around 10 GPa, going to phase D around 20 GPa, superhydrous phase B at 23 GPa, and phase H at 40 GPa (Fig. 2.2) (Nishi et al., 2014). The higher pressure phase δ-AlO(OH) has gained interest due to its stability at lower mantle pressures and thus potential to transport water to the core. The stability and elastic constants of these hydrous phases have been studied with first principles (Mainprice et al., 2007; Tsuchiya and Tsuchiya, 2009; Thompson et al., 2022), however the deformation behavior and contribution to anisotropy in the mantle has only been studied for phase D (Rosa et al., 2013). In this chapter, I report the results from the texture and deformation study on hydrous phases D, Egg, and δ-AlO(OH) synthesized in a diamond anvil cell in radial geometry combined with laser heating to approach mantle conditions.
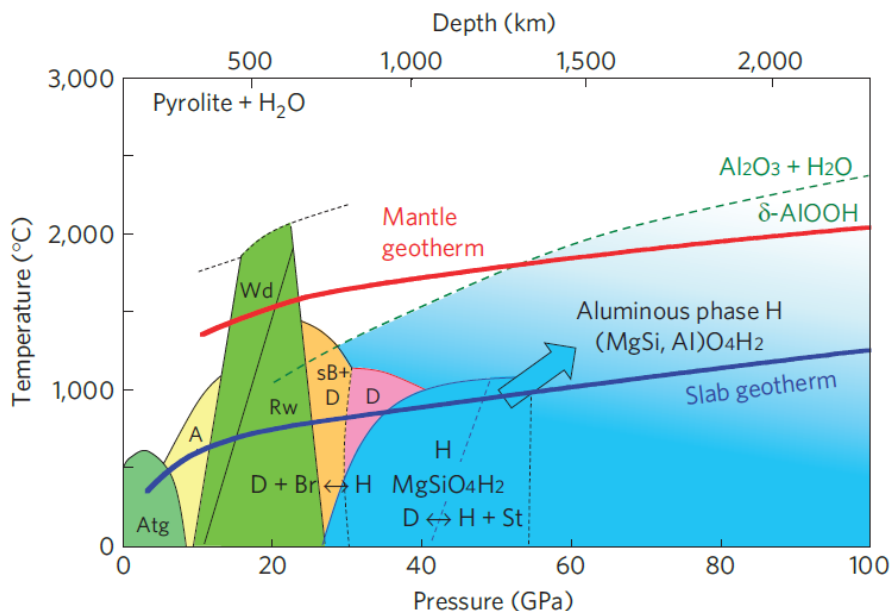
Figure 2.2: *Pressure–temperature diagram showing stability zones of hydrous phases with 2 wt% H_2O from Nishi et al., 2014. Typical geothermal temperature gradients are shown in solid lines for the mantle (red) and cold slab subduction (blue). Colored regions demarcate regions where water is retained in the crystal structure. Atg is antigorite, A is phase A, Wd is wadsleyite, Rw is ringwoodite, sB is superhydrous phase B, D is phase D, and H is phase H.*

2.2 Methods: Experiment set up

High pressure texture studies use the well-established radial diffraction technique (e.g. Merkel et al., 2000; Merkel et al., 2006; Wenk et al., 2006a; Miyagi et al., 2010; Miyagi and Wenk, 2016), in which the DAC is loaded into the x-ray beam such that the compression axis is perpendicular to the beam path, sending the x-ray beam through the gasket and sample material, and the diffraction patterns are captured by the detector located downstream. CPO is observed as azimuthal intensity variation of Debye rings on the diffraction image collected by the detector (Fig. 2.3). This experiment was conducted at the Advanced Light Source (ALS) non-ambient diffraction beamline 12.2.2 using an x-ray energy of 25 keV and spot size of 10 μm, a Dectris Pilatus 1M detector and a gas-actuated pressure membrane to increase pressure remotely (Fig. 2.4). The experiment is controlled from the beamline station computers outside of the hutch.

The beamline controls are accessed via the LabView Acquisition window (Fig. 2.5). The monochromatic x-ray beam enters the hutch through the fast shutter, which can be controlled remotely via the acquisition window, travels through a a set of slits to set the
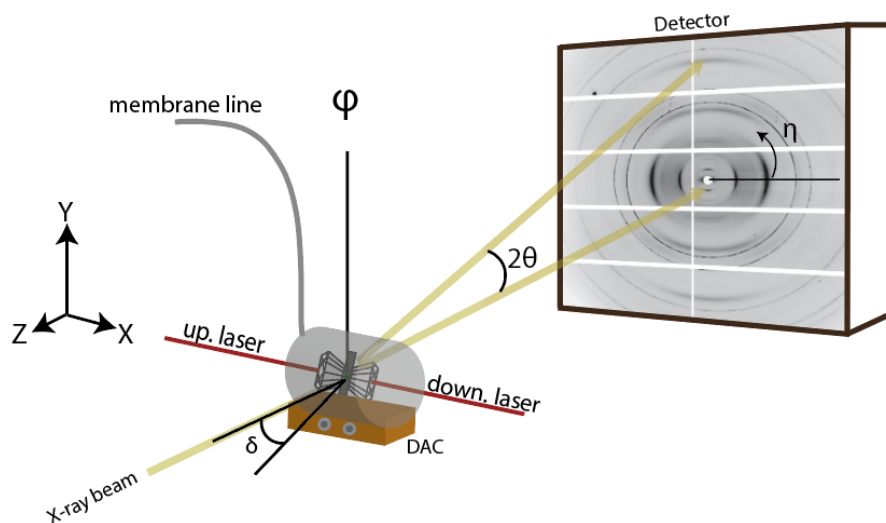
Figure 2.3: *Schematic of beamline geometry at 12.2.2. DAC mounted on a copper cooling block is oriented with compression axis perpendicular to the direction of the x-ray beam, and infrared heating lasers are oriented parallel with the axis of compression. DAC is centered on the rotation axis (ϕ) and wobbled (δ) to increase grain statistics.*

spot size diameter, and then an ionization chamber (I1) to measure the intensity of the x-ray beam. The beam is then focused using Kirk-Baez mirrors, the scatter is reduced by a pin hole, and the x-ray beam reaches the DAC. The remote-controlled diode is placed into the beamline between the DAC and the detector to measure the transmitted x-ray signal and is removed from the beam path during diffraction. The beamstop, located just upstream from the detector, prevents the direct beam from hitting the detector which captures diffraction patterns.

   In this experiment, the spot size of the beam was set to 10 µm and beam energy was set to 25 keV. The detector was set at a distance 225 mm from the sample and translated -9 mm in the X direction such that the vertical interpanel gap between detector submodules was not in the center of the diffraction pattern so as not to miss any texture intensity that will collect along the vertical detector axis. A standard of CeO_2 was used to calibrate the beamline geometry and center the sample stage on the rotation axis. A calibration file for Dioptas software (Prescher & Prakapenka, 2015) was created using CeO_2. Dioptas is used for quick phase identification while running the experiment.

   Two diamond anvil cells (DACs) were prepared in the same way for the two samples; a pair of brilliant cut 300 µm culet diamonds set on cubic boron nitride backing plates were aligned in the a BX-90-RD DAC (Kantor et al., 2012) (Fig. 2.6). A boron epoxy gasket (Merkel & Yagi, 2005) 65 µm in thickness was cut using the laser mill to have an outer diameter of 350 µm and an inner diameter (sample chamber diameter) of 60 µm. The gasket was placed
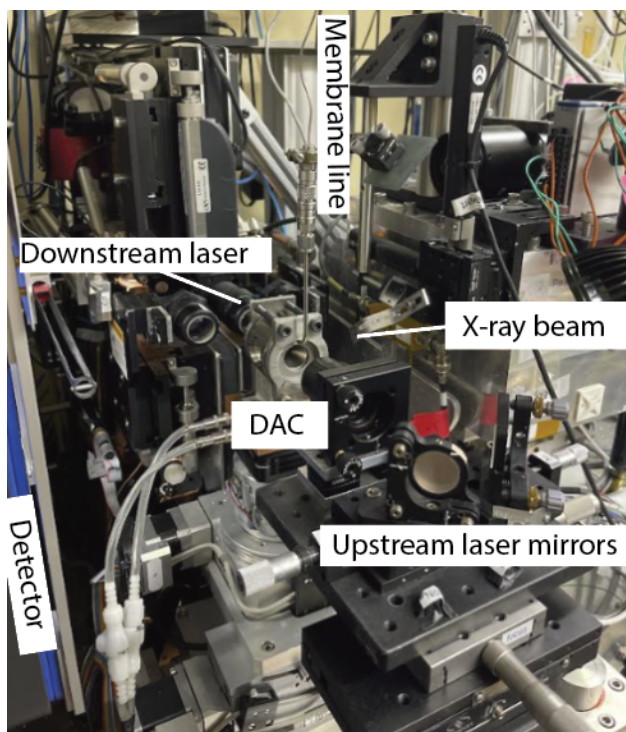
Figure 2.4: *Experimental setup inside the hutch at ALS 12.2.2 for radial DAC diffraction. DAC is loaded such that the axis of compression is perpendicular to the x-ray beam. Detector behind the DAC captures diffraction signal. Upstream and downstream lasers are directed to the sample chamber through the diamonds. Gas-actuated pressure membrane is used to increase pressure in the DAC remotely.*
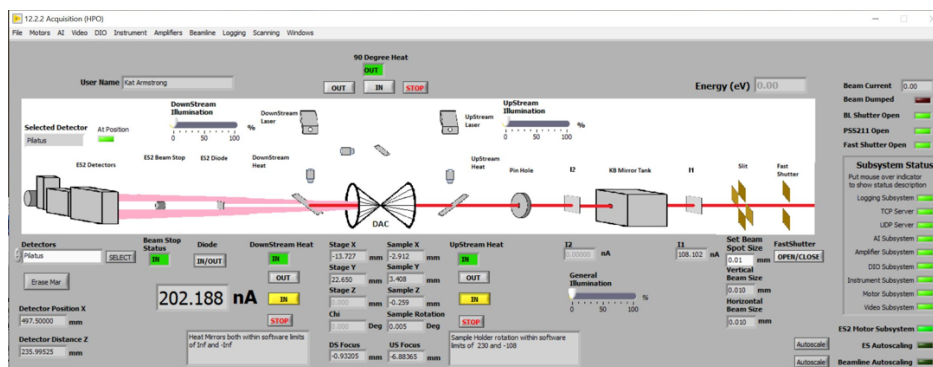

Figure 2.5: *LabView Acquisition window used for beamline control at ALS 12.2.2.*

into a rectangle of kapton tape 100 µm in thickness. The two DACs were prepared with different starting samples. Phase D was synthesized from natural serpentine sourced from Herbeira, Northern Spain [$(Mg_{0.76}, Fe_{0.24})_3Si_2O_5(OH)_4$], and phase Egg and δ-AlO(OH) were synthesized from kaolin (Sigma Aldrich Lot #120M0110V) [$Al_2Si_2O_5(OH)_4$]. Five percent by weight of platinum powder was added to the serpentine powder, and three percent by weight of platinum powder was added to the kaolin sample as a pressure standard and to help with laser coupling. Both the serpentine+Pt and kaolin+Pt mixtures were combined with deionized water and ground into a fine powder using a mortar and pestle to form a paste and to evenly distribute the Pt powder. The sample pastes were pre-compressed between two glass slides to reduce their porosity and flakes of the pre-compressed sample were loaded into the sample chamber. Once the sample chamber was full, the top anvil was used to compress the paste into the sample chamber and more powder was placed into the sample chamber and then compressed again with the top anvil a couple more times. A pressure medium was not used in this experiment to allow texture to develop. The DACs were closed with the top anvils and the screws were tightened to "finger tight".

After loading the DAC into the beamline and roughly aligning the DAC to the x-ray beam path using the beamline cameras, the LabView DAC centering routine is used to center the sample chamber onto the x-ray beam path; x-ray transmission is measured using the diode during translational scans over specified ranges (delta) in the X and Y directions. Based on the differences in x-ray absorptivity of the sample to the gasket material, a peak or a valley of photon counts is expected at the sample chamber compared to the surrounding gasket. In this experiment, due to the strong x-ray absorptivity of platinum, a decrease in photon counts is observed at the sample chamber (Fig. 2.7). The x-ray beam is centered to the middle of the "valley" in both X and Y directions. Consecutive scans with smaller delta and increment (step size) are used for higher resolution. It can sometimes be difficult to differentiate the sample from the x-ray transparent gasket, and therefore Pt is helpful in identifying the location of the sample chamber. Performing a 2D Transmission scan can also help locate the sample chamber. The sample is then aligned onto the rotation axis using the Z on Phi routine.
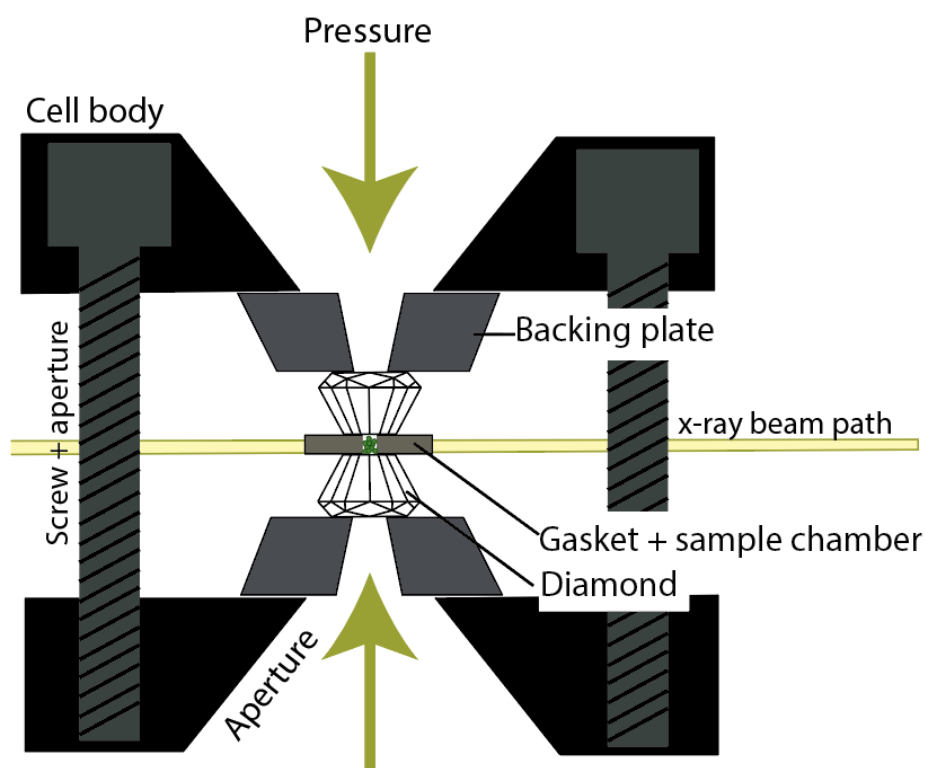
Figure 2.6: *Schematic of a diamond anvil cell. Diamonds glued to backing plates are loaded and aligned on top of each other and in the center of the diamond anvil cell body. Sample loaded into the sample chamber hole, milled out of the gasket material, is placed in the center of the diamond culets. Pressure is generated by squeezing the diamonds together, either using the screws in the DAC body, or the gas membrane at the beamline. X-ray beam path for radial diffraction geometry is shown here, perpendicular to the axis of compression.*
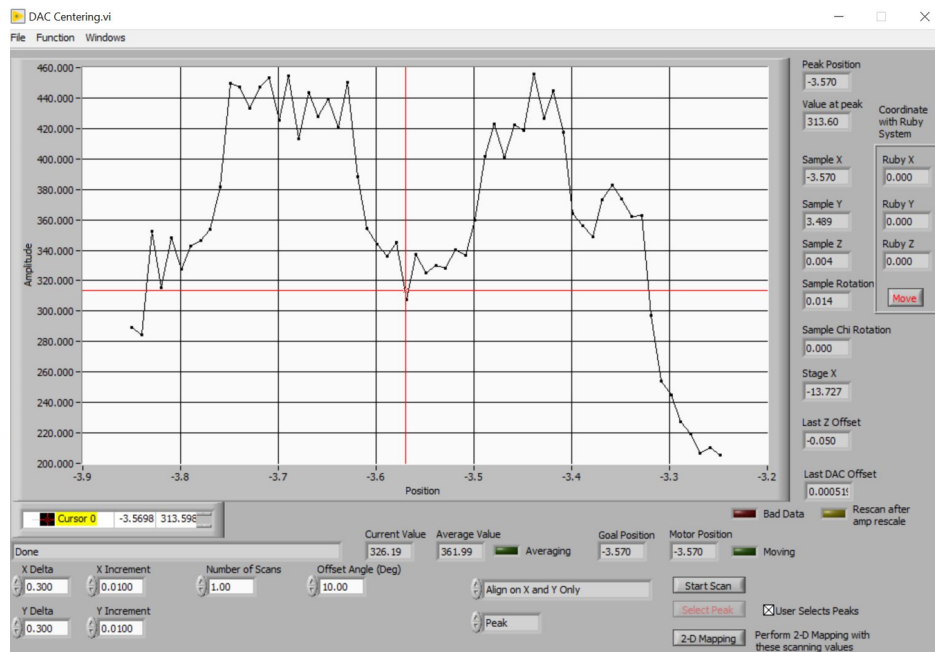
Figure 2.7: *DAC Centering LabView window used to align the sample chamber to the x–ray beam at ALS 12.2.2. The cell is first aligned on X and Y, and then Z on Phi. Absorption valleys, as seen here, can indicate the sample chamber location relative to the gasket.*

2.3   Methods: Serpentine to phase D

The DAC was brought to 22 GPa (Pt signal) with three steps of increasing pressure using the Druck pressure membrane. Increasing pressure can cause the sample chamber location to shift, and therefore the DAC was recentered prior to taking a diffraction pattern. A 30 sec diffraction pattern was captured and the pressure from the Pt signal was determined using Dioptas and the equation of state of Pt (Fig. 2.8).

Once the pressure was verified by analyzing the Pt signal in Dioptas, a longer exposure (60 sec) diffraction pattern was captured to get a stronger signal of the sample prior to transformation. The double-sided laser heating system (Kunz et al., 2018) was then used to heat the sample chamber for 30 mins at 1200 K to induce the phase transformation.

The two infrared lasers, located upstream and downstream from the DAC, are aligned on top of each other to reduce temperature gradients in the DAC sample chamber during heating and for precise control over the laser heating area. Alignment of lasers is done prior to the experiment using the AgI standard which couples well with the infrared lasers. A schematic of the double-sided laser heating system is shown in Figure 2.9. The upstream laser must be redirected into the DAC using mirrors (B, C) and a lens (D). The downstream laser enters the DAC through the opposite anvil.

Coupling of the sample to the infrared lasers depends on the thermal conductivity and emissivity of the sample (Kunz et al., 2018). The power settings of the lasers are controlled using the Laser Screen window (Fig. 2.10). After enabling the upstream and downstream lasers, the Power Setting was increased stepwise until the sample visibly coupled with the laser; a warm glow should be seen in the laser chamber in Laser Viewing Screen window (Fig. 2.11). The positioning of the lasers relative to the sample is visualized using the upstream (Fig. 2.11A) and downstream camera views (Fig. 2.11B) on the Laser Viewing Screen. Temperature of the heated sample is measured using a spectrometer that is centered in the field of view of the camera and therefore it is best to align the lasers in the center of the field of view of the camera.

The heating cycle resulted in partial transformation to phase D. Using the equation of state from Thompson et al., 2022 and Dioptas, the pressure of phase D was determined to be 17 GPa. Pressure was increased to 29 GPa (phase D signal) and the sample chamber was heated again for 10 mins at 1300 K. This resulted in more complete transformation of serpentine to phase D. Minor stress is visible in phase D and texture is present, albeit weak (Fig. 2.12). The DAC was then decompressed stepwise using the Druck pressure system but a phase change was not observed during decompression, likely due to the top and bottom anvil sticking together without sufficient time to relax and effectively keeping the sample chamber at pressure during the remainder of the experimental time at the beamline.
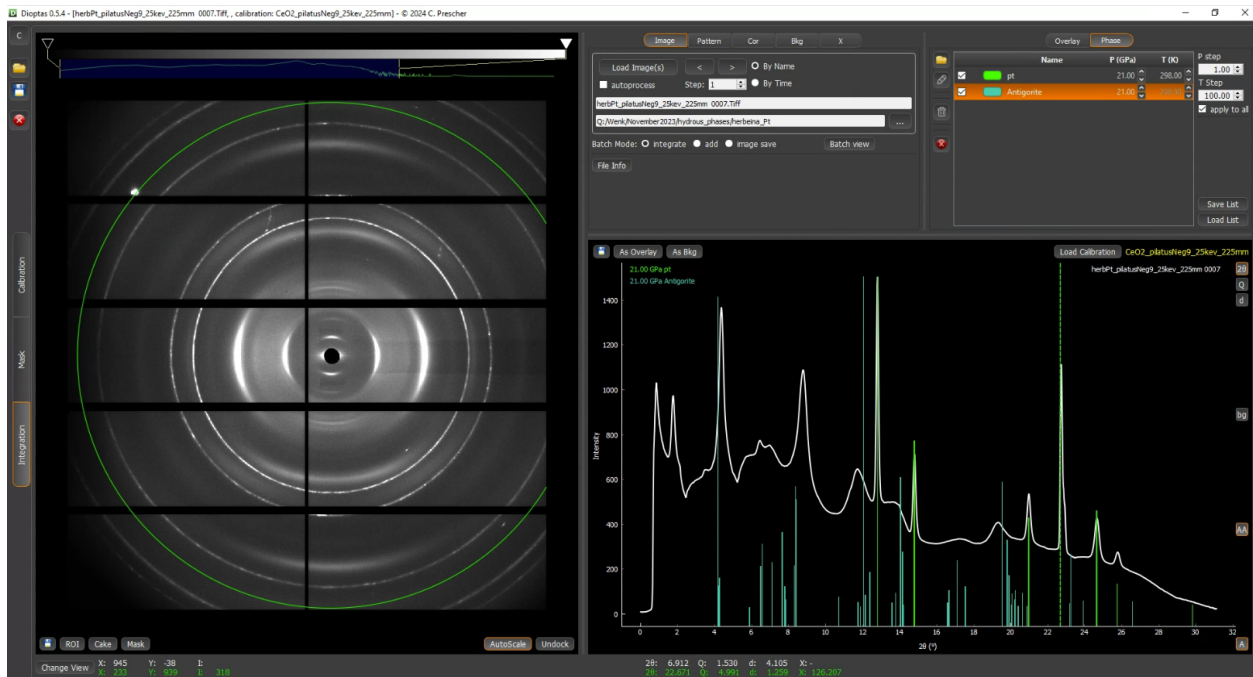
Figure 2.8: *The software Dioptas is used to quickly identify phases and monitor pressure while on the beamline. Left is the diffraction pattern, and right is the integration of the diffraction pattern. Platinum peaks (green lines) and antigorite peaks (blue lines) are loaded as potential phases. Dioptas uses the equation of state of both phases to determine their pressure. Here, the Pt signal is at approximately 21 GPa.*
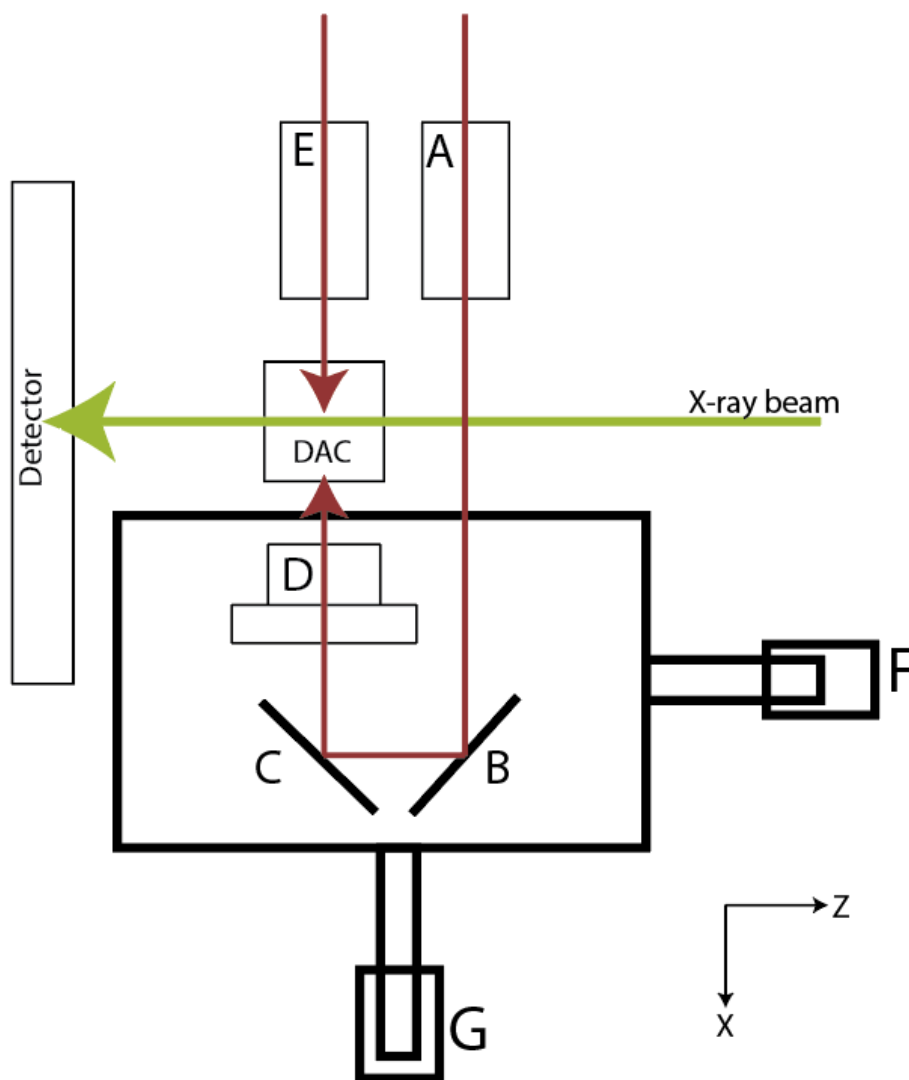
Figure 2.9: *Birds-eye-view of double-sided infrared laser heating system at ALS 12.2.2. DAC loaded radially into the beamline such that the axis of compression is perpendicular to the direction of the x-ray beam. Upstream infrared laser (A) is redirected via reflection off of mirrors B and C, travels through focusing lens D into the DAC through the axis of a diamond anvil. Downstream laser (E) is directed through the opposite anvil. The upstream focus and positioning can be modified using micrometers F and G, and the downstream focus using beamline motors. Sample/laboratory coordinates XYZ.*
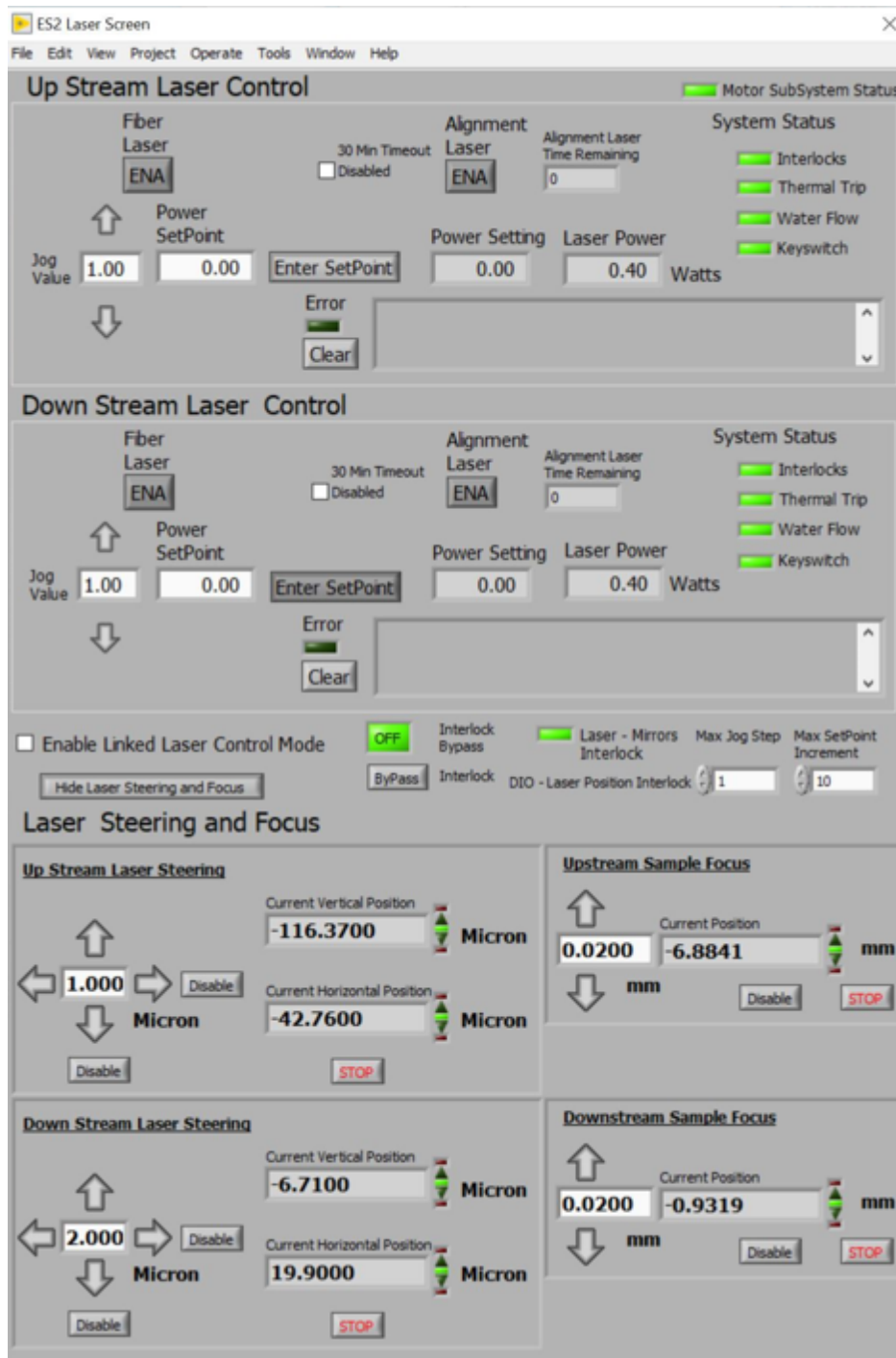
Figure 2.10: *LabView Laser Control window at ALS 12.2.2. Up Stream and Down Stream Laser control adjust the power of the lasers. Laser Steering and Focus is used to reposition the lasers.*
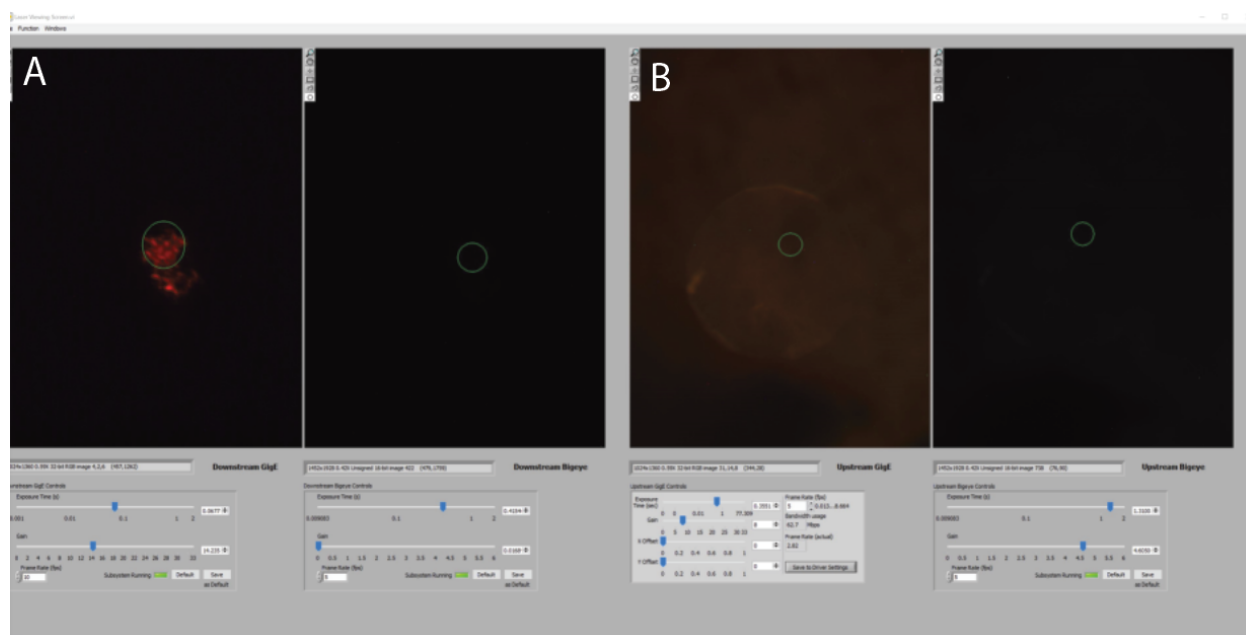
Figure 2.11: *LabView Laser Viewing screen is used to see the positioning of the lasers relative to the sample. Here a backlit sample chamber can be seen in the downstream GigE camera (A). The red color is from light from the upstream illumination transmitted through the sample chamber. The downstream GigE camera shows the diamond culet. Glare is present in the radial different geometry.*
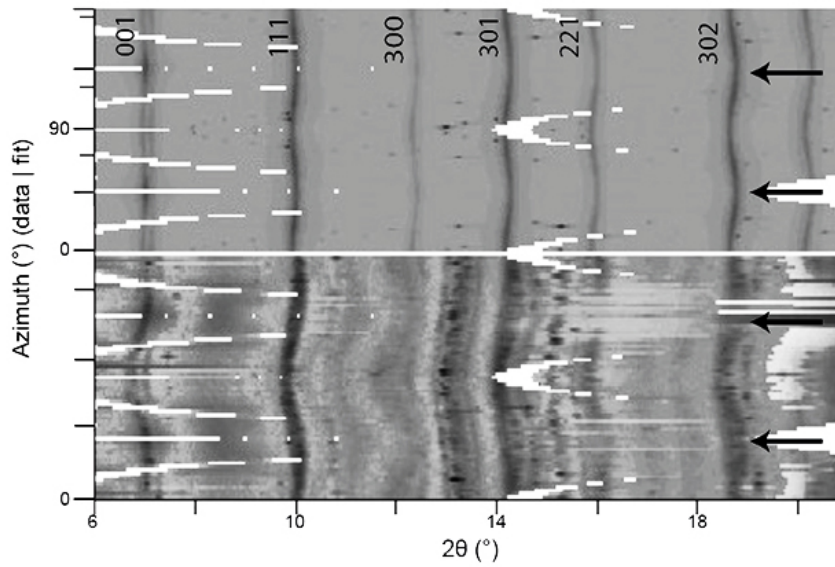
Figure 2.12: *Data processing using the software MAUD. Unrolled diffraction pattern for phase D (bottom) at 29 GPa and Rietveld fit (top). Horizontal axis is 2-theta (in degrees), and vertical axis is azimuth of the diffraction pattern (in degrees). The axis of compression in each diffraction pattern is indicated by black arrows. Some phase D diffraction peaks are labeled.*

2.4 Methods: Kaolinite to phase Egg and δ-AlO(OH)

The DAC was brought to 25 GPa (Pt signal) using the Druck pressure system. The stability zone of Egg was slightly overshot, so the DAC was decompressed by 2 steps to reduce the pressure inside the sample chamber and bring it back into the Egg stability zone. The DAC was then heated for 20 mins at 1300-1500 K and transformation to phase Egg was observed. The equation of state for phase Egg (Wang et al., 2022) indicated phase Egg was at 16 GPa as determined in Dioptas. The sample was then heated again for 10 mins at 1500 K for more complete transformation. Pressure was then increased to 30 GPa (phase Egg signal) and high stress was observed in the diffraction pattern based on the curvature of the diffraction lines relative to azimuth with larger 2 thetas along the axis of compression due to compression of the unit cell (Fig. 2.13). The sample was then heated for 30 mins at 1100-1500 K and the high pressure δ-AlO(OH) phase (Fig. 2.1c) was observed along with stishovite which was then used as a pressure calibrant. Pressure was increased (37 GPa stishovite signal, 32 GPa δ-AlO(OH) signal) to observe deformation texture in δ-AlO(OH) (image#033, Fig. 2.14). The pressure membrane was then decompressed and no phase transformation was observed. Negligible decompression was observed in the decompression diffraction patterns, likely the anvils were again stuck together and unable to release pressure in the experimental time frame.
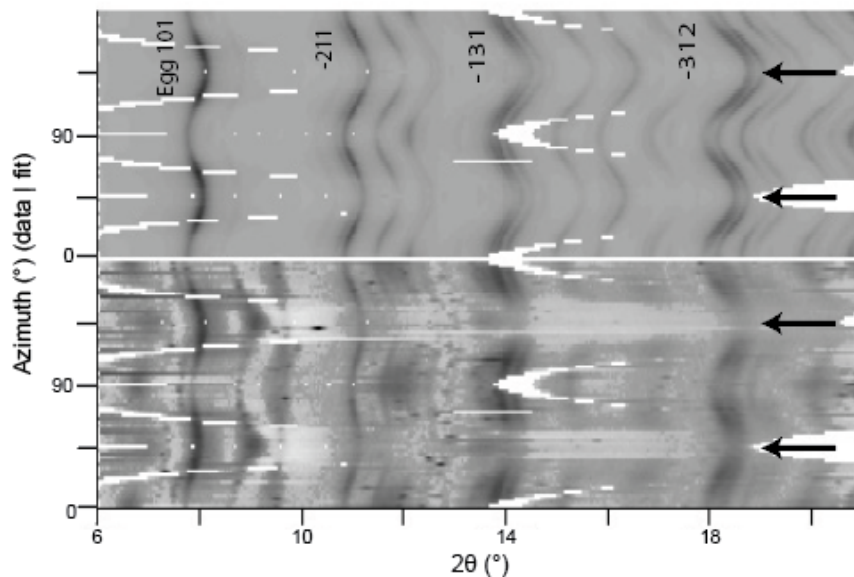

Figure 2.13: *Unrolled diffraction pattern of Phase Egg at 30 GPa (phase Egg signal) (bottom) and Rietveld fit (top). Horizontal axis is 2-theta (in degrees), and vertical axis is azimuth of diffraction pattern (in degrees). Axis of compression is indicated by black arrows. Some diffraction peaks of phase Egg are labeled.*
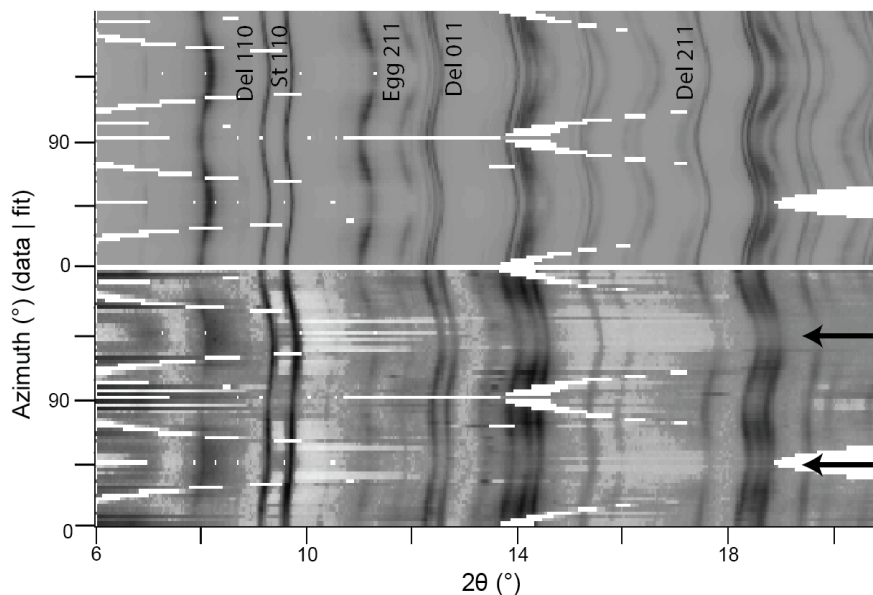
Figure 2.14: *Unrolled diffraction pattern of δ-AlO(OH) phase at 32 GPa (δ-AlO(OH) signal) (bottom) and Rietveld fit (top). Phase Egg (Egg) and stishovite (St) are also present. Horizontal axis is 2-theta (in degrees), and vertical axis is azimuth of diffraction pattern (in degrees). Compression axis is indicated by black arrows. Some diffraction peaks are labeled.*

2.5   Results: Texture and stress refinement

Diffraction images were analyzed with Rietveld refinement using MAUD software (Lutterotti et al., 1997; Lutterotti et al., 2014; Wenk et al., 2014). A CeO$_2$ diffraction image collected during beamline calibration was used for instrument calibration in MAUD. To load a diffraction pattern into MAUD to be analyzed, it must be converted to .esg files. The embedded version of ImageJ software pre-loaded into MAUD is used to adjust the contrast of the image and set the parameters such as the detector pixel size, center of the detector, and sample-detector distance. Any intensity in the interstitial space between detector panels is removed by selecting the areas and using the Process>Math>Subtract function. In this experiment, some diamond reflections produced bright spots on the diffraction pattern which were also subtracted. Using Plugins>Maud Plugins >Multi-Spectra from normal transmission/reflection image, the area of the image is selected and the integration parameters are set: the center of the diffraction pattern, the azimuthal range to be integrated, the azimuthal segment value (phi), the number of segments/spectra generated (Fig. 2.15). The number of spectra should be equal to the range between the starting and final angle divided by the Phi angle.

In this experiment, each image was divided into seventy-two 5° azimuthal segments. Each segment is then individually integrated and the intensity values are plotted as a function of
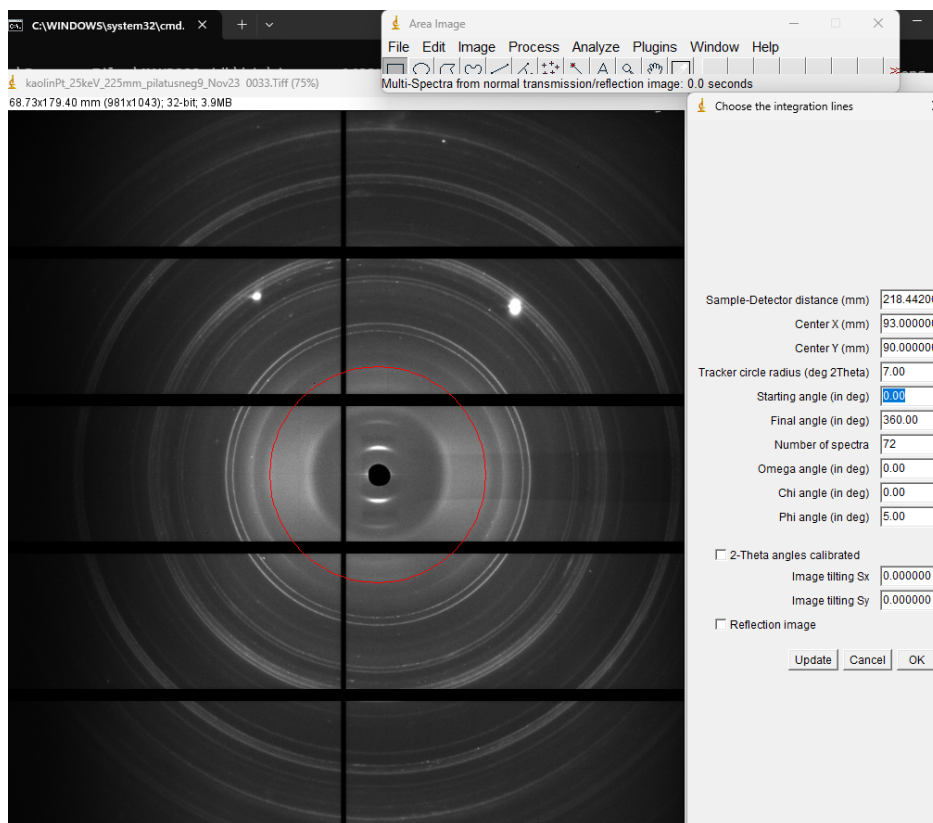
Figure 2.15: *MAUD integration settings are set using the ImageJ software plugins embedded in MAUD. Phi angle is the azimuthal segmentation value. The number of spectra should be equal to the range between the starting and final angle divided by the Phi angle. Diamond reflections (the bright spots) were excluded from analysis by subtracting their intensities while making the ESG files.*

2θ against azimuth, essentially stacking each consecutive azimuthal segment on top of the previous to create an "unrolled" diffraction pattern as seen in Figs. 2.12, 2.13, 2.14. The refinement range was set to 6-21° 2θ. Diffraction from the gasket as well as an overpowering Pt signal in the serpentine sample were excluded from the analysis by excluding these 2θ regions. A close match was obtained between the measured (Figs. 2.12, 2.13, 2.14 bottom) and calculated spectra (Figs. 2.12, 2.13, 2.14 top); the background functions (polynomial and interpolation), scale, and lattice parameters were refined. Axial stress was modeled using the Moment Pole Stress model (Matthies, 1996) and refined based on the curved shape of diffraction lines as function of azimuth η in Figs. 2.12, 2.13, 2.14 and the elasticity tensor for each phase. Single crystal elastic constants for phase D at 25 GPa (Mainprice et al., 2007), phase Egg at 24 GPa (Mookherjee et al., 2019), and δ-AlO(OH) at 30 GPa (Tsuchiya & Tsuchiya, 2009) were used. Fiber symmetry was imposed to reflect the geometry of the DAC

and the three-dimensional orientation distribution function (ODF) was calculated with the E-WIMV algorithm (Matthies & Vinel, 1982).

Compressive stress was calculated to be -2.24 GPa for phase D, -8.61 GPa for phase Egg, and -3.74 GPa for δ-AlO(OH). Crystallographic preferred orientation ODFs were exported from MAUD and imported into BEARTEX software (Wenk et al., 1998) to generate CPO pole figures. Phase D and Egg show a (001) maximum along the compression axis indicating that the (001) planes aligned themselves perpendicular to the axis of compression, and δ-AlO(OH) shows a (010) maximum along the compression axis, indicating the (010) planes align perpendicular to the axis of compression (Fig. 2.16). Phase Egg produced a (001) maximum of 10.33 multiples of random distribution (m.r.d.), D produced a (001) maximum of 7.37 m.r.d, and δ-AlO(OH) produced a (010) maximum of 2.97 m.r.d. The weaker texture in D and δ-AlO(OH) compared to Egg is evident in the diffraction patterns, as Egg shows a greater intensity variation along the azimuth. In each phase, the "sheet-like planes" in the crystal structure (the basal planes (001) for phase D and Egg, and the (010) planes for δ-AlO(OH)) aligned themselves perpendicular to the compression axis.

Potential deformation mechanisms for the trigonal phase D were modeled using the viscoplastic self-consistent approach (VPSC) (Lebensohn & Tomé, 1993). Compressive strain was applied to 4000 randomly oriented grains. Eight different slip systems were activated with low critical shear stress for (0001) <10-20> 50% strain produced an excellent fit with the CPO pole figure generated from the observed aggregate (Fig. 2.17). So far deformation mechanisms for phase Egg and δ-AlO(OH) were not modeled but it is likely that here also basal slip (001) is the dominant slip system for phase Egg and (010) slip for δ-AlO(OH).
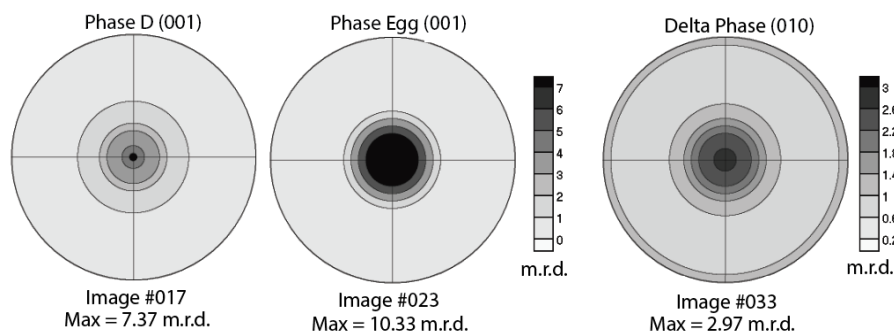

Figure 2.16: *Deformation textures of hydrous phases D, Egg, and δ-AlO(OH). Phase D (001) texture max=7.37 m.r.d. (herbPt_017). Phase Egg (001) texture max=10.33 m.r.d. (kaolinPt_023). δ-AlO(OH) (010) max=2.97 m.r.d. (kaolinPt_033). Compression axis is in the center of each plot. Plots are equal area projections.*
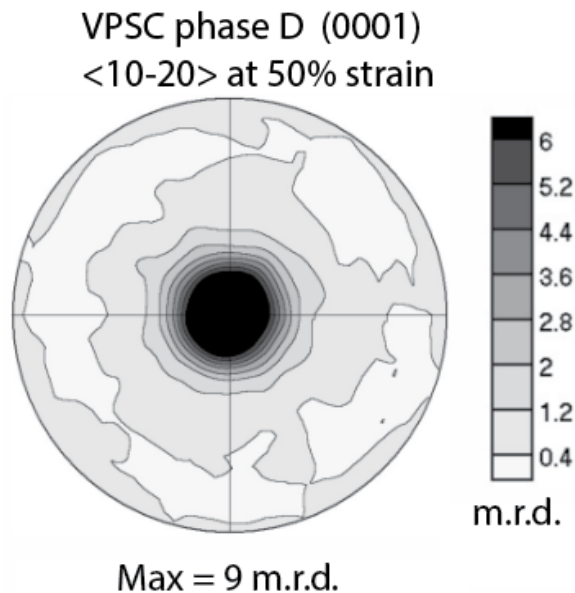
Figure 2.17: *VPSC modeling for phase D at 50% strain with dominant basal slip. Max = 9 m.r.d. Compression axis is in the center of the plot. Equal area projection.*

2.6 Results: Elastic properties, anisotropy, & implications for the mantle

There is strong evidence showing seismic anisotropy in the transition zone near the vicinity of subducting slabs, suggesting deformation and CPO development of mid-mantle phases (e.g. Long, 2013). To compare the elasticity of the hydrous phases against other lower mantle phases, the P-wave anisotropy was calculated for each phase using the following equation:

$$An\% = 200(Pmax - Pmin)/(Pmax + Pmin) \qquad (2.1)$$

where P_{max} is the maximum P-wave velocity for the phase and P_{min} is the minimum P-wave velocity. The maximum shear wave splitting (dS) is also shown in Table 2.1. BEARTEX (Wenk et al., 1998) was used to calculate the aggregate elastic tensor based on ODF and single crystal elastic properties. The calculated aggregate elastic tensor coefficients are listed in Table 2.2. For each phase a .TEN file with the single crystal elasticity constants was created. The .TEN file was loaded into VELO which calculates a distribution of P-wave, S-wave, and dS velocities for each phase in all spherical directions and is compiled in an output .XVX file. The maximum and minimum velocities from this file were used to plot shear wave splitting pole figures for single crystals (Fig. 2.18a) and deformed aggregates (Fig. 2.18b) using PING. P-wave anisotropy and dS max for both phase D and Egg single

Table 2.1: *P-wave anisotropy and shear wave splitting (dS) of mantle phases*

Phase	P-An(%)	dS max (km/s)	Reference
D (single crystal)	8.7	1.15	Mainprice et al. (2007)
D (aggregate, image #017)	0.86	0.10	
Egg (single crystal)	11.3	0.77	Mookherjee et al. (2019)
Egg (aggregate, image #023)	5.8	0.18	
Delta (single crystal)	13	2.1	Tsuchiya and Tsuchiya (2009)
Delta (aggregate, image #023)	0.78	0.08	
Wadsleyite	10.5	1.48	Nunez-Valdez et al. (2011)
Ringwoodite	0.74	0.11	Lin et al. (2018)
Bridgmanite	8.8	0.61	Lin et al. (2018)
Ca-Perovskite	11.6	1.66	Karki and Crain (1998)
Periclase	10.8	0.12	Sinogeikin and Bass (1999)
Post-perovskite (0 K)	21.2	2.39	Tsuchiya et al. (2004)

crystal is greater than that of ringwoodite, bridgmanite and periclase (Table 2.1).

Polycrystalline anisotropies of the deformed aggregates were calculated by generating an elasticity tensor of the deformed aggregate in BEARTEX using the 3D orientation distribution function generated by MAUD for each phase and the single crystal elasticity constants. CMAU was used to convert the Maud-generated ODF (.MOD file) into a binary BEARTEX ODF (output .YOM file), which was then smoothed using SMOO (output .YSO file). TENS was then used to calculate the tensor properties of the polycrystalline aggregate using the smoothed ODF and the single crystal elasticity constants in the .TEN file (output .TEN file). The geometric mean polycrystalline stiffness tensor (Matthies & Humbert, 1995) was used to calculate the seismic wave velocities using VELO (output .XVX file) and shear wave polarity direction (output .XVV file) of the aggregate for each phase, and PING was used to plot them as pole figures relative to sample coordinates (Fig. 2.18b). The deformed aggregate

Table 2.2: *Geometric mean polycrystalline stiffness tensor coefficients*

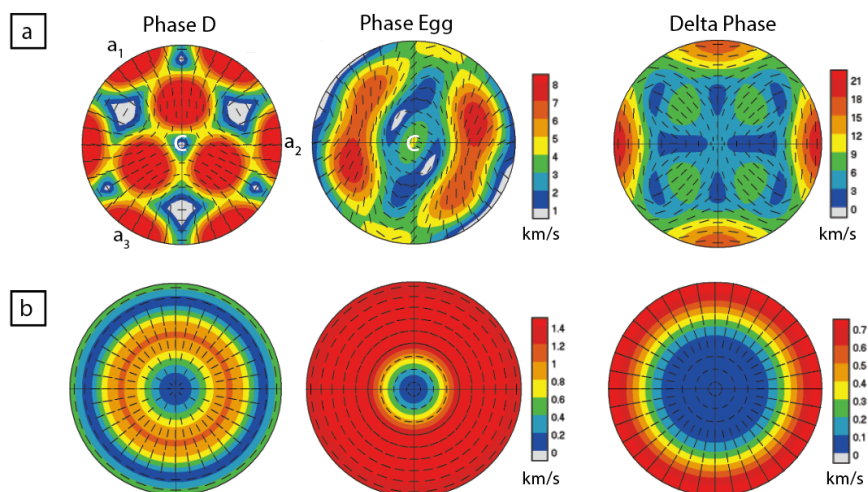|	Phase D	Phase Egg	δ-AlO(OH)
C_{11}	537	617	565
C_{22}	537	617	565
C_{33}	535	550	573
C_{44}	174	199	193
C_{55}	174	199	193
C_{66}	176	206	189
C_{12}	184	205	187
C_{13}	178	196	186
C_{23}	178	196	186

Figure 2.18: *(a) Shear wave splitting seismic velocity projections of single crystal phase D, phase Egg, and δ-AlO(OH). (b) Shear wave splitting for deformed aggregates of phase D, phase Egg, and δ-AlO(OH). The compression direction is in the center of each plot. Color indicates velocity difference of fast and slow shear waves. Black lines indicate directions of the fast S waves. Plots are equal area projections*

of phase D had relatively strong texture (7.4 m.r.d.) but shows a weak shear wave splitting (0.10 km/s), while the deformed aggregate of phase Egg had a stronger texture (10.3 m.r.d.) and shows slightly higher shear wave splitting (0.18 km/s). δ-AlO(OH) has significant single crystal anisotropy, however only a weak texture was developed during the experiment (2.97 m.r.d.) and thus the shear wave splitting of the aggregate is also weak (0.08 km/s). P-wave anisotropy is very weak for phase D aggregate (0.86%) and δ-AlO(OH) aggregate (0.78%),

while phase Egg aggregate shows significant p-wave anisotropy (5.8%).

Mantle convection models (Wenk et al., 2011; Chandler et al., 2021b) have relied on the deformational properties of the anhydrous phases ringwoodite, bridgmanite, periclase, and post-perovskite to explain the crystallographic preferred orientation and resulting anisotropy that could result from mantle flow (Merkel et al., 2006; Miyagi et al., 2010; Miyagi and Wenk, 2016; Chandler et al., 2021b). However, compared to the anhydrous lower mantle phases, the three hydrous phases investigated in these experiments have very high single crystal P-wave anisotropy compared to other mantle phases: δ-AlO(OH) has the second highest P-wave anisotropy (13%) after post-perovskite (21.2%), and phase Egg has comparable P-wave anisotropy (11.3%) to Ca-Perovskite at 11.6%. Additionally, they have very high single crystal shear wave splitting: δ-AlO(OH) is the second highest (2.1 km/s) post-perovskite (2.39 km/s), and phase D (1.15 km/s) and Egg (0.77 km/s) are greater than bridgmanite (0.61 km/s), which is considered the primary component of the lower mantle, and ringwoodite (0.11 km/s). Anisotropy of the aggregates is always less than the single crystal. Further studies should be conducted to maximize the data collection conditions to optimize the signal so maximum texture development can be measured, especially for δ-AlO(OH) which was not a phase I had planned to target during this investigation.

It is estimated that the volumetric percentage phase D present in the mantle transition zone ranges from 15% for a peridotite containing 2 wt% H_2O (Ohtani et al., 2004), 56.3% for lherzolite containing 8% H_2O, and up to 63.5% for harzburgite containing 9% H_2O (Iwamori, 2004). Phases δ-AlO(OH), D and Egg have shown similar single crystal anisotropy compared to the anhydrous phases of the mantle, as well as the tendency to develop CPO under differential stress. Therefore, hydrous phases could contribute significantly to the anisotropy of the transition zone and mantle. Additionally, due to their -OH content, they could also influence the rheology of the mantle. The deformation mechanisms, particularly δ-AlO(OH), should be investigated further using experiment and VPSC modeling, and should be considered when modeling mantle rheology and anisotropy.

Chapter 3

Paleostress orientation inferred from residual strain in quartzites

3.1   Introduction

Residual strain has been studied by metallurgists and material scientists for decades due to its prevalence in metal manufacturing and significance on material properties (Noyan & Cohen, 1987). Residual strain is the strain that remains in a crystal lattice even after the external stress has been removed. It is the elastic strain that results from the distortion of the crystal structure around defects such as point defects, dislocations, and grain boundaries. It is considered elastic because it is only present so long as the defect — a form of plastic deformation — causing the interruption in the periodic lattice is present. If the defects are removed, through annealing or dislocation mobility, the lattice will return to the unstrained, characteristic lattice parameters of the material and the residual stress is absolved as well. Residual strain can occur due to internal stress, such as from differences in thermal expansion of an object with heterogeneous composition like an alloy, or grain orientation (Hosford, 2005). It can also result from external macrostress on the system such as the manufacturing process which can cause metal fatigue in welds (Staron et al., 2002), railway rails (Kelleher et al., 2003), and bridges (Van Puymbroeck et al., 2019). For natural rock samples, examples of external macrostresses could be tectonic deformation, stresses imposed by earthquakes, meteorite impact or laboratory experimental deformation.

Residual strain can vary intergranularly due to crystallographic anisotropy. In non-cubic crystals, material properties such as thermal expansion coefficient and the elastic modulus are anisotropic and dependent upon crystallographic direction. Therefore, in a polycrystalline material, the response of each grain to a stress can vary depending on the orientation of the grain relative to the stress. Stress can be accommodated by activating slip systems. Slip systems are a combination of a plane and direction along which the dislocations will glide under stress, and become activated when the critical resolved shear stress for slip has been reached (e.g. Hull & Bacon, 2011). Grains oriented favorably for slip relative to the

macrostress will deform at lower stresses than those unfavorably oriented. Additionally, in a multiphase polycrystalline material, grains with higher elastic moduli will experience greater stress changes than grains with lower elastic moduli (e.g. Hosford, 2005).

As mentioned in Chapter 1, there are several methods used to measure residual strain. Synchrotron Laue microdiffraction has previously been used to infer the paleostress magnitude and orientation in quartzites from various localities (Kunz et al., 2009, Chen et al., 2011, Chen et al., 2015, Chen et al., 2016, Wenk et al., 2020). The average distortion of the crystal lattice is measured and an Eigen decomposition of the strain tensor provides the orientation and magnitude of the principal axes of maximum compression, extension, and the intermediate axes of the strain ellipsoid which are used to infer the orientation of the paleostress. In this chapter I explain the methodology and its application to measure the residual strain and infer the paleostress in quartz from hydrothermal features from Hong Kong.

3.2   The samples

Two quartz samples from a hydrothermal environment featuring silica-rich breccia pipes, dikes, and veins in northeastern Hong Kong were used for this analysis. Details about the local geology and the formation of these structures have been described in Chan and Alvarez (2023) and will briefly be summarized here. The hydrothermal breccias are believed to be associated with ascending hydrothermal fluids through the crust. A sample from a cockade breccia vein (e.g. Frenzel & Woodcock, 2014) in Hung Shek Mun (HSM_1159A) and an explosion structure in a breccia dike on Crooked Island, known locally as Kat-O (Ko1_1553C), were used in this experiment. The cockade breccia veins form anastomosing networks through the host rock, which consists of Cretaceous–age reddish sandstones and conglomerates overlaying Late Jurassic-Early Cretaceous lavas and volcaniclastic rocks (Fig. 3.1a). The explosion structures closely resemble those produced by quarry blasting: a central cavity, surrounded by a crushed zone with radial cracking up until a circular "damage boundary" which demarcates the edge of the explosion structure from the host rock (Fig. 3.1b). These explosion structures are found in the breccia dike on Kat-O as well as a breccia pipe on nearby Double Island (Chan & Alvarez, 2023). Ko1_1553C was collected 10 cm from the center of an 80 cm diameter explosion structure in the breccia dike on Kat-O.

Standard thin sections were made from both rocks. HSM_1159A shows small, oblong grains at various orientations showing little to no undulatory extinction (Fig. 3.2). Ko1_1553C shows grains with irregular grain boundaries suggestive of dislocation creep (Hirth & Tullis, 1992), and deformation lamellae (Fig. 3.3). As opposed to planar deformation features which are associated with shock features, the deformation lamellae present in Ko1 are not aligned with any crystallographic direction, are not truly planar and rather are curvy structures that bifurcate (Vernooij & Langenhorst, 2005).
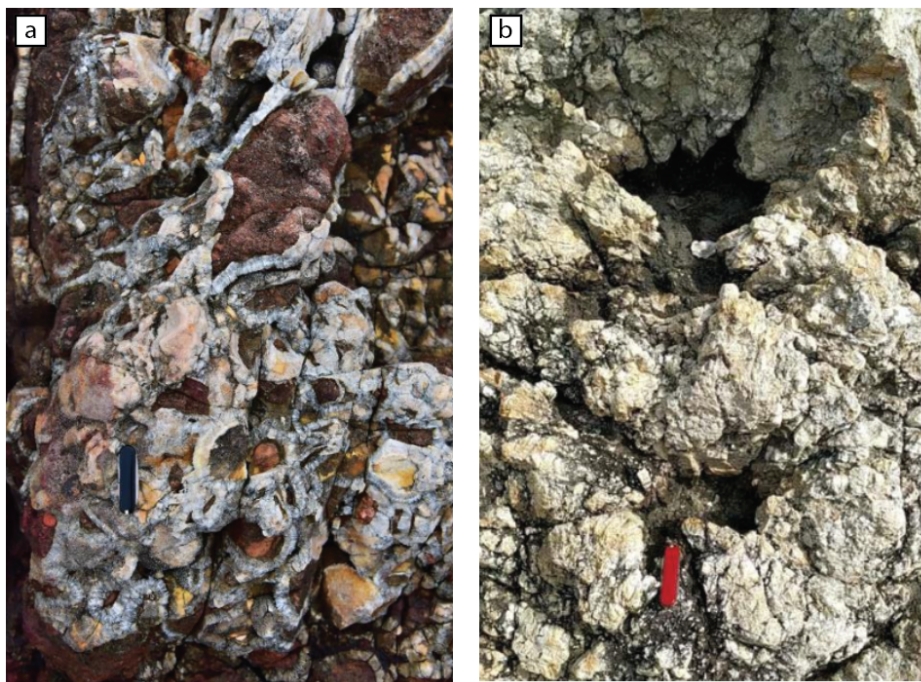
Figure 3.1: *Outcrop photos of (a) cockade breccia vein on Hung Shek Mun, and (b) explosion structure in breccia dike on Kat-O. Black and red pocket knife (8 cm in length) for scale.*
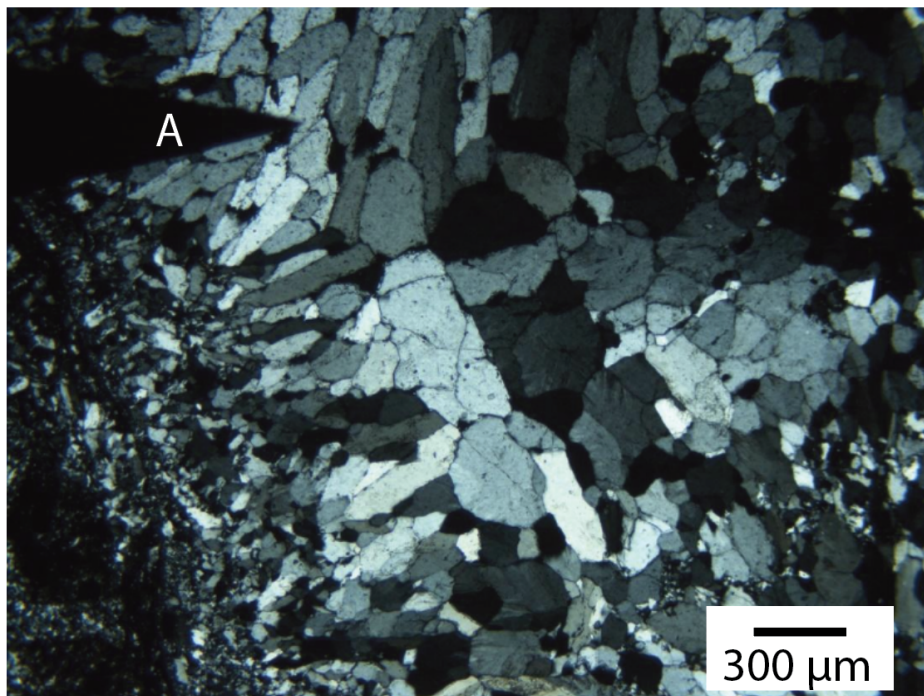
Figure 3.2: *Photo micrograph of HSM_1159A in cross-polarized light at 20x magnification. HSM data presented below was collected to the right of arrow (A).*
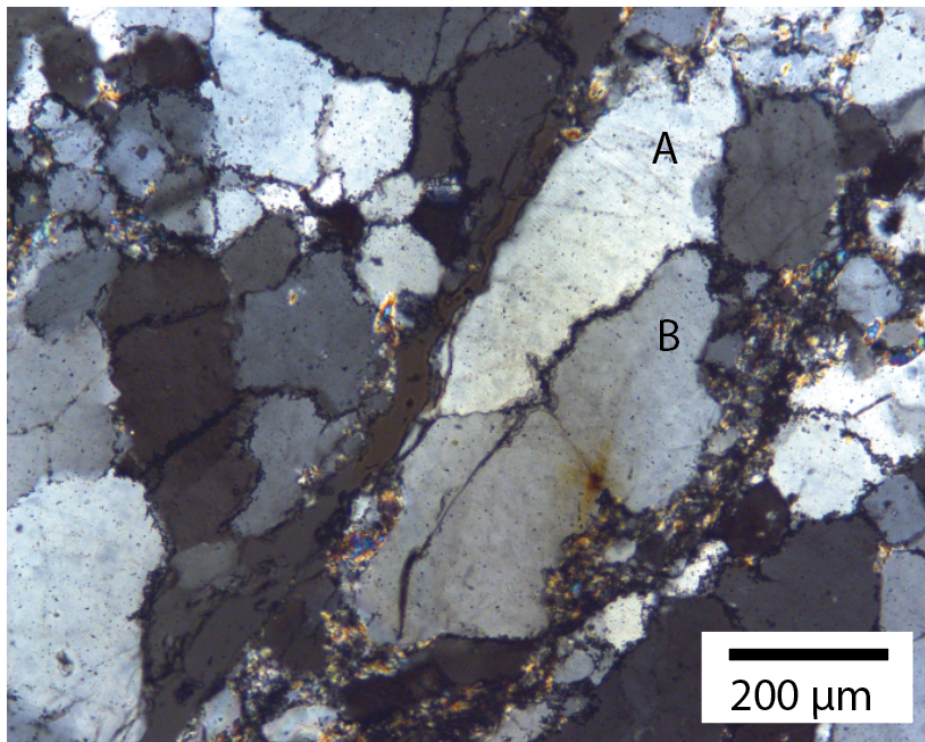
Figure 3.3: *Photo micrograph of Ko1_1553C in cross-polarized light at 10x magnification. Ko1 scan data presented below was collected over grains A and B. Deformation lamellae can be seen in grain A.*

3.3 Methodology

Synchrotron x-rays have the benefit of being a continuous (spanning many wavelengths) source of high intensity, high brightness x-rays. Compared to lab–based x-ray diffraction methods which irradiate a sample using much lower intensity and brightness, synchrotrons require a shorter exposure time than lab-based methods to measure enough signal to analyze, which therefore enables the collection of more data over a shorter period of time compared to lab-based methods. Most importantly synchrotron x-rays can be focused to a very small spot size. The polychromatic beam used in "Laue" diffraction satisfies a range of Bragg conditions which eliminates the need for sample rotation as in monochromatic diffraction. This simplifies data analysis and enables maps of the scanned grains to be easily reconstructed. The experiments presented in this thesis were performed at the Advanced Light Source beamline 12.3.2, the microdiffraction beamline using a polychromatic beam. At this beamline, the microfocused polychromatic beam has an energy range of 5-24 keV and a spot size of 1 µm diameter, which enables the reconstruction of high resolution strain maps over several grains on a thin section of quartzite.

3.4 Scan set up

From the accelerator storage ring, the polychromatic source light enters the end station where it passes through a series of slits and a pair of Kirk-Baez mirrors that reduce the spot size of the beam to 1µm. The beam exits the optics box through the beam pass and impinges upon the sample located on the translational stage tilted 45° to the beam. The diffraction signal is collected by the Dectris Pilatus 1M detector located above the sample stage and 90° from the incident beam (Figs. 3.4, 3.5)

A calibrant is used prior to data collection to create a calibration file for analysis. The material used as a calibrant is discussed below in Section 3.5. The calibrant is used to refine the positioning of the detector relative to the sample, which is necessary for accurate strain measurements. the surface of the sample is placed at the focal point of the x-ray beam by adjusting the Upper Stage Z position (Fig. 3.6) until the sample surface is at the focal point. During beamline commissioning at the start of every beamtime cycle, the laser and high magnification camera are calibrated to the position of the focal point of the x-ray beam, and a guide is placed on the camera monitor screen to indicate the position of the x-ray beam (Fig. 3.7). Most recently, this guide has been a green circle. When the sample is positioned in the focal point of the beam, the laser appears inside the green circle (Fig. 3.7b, c). Surficial topographic details such as grain boundaries, surface roughness, or copper arrows placed on the sample surface (e.g. Fig. 3.2a) will come into focus.

A small scan of the calibrant, approximately 100 images, is run and the calibration parameters are refined following indexation of the diffraction patterns. Spider lights on the end station are used to illuminate the sample properly, and on-line cameras are used to locate the areas of interest on the sample. The start (X & YSTART) and end (X & YEND)
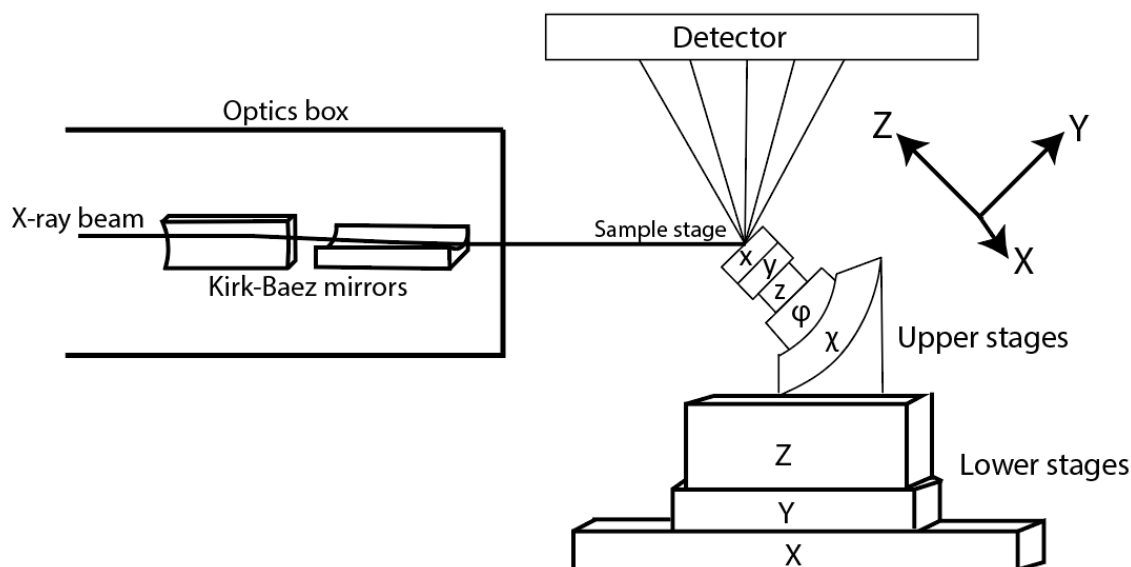
Figure 3.4: *Schematic of ALS beamline 12.3.2 in reflection geometry. X-ray beam enters the hutch from accelerator storage ring (at left). Prior to reaching the sample stage, the polychromatic beam spot size is reduced to 1 µm using the Kirk-Baez mirrors. The sample is located on translational stages used to position the sample. The detector to receive the signal and capture diffraction images is located above.*

coordinates, the step size (X & YSTEP), and the exposure time are programmed by the user, along with a scan name and file save location (Fig. 3.8). Exposure time depends on how well the sample diffracts and a test image should be taken (Fig. 3.8 "Take Single Frame") to test the correct exposure has been chosen for the sample. The estimated scan time is found in the "Remaining time" box in the lower right.

After the parameters have been set, the scan is started by pressing the green arrow in the upper left corner (Fig. 3.8). The scan area of the calibrant is intentionally small to avoid any variation in sample height that would require a change in focus. As the sample rasters around the scan area, a diffraction image (Fig. 3.9) is collected at each step which are later processed with softwares XMAS (Tamura, 2014) and XtalCAMP (Li et al., 2020).
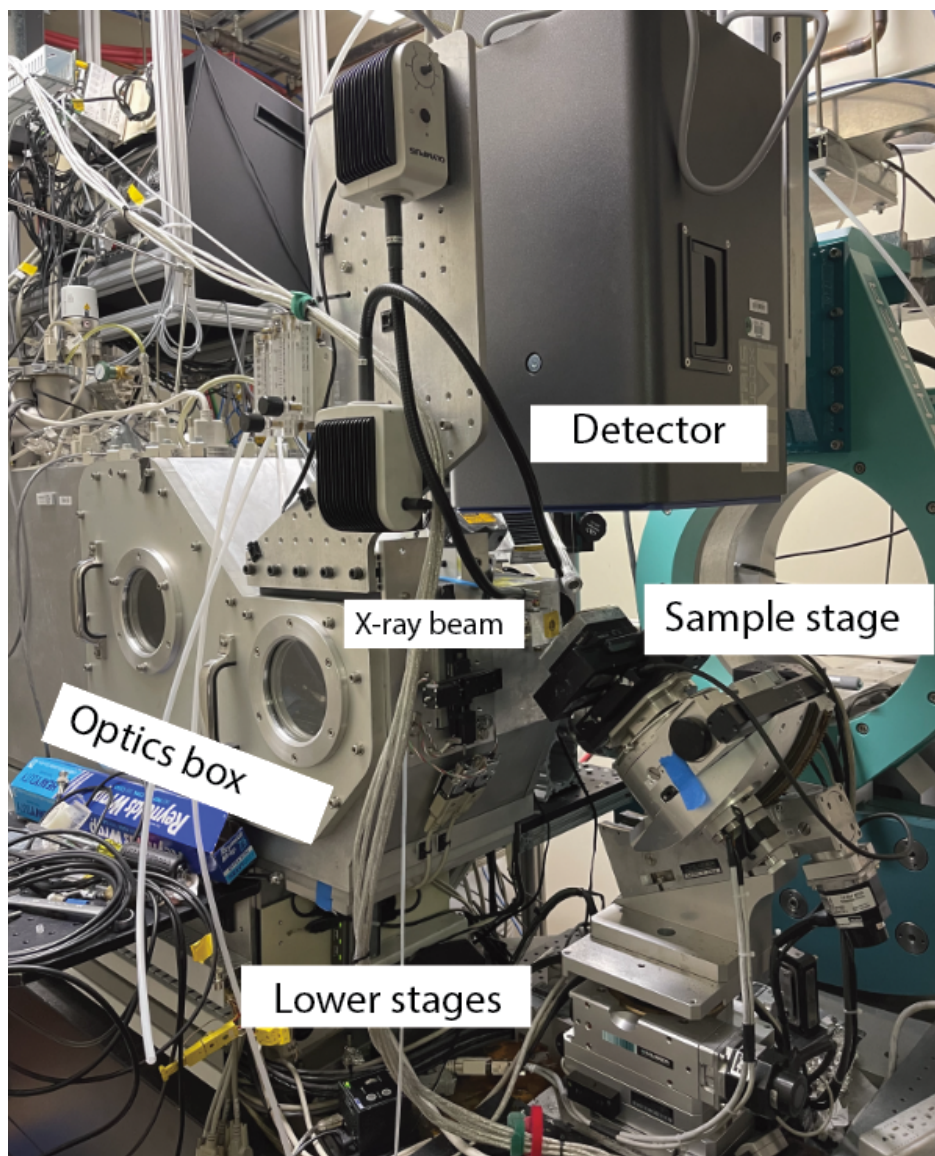
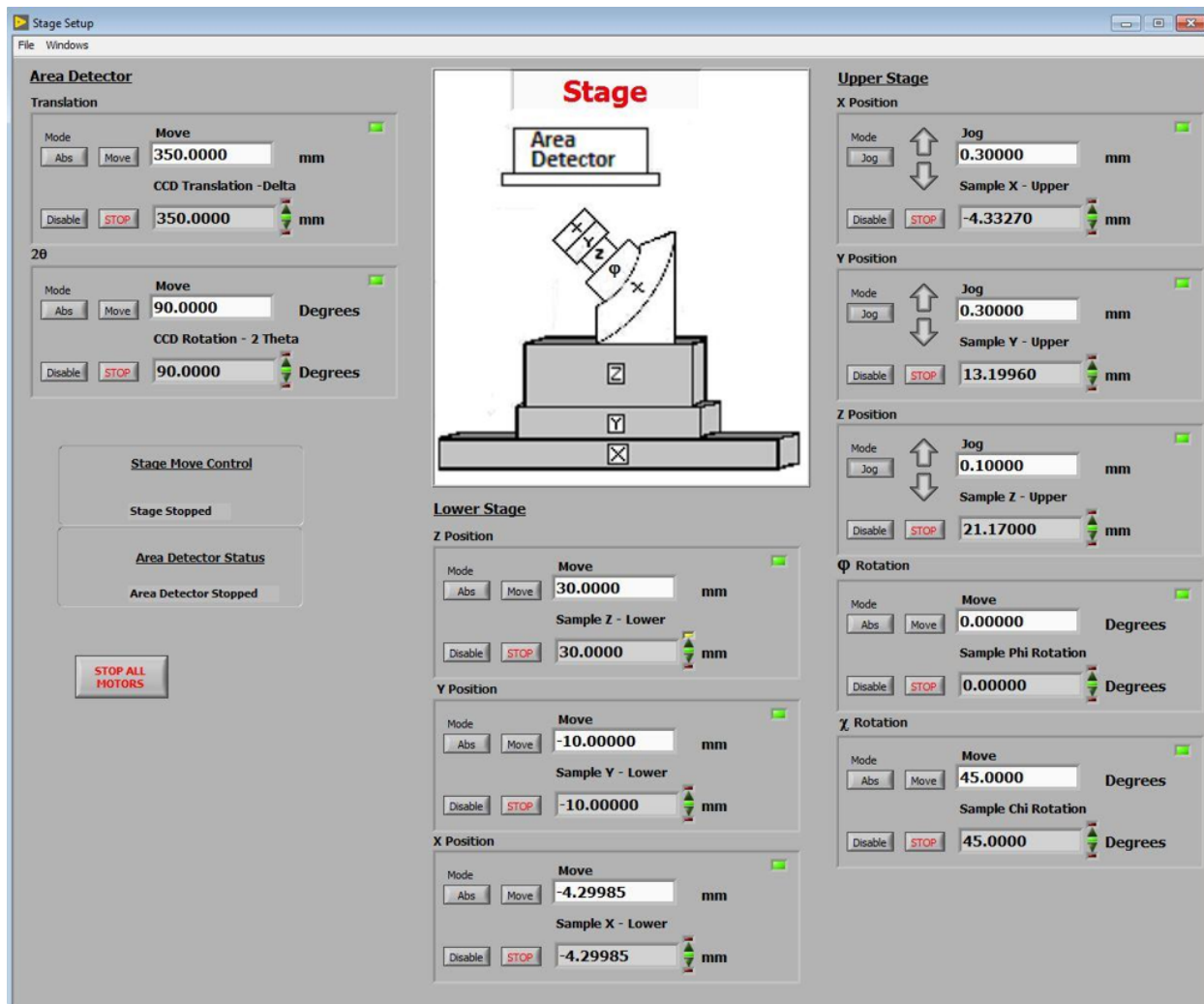**Figure 3.5:** *Photo of the ALS beamline 12.3.2 end station setup*

Figure 3.6: *LabView window used to move sample stages at ALS beamline 12.3.2*
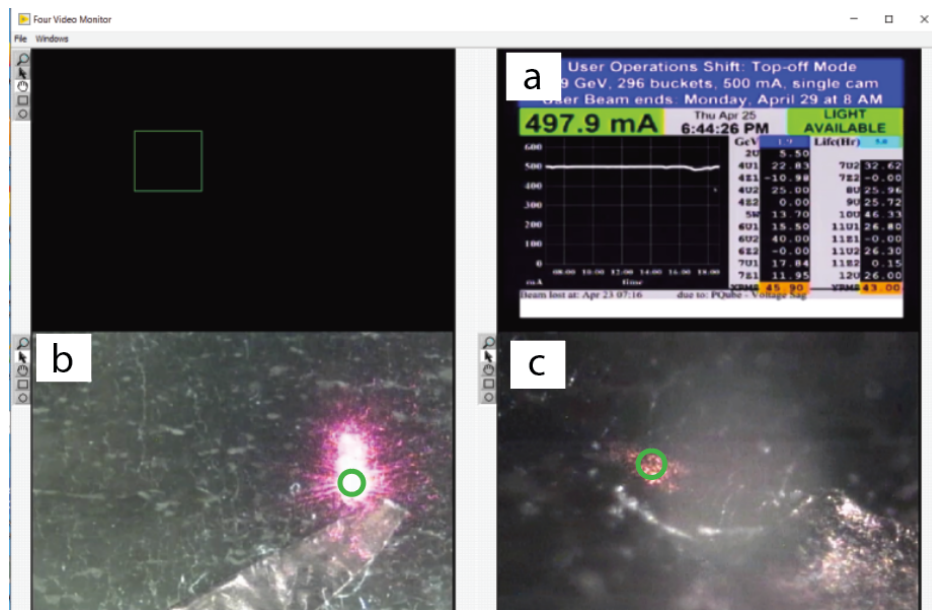
Figure 3.7: *Four Video Monitor screen at ALS beamline 12.3.2. (a) shows beam status, (b) is beamline camera, (c) is high magnification beamline camera. When the sample surface is aligned with the focal point of the beam, the laser appears inside the green circle in (b) and (c).*
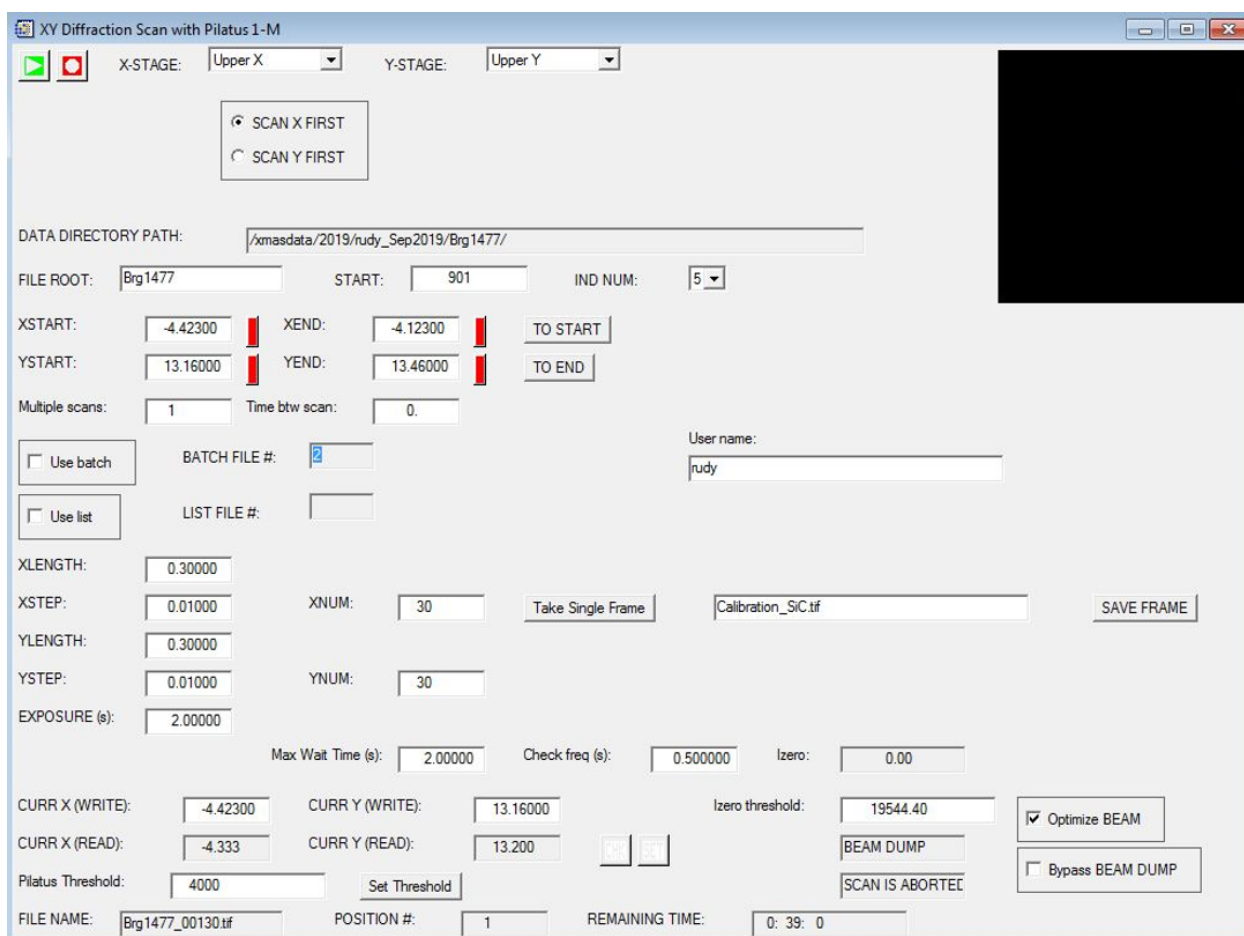
Figure 3.8: *XY Diffraction Scan with Pilatus window used to program scan parameters*
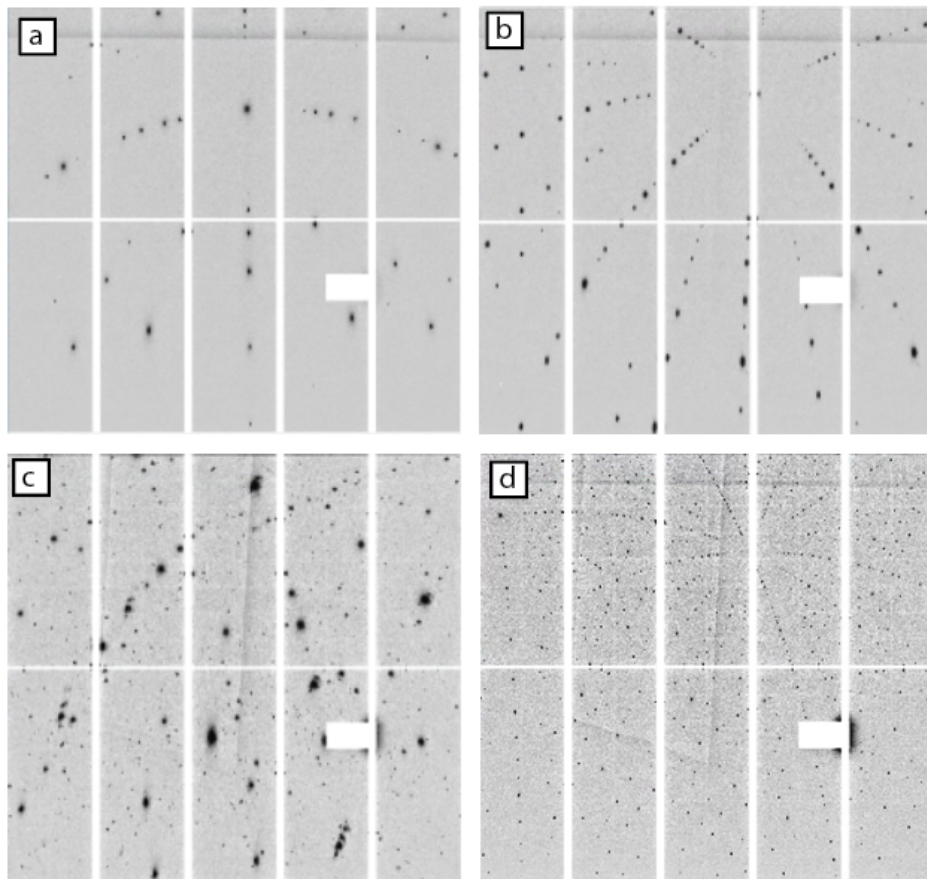
Figure 3.9: *Example diffraction image for different calibrants. (a) single crystal silicon, (b) single crystal synthetic quartz, (c) polysilicon, (d) single crystal YAG. White gaps are interstitial area between detector subpanels, and white rectangle in bottom right is a bad submodule that has been removed from the image.*

3.5 Indexation of diffraction patterns, and calibration

XMAS is used to calculate an orientation matrix of the diffracting grain, index the diffraction patterns (i.e. assign *hkl* Bragg indices to peaks), and calculate the deviatoric strain tensor. Prior to indexation, corrections are applied to each diffraction image. The frame-grabbing software from the detector performs flat field correction, and a custom beamline-specific code performs spatial correction. The last two are particularly important for strain refinement. Flat field correction removes effects of non-uniform illumination and differences in pixel sensitivity, and spatial correction correct any spatial distortion due to misalignment of the detector panels during manufacturing. And finally, the background signal caused by anomalous scattering is subtracted using XMAS (Tamura, 2014).

After the background is subtracted, peak positions are found using a Peak Finding routine (Fig. 3.10). A threshold value is used to distinguish peaks of a certain intensity from the background, and then the peak is fit with a 2D Gaussian function. A list of fitted peak positions is generated and sorted by integrated intensity values, starting with the brightest reflections.
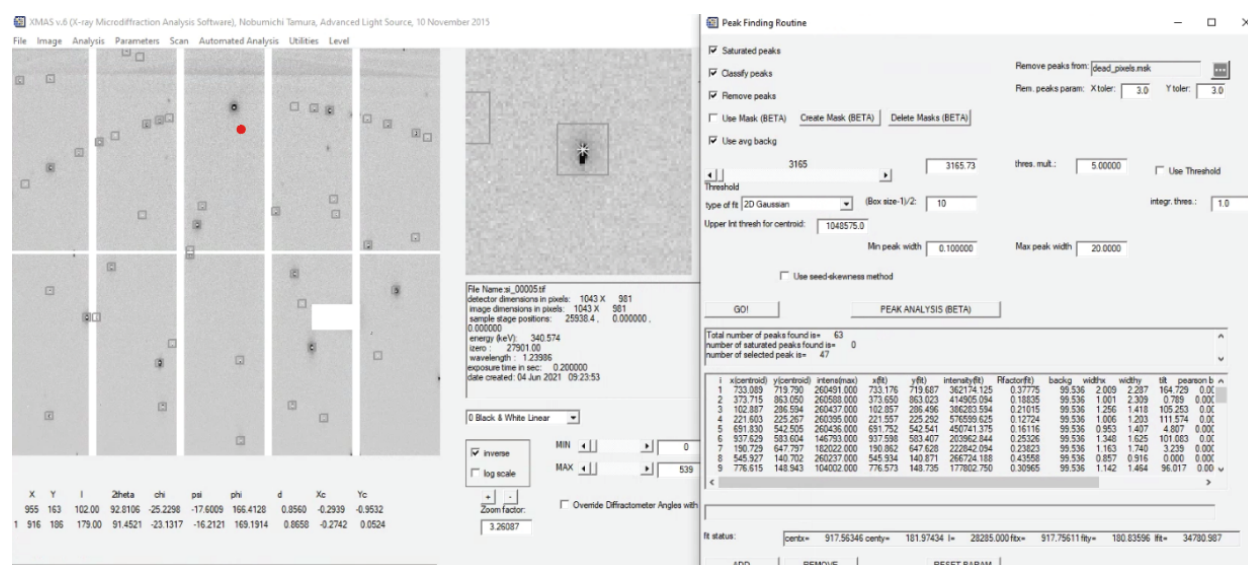

Figure 3.10: *Results of XMAS peak finding routine on a diffraction pattern of Si calibrant. (left) Diffraction image with fitted peaks outlined in gray boxes. Center coordinate of diffraction pattern marked with a red dot. (right) Peak Finding routine window where peak fitting parameters are set such as the threshold value and box size. List of fitted peaks in bottom of this window.*

To index the diffraction image, the angle between a pair of peaks is measured and compared to a list of angles between theoretical *hkls* that have been calculated based on the crystal structure, the parameters of which are specified in a crystal file. It is helpful to use a

calibration file from a previous beamtime with a similar set up to provide initial parameters to then refine. With these starting values, origin of scattering and the direction of the incident beam is known relative to the detector, and assuming elastic scattering ($|\mathbf{k}_{in}| = |\mathbf{k}_{out}|$) and the crystal structure, the direction of the experimental scattering vector is calculated ($\mathbf{q}_{exp} = \mathbf{k}_{out} - \mathbf{k}_{in}$). The angles between pairs of $\mathbf{q}_{exp}$ are calculated and tabulated. A corresponding table of angular differences between theoretical (zero strain) scattering vectors ($\mathbf{q}_{ref}$) are also tabulated, knowing the crystal structure and the energy of the incident beam. When a pair of *hkl*s with an angular difference within the user-set angular tolerance is found, a third reflection is added to the pair to make a triplet. Then, the process is repeated until a set of three theoretical *hkl*s with measured angles within the angular tolerance of the experimental values are found. This determines the orientation of the crystal, from which a list of reference peaks that are expected to be observed on the diffraction pattern is generated. Miller indices from this generated list are then assigned to peaks present on the diffraction pattern based on peak position (Fig. 3.11) (Tamura et al., 2003).
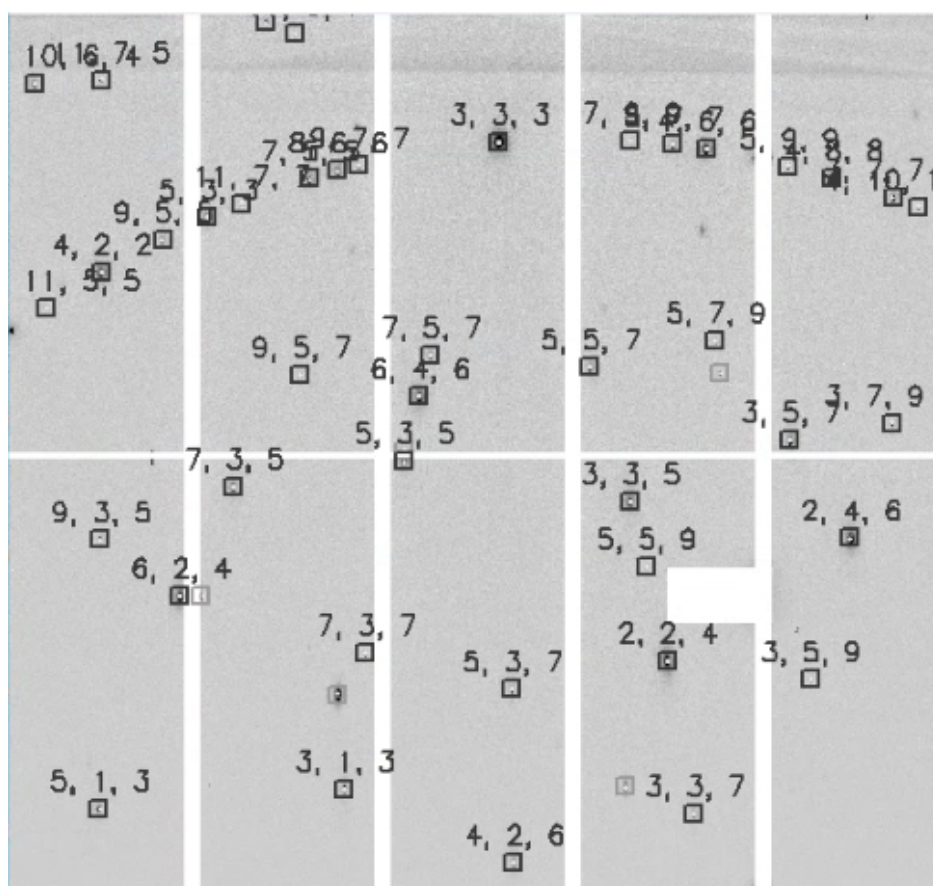

Figure 3.11: *Miller indices assigned to identified peaks in Si diffraction image (Fig. 3.9a)*

After an example diffraction pattern of the calibrant has been indexed, five independent calibration parameters are refined that define the positioning of the detector relative to the origin of diffraction in the sample: the coordinates of the center of the detector relative to the origin of scattering (xcent and ycent), the distance between the scattering origin and the detector, and two tilt parameters of the detector (pitch and yaw). These five parameters are selected in the Strain Refinement Parameters window (Fig. 3.12).
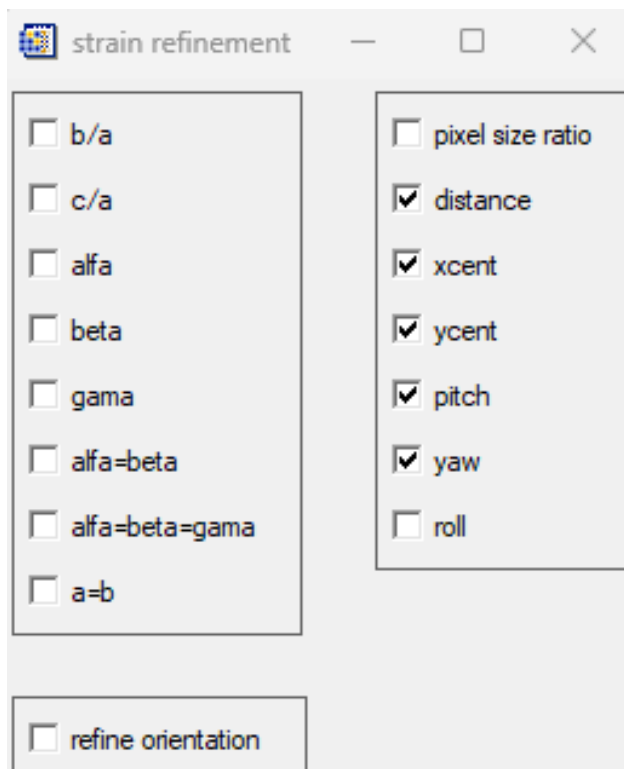

Figure 3.12: *Calibration parameters selected for refinement.*

The Strain Refinement/Calibration routine is run, and the calibration parameters are optimized to minimize the theoretical and experimental angular deviation between pairs of reflections visible on the diffraction pattern using the following function:

$$\alpha_0 = \sum_i w_i (\alpha_i^{th} - \alpha_i^{exp})^2 \div \sum_i w_i$$

where α_i^{th} and α_i^{exp} are the theoretical and experimental angular deviations between a pair of scattering vectors $\mathbf{q}_{exp}$, and w_i are weighting factors. This is first performed for a single diffraction pattern and a limited energy range (5-20 keV) and large angular tolerance (0.2 degrees). "Set new calibration" on the bottom of the strain refinement window is selected to apply the refined calibration parameters. The energy range is increased to its full range of 5-25 keV and angular tolerance is reduced to 0.1 degrees. The image is re-indexed, and

calibration parameter refinement is run again and the new calibration parameters are set. The indexation and calibration parameter refinement routine is applied to all of the diffraction images in the scan using Automated Analysis on the cluster, and the average value for each calibration parameter is entered into the calibration window (Fig. 3.13), a calibration file saved, and used for data analysis.

Figure 3.13: *Example calibration parameter window in XMAS*

Pros and cons of different calibrants

The choice of calibrant is critical for accurate determination of strain. There are a number of parameters that affect whether or not a calibrant will accurately calibrate the beamline geometry for the experiment, as discussed below. If beamline geometry is not calibrated accurately, the strain will be miscalculated. The pros and cons of different calibrants are listed in Table 3.1.

Number of reflections per diffraction pattern

The best calibrant has changed over the course of my PhD and I will describe the benefits and limitations of each below. An ideal calibrant is an unstrained crystal with well-determined lattice parameters and a large enough unit cell that produces a sufficient number of reflections on the diffraction pattern. A standard thin section of a synthetic quartz crystal has been used for its pure composition and well-known lattice parameters. A single crystal of silicon has also been used for the same reason. However, both calibrants, while they have a relatively pure composition and well-determined lattice parameters, also produce few reflections over the entire diffraction image ($\sim$40 reflections for Si, $\sim$80 reflections for quartz) and thus only a few reflections appear on each of the eight individual detector panels. This can cause an "orientation bias" and artificially introduce strain into the measurement (personal communication with N. Tamura, 2022). For this reason, a sample of crushed silicon was used ("polysilicon," Fig. 3.9c) which contains several, randomly oriented grains within the area of the x-ray probe with $\sim$600 reflections per image, thus reducing the possibility of an orientation bias error. However the fracture of the silicon into grains results in an uneven surface height of each grain which would result in variability in the refinement of calibration parameters. More recently, a yttrium aluminum garnet (YAG) single crystal mounted on a glass slide has been used which produces $\sim$400 reflections per pattern, thus reducing the possibility of orientation bias.

Sample transparency

If a calibrant is optically transparent, it can be difficult to determine the sample height at which the laser proxy is focused on its surface. Silicon is opaque and therefore it is easy to focus the laser on its surface compared to quartz or YAG mounted on a glass slide.

X-ray penetration and sample thickness

If the calibrant is made of a material that is transparent to x-rays, diffraction can originate throughout the thickness of the sample. Synthetic quartz has a thickness slightly greater than 30 μm, and the YAG crystal has a thickness of 560 μm. Due to the x-ray attenuation of quartz, the entire thickness of the sample can be probed by photon energies of 7 keV and greater (source: CXRO x-ray database). The polychromatic beam at 12.3.2 ranges from 5-25 keV, and therefore diffraction can originate along the entire thickness of the sample, which would result in variable ycent values. Similarly, the polychromatic beam at 12.3.2. has the potential to probe 200 μm thickness of the 570 μm thick YAG crystal calibrant, thus the scattering averages over the depth penetrated which can create an artificial strain error due to variability in the scattering origin through the thickness of the sample.

Table 3.1: *Scanning Laue microdiffraction calibrant comparison*

Calibrant	Lattice parameters (a, b, c, α, β, γ)	Optically transpar-ent?	X-ray transpar-ent?	Issues due to sample nature
Synthetic quartz	4.9135 Å, 4.9135 Å, 0.54052 Å, 90 °, 90°, 120°	Yes	Yes	Ycent, orientation bias
Silicon, single crystal	5.4300 Å, 5.4300 Å, 5.4300 Å, 90°, 90°, 90°	No	Yes	Orientation bias
Polysilicon	5.4300 Å, 5.4300 Å, 5.4300 Å, 90°, 90°, 90°	No	Yes	Ycent due to uneven surface
YAG	11.590 Å, 11.590 Å, 11.590 Å, 90°, 90°, 90°	Yes	No	Ycent

Calibrant conclusions

A calibrant with properties most similar to the sample is ideal. If the sample is an optically and x-ray transparent sample such as a thin section of quartzite, then a calibrant such as YAG would be the most ideal candidate to calibrate the the beamline geometry. This is because the calibrant and the sample need to be focused at the same spot to ensure there is minimal error caused by the calibration parameters used for sample analysis, and therefore the calibrant and the sample need to have similar properties such as optical transparency and x-ray transparency. Also, the calibrant and the sample need to interact with the laser in the same way to ensure that equivalent surfaces are measured on both the calibrant and the sample. And finally, the calibrant needs to have an adequate number of reflections per diffraction pattern to eliminate the potential for orientation bias. For these reasons, the YAG crystal is the best calibrant option for analyses of thin sections of quartz.

3.6 Data collection

A standard 30 µm thin section was created from each of the Hong Kong quartzites. Prior to collecting data at the beamline, the areas of interest on the thin section are found using a

Figure 3.14: *Topmost reflection (#1, rock surface) must be placed into the focal point of the beam (circled in pink) which is determined by the beamline scientist at the start of every accelerator run cycle. Reflections #2 and #3 are from the top and bottom of the glass slide.*

petrographic microscope and marked with a copper arrow. The copper arrow can be easily found using the beamline cameras. After the area of interest has been found and the scan parameters determined on the beamline, the sample must be placed into the focal point of the beam. A thin section has three sets of polished surfaces, the polished sample surface, the glass surface onto which the sample is epoxied, and the bottom surface of the glass slide, that produce three reflections as seen on the high-mag beamline camera (Fig. 3.14). It is important to keep the focus consistent between the calibrant and the sample by focusing on the same plane of the calibrant and sample. For example, if the focus of YAG on the glass slide was set to the top-most laser reflection (i.e. the surface of the YAG crystal), then the focus must be set to the top-most reflection (i.e. the surface) of the thin section. The top-most laser reflection is the surface of the sample, which can be verified by seeing the details of the sample surface, such as grain boundaries, come into focus. Large scans can vary in sample height due to variability in the sample polish and sample mounting, so it is best to keep the scans no larger than a few millimeters in size to avoid the need to change focus during the scan. It is best practice to check the focus of the beam on the sample surface at several locations in the scan area to ensure it is adequate for the entirety of the scan. At this point, it is worth mentioning briefly that the point of origin of the reflecting rays can be refined during data analysis using a strain minimization technique, explained in Section 3.7. This is important because if the sample is x-ray transparent, due to its composition and thickness, the origin of scattering may vary throughout the scan.

Once the sample has been set into focus, the scan area is programmed by the user. Spider lights on the end station are used to illuminate the sample properly, and on-line cameras are used to locate the areas of interest on the sample. The scan parameters are programmed by the user (Fig. 3.8). Each scan is usually a couple millimeters in either direction, and step size

is usually between 2 to 15 µm but is dependent on the grain size and the desired resolution of the scan. Exposure time for each diffraction pattern depends on how well the sample diffracts and a test image should be taken (Fig. 3.8 "Take Single Frame") to test the correct exposure has been chosen for the sample. A typical exposure time is 0.5 seconds. Prior to starting the scan, I recommend checking the focus at both the start and end coordinates to make sure the correct focus has been chosen as sample height can vary across a thin section. Samples with more plastic deformation produce weak, broad diffraction peaks and require longer exposure than samples with less plastic deformation. A test image is taken at several places in the scan area to determine the optimal settings such as exposure and focus, and to check the quality of the diffraction patterns. The quality of diffraction peaks can vary within the sample, intragranularly as well as intergranularly, depending on the degree of plastic deformation. Peak shape is also affected by the plastic deformation in the sample (Barabash et al., 2003). An average scan collects at least 10,000 diffraction patterns, and takes 8-12 hours to complete.

3.7 Strain Calculation from Diffraction Patterns

Strain distorts the crystal unit cell into a triclinic shape. The strain of the crystal lattice is measured from the diffraction patterns. For each diffraction pattern, the deviatoric strain tensor is determined, from which the principal strain tensor is calculated. This deviatoric strain tensor describes the difference between an ideal single crystal (in this case, quartz) and the distorted crystal measured during the experiment. With Laue diffraction, the dilatational strain and therefore the total strain tensor cannot be measured unless an energy scan is also performed to measure the energy associated with each diffraction peak. I did not perform energy scans because they add a significant amount of time to each scan, and they are also not necessary for determining the principal strain ellipsoid which is used to determine the principal stress orientation which is the goal of this project.

After the diffraction pattern has been indexed using the procedure explained Section 3.5, the strain can be calculated. The strain is refined using the same minimization procedure used to refine the calibration parameters, but instead the beamline geometry parameters are fixed and lattice parameter ratios and angles are refined (Fig. 3.15). As mentioned before, absolute lattice parameters cannot be determined with Laue microdiffraction without an energy scan because of the use of polychromatic x-rays. Therefore, the b/a, c/a ratios are refined, as well as the unit cell angles α, β, γ.

The total strain tensor (ϵ_{ij}) is the sum of the dilatational strain tensor (Δ_{ij}) which describes the change in unit cell volume, and cannot be measured with Laue microdiffraction without an energy scan, and the deviatoric strain tensor (ϵ'_{ij}) which describes the change in shape of the unit cell (Fig. 3.16a) : $\epsilon_{ij} = \Delta_{ij} + \epsilon'_{ij}$ where

$$\Delta_{ij} = \begin{bmatrix} \delta & 0 & 0 \\ 0 & \delta & 0 \\ 0 & 0 & \delta \end{bmatrix}$$

and

$$\epsilon_{ij}' = \begin{bmatrix} \epsilon_{11}' & \epsilon_{12} & \epsilon_{13} \\ \epsilon_{12} & \epsilon_{22}' & \epsilon_{23} \\ \epsilon_{13} & \epsilon_{23} & \epsilon_{33}' \end{bmatrix}$$

The deviatoric strain tensor is calculated in crystal coordinate system based on the angular deviation of experimental and theoretical peak positions. It is then transformed from the coordinate system of the unit cell to the sample coordinate system $(x,\ y,\ z)$ (i.e. the laboratory coordinate system) using the crystal's orientation matrix M, generated by XMAS, and transformation $\epsilon_{xyz}' = M\epsilon_{ij}' M^T$ such that

$$\epsilon_{xyz}' = \begin{bmatrix} \epsilon_{xx}' & \epsilon_{xy} & \epsilon_{xz} \\ \epsilon_{yx} & \epsilon_{yy}' & \epsilon_{yz} \\ \epsilon_{zx} & \epsilon_{zy} & \epsilon_{zz}' \end{bmatrix}$$

An Eigen decomposition of ϵ_{xyz}' provides the eigenvalues and eigenvectors of the deviatoric strain matrix, which are equivalent to the axes of the principal strain ellipsoid in sample coordinates; scaled by the eigenvalues, the longest axis is equivalent to the axis of primary extension, the shortest axis to the axis of primary compression, and the intermediate axis is between the two (Fig. 3.16b).

The crystal orientation and strain is calculated using XMAS. The grain indexation and strain refinement routine is performed on every diffraction image of the scan using the XMAS cluster, part of the supercluster at Lawrence Berkeley National Lab. Routine files (.dat) that contain the information on how to process the diffraction images for a scan, such as indexation and strain refinement parameters, are scheduled to the cluster which performs the analysis. The output file is an SEQ file, a binary file which can only be opened in XMAS or XtalCAMP. XtalCAMP is a Matlab code software that is used to perform the Eigen decomposition, calculate the principal strain ellipsoid for each diffraction pattern, and generate the high resolution area maps of the data (Li et al., 2020). Load the SEQ file into XtalCAMP by right clicking on in the main window and selecting "Import μXRD SEQ file" (Fig. 3.17). The data from the SEQ is displayed like a table, with each column containing a data field and each row the data from a single diffraction image. Check to make sure the crystal file is correct by choosing Crystal from the top menu, then Crystal Structure, opening the crystal structure window from which the correct crystal file for your analysis can be chosen. This should be the same crystal file used in the XMAS analysis. Note that the crystal file does not affect the Eigen decomposition, which only uses the calculated deviatoric strain tensor, but it does affect the orientation of the plotted grains. Then, the data is cleaned by opening the 2D Mapping window (Plot>2D Mapping) and any unindexed diffraction patterns or those indexed very poorly are filtered out.
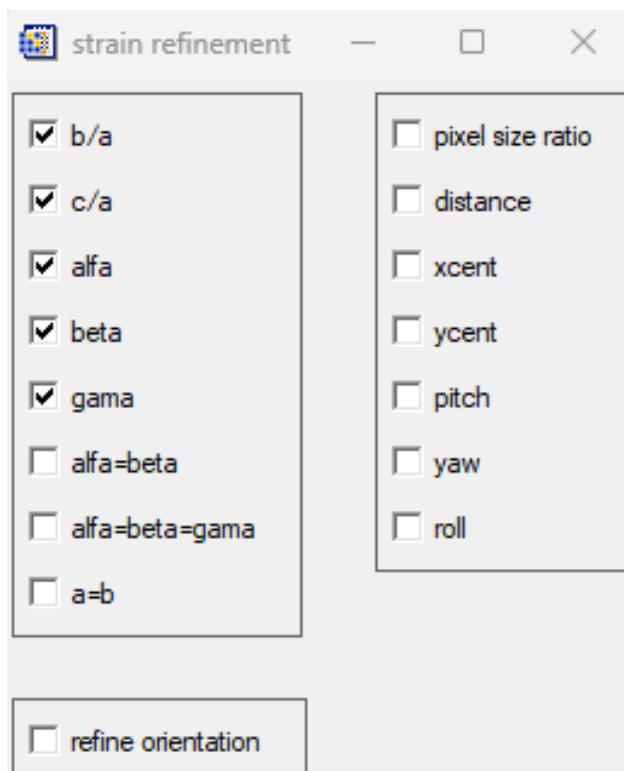
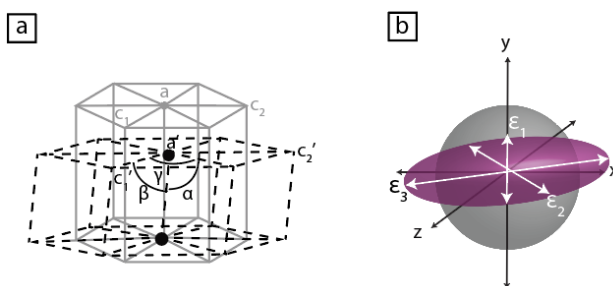**Figure 3.15:** XMAS strain parameters selected for refinement.

Figure 3.16: Deviatoric strain tensor describes the change in shape of the unit cell (a). An Eigen decomposition of the tensor produces the principal strain ellipsoid (b).

Figure 3.17: *SEQ file loaded into XtalCAMP. Each row contains the data for a single diffraction image of the scan. Column headers indicate different data fields.*

The Selection tool in the 2D mapping window is used to filter the data based on up to four parameters. To filter out only those diffraction patterns that have been poorly indexed, Selection 1 is chosen, and then Nindex as the parameter, setting the minimum to 19 and maximum to 200 or so (Fig. 3.18). The Nindex value is the number of indexed reflections of the diffraction pattern. Filtering out diffraction patterns with Nindex less than 20 peaks for quartz is reasonable. This subset of data is then saved by clicking Output Selection button in the upper right of the window. Choose YES to calculate boundary data, and the data is saved as an "Orient" text file. It is worth mentioning that the crystal orientation as described by Euler angles, a series of three angles/rotations that bring two coordinate systems into coincidence, have several different conventions that can be used to report these angles, all of which have different series of rotations. The convention describe used in XtalCAMP differs from the convention used in XMAS and thus the two softwares report different Euler
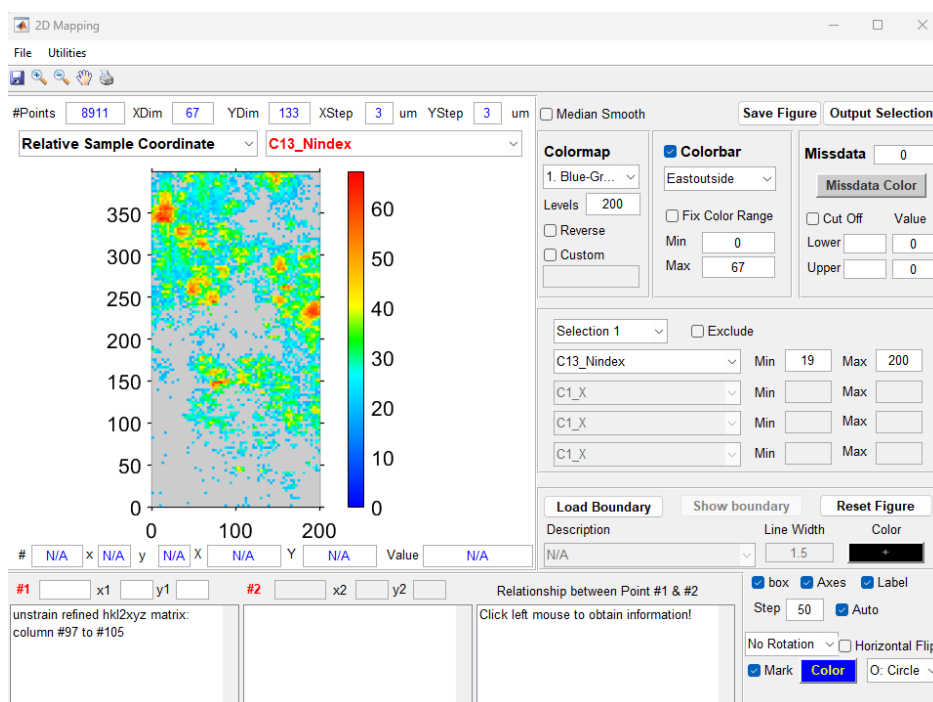
Figure 3.18: *XtalCAMP 2D mapping window used to visualize the data as a 2D map and filter the data*

angle values. At the point of converting the SEQ to an orient file, the Euler angles get re-saved in the XtalCAMP convention. The XtalCAMP convention agrees with the electron backscatter diffraction (EBSD) data collected with a scanning electron microscope (SEM) and therefore the Euler angles from the Orient files are used in discussion. SEM-EBSD data is collected with a ZEISS EVO MA10 tungsten filament scanning electron microscope and an EDAX EDS detector and Ametek TSL Digiview detector, and processed using EDAX OIM softwaver V 6.1.3.

3.8 Results: HSM_1159A

The filtered dataset is then used for subsequent analysis. The Orient text file is loaded into XtalCAMP (Rt click on main window>Import µXRD Text File) and used to plot grain orientation (Fig. 3.19) and deviatoric strain maps. The 1000 x 1500 µm scan of HSM was collected with a step size of 7 µm. Diffraction images with less than 20 reflections were removed from the analysis (gray pixels). Many of the diffraction patterns had more than 20 indexable peaks, with the most well-indexed peaks towards the interior of each grain, with less peaks being indexed closer to the grain boundaries (Fig. 3.19a). (Note: I do not show the indexation results for an example diffraction image for the data because the indexation

performed using the Cluster Automated Analysis, the results of which are not visualized, produces different results than when performed on a local computer, and thus the visual from the local indexation would not be representative of the data.) This is likely due to an increase in plastic deformation towards grain boundaries, where dislocations tend to move and congregate. Plastic deformation throughout the scan was relatively low, as can be seen by the mostly uniform peak shape in the diffraction pattern (Fig. 3.19b). Grain orientations show that the majority of grains in the scan are similarly oriented between Euler 1 angles of 140° to 150° (blue), or 320° to 340° (red), Euler 2 angles of 70° to 80° (orange), and 60° Dauphiné twins are visible in Euler 3 map (red/blue and yellow/green) (Fig. 3.19c, d, e).

XtalCAMP is also used to plot maps showing the deviatoric strain components. Figure 3.20a shows the deviatoric strain components of HSM_1159A plotted in 2D. The most compressive strain (blue, negative) is observed in the y-direction (YY), and the most extensive strain (red, positive) is observed in the z-direction (ZZ) (perpendicular to the plane of viewing), with the x-direction (XX) as the intermediate direction. It can be helpful to plot the strain magnitudes from the maps as histograms, which clearly show the distribution of positive to negative values. In this scan, the deviatoric strain in the YY direction produced the most negative distribution of strain magnitude values, and ZZ the most positive distribution of strain magnitude values (Fig. 3.20b).

Using the new subset of well-indexed diffraction patterns, the Eigen decomposition is performed on the strain tensor of each diffraction pattern and the principal strains are calculated and output into a new text file. The Orient text file is loaded into XtalCAMP (Rt click on main window>Import μXRD Text File) and then select Strain/Stress>Principal Strain/Stress from the top menu. The Principal Strain & Stress window will open and "Save BearTex .cpt file" should be selected to create a file of Euler angles that describe the orientation of the principal strain ellipsoid relative to sample coordinates. This file is used to plot the principal strain pole figures in BEARTEX (Fig. 3.21). Click Output Data and the principal strain file will be saved as a text file.

To plot the components of the principal strain tensor in 2D, the principal strain text file is loaded into XtalCAMP (Rt click on main window> Import Ordinary Text File) and the 2D Mapping window is opened (Fig. 3.22). The desired component of the principal strain tensor is chosen, and the magnitude of that component is displayed per the color bar scale. To plot the orientation of the component, the Projected Vectors on XY Plane window is opened (Utilities>Projected Vectors on XY Plane). The vector components of the tensor component are selected (in this case the x, y, and z components of the ϵ_1 axis). The vector projections are added to every 6th diffraction image, as specified in the lower right of the window, by clicking "Add Arrow" button.

Principal strain maps of HSM_1159A show that the principal axes of compression (ϵ_1) are more or less aligned vertically, along the y-axis, and the intermediate axes (ϵ_2) are aligned horizontally, along the x-axis. The axes of extension (ϵ_3) have a great z-component that reduces the apparent length of the vector overlay in Fig. 3.23.

Equivalent strain was used to estimate the magnitude of the deviatoric strain. Equivalent
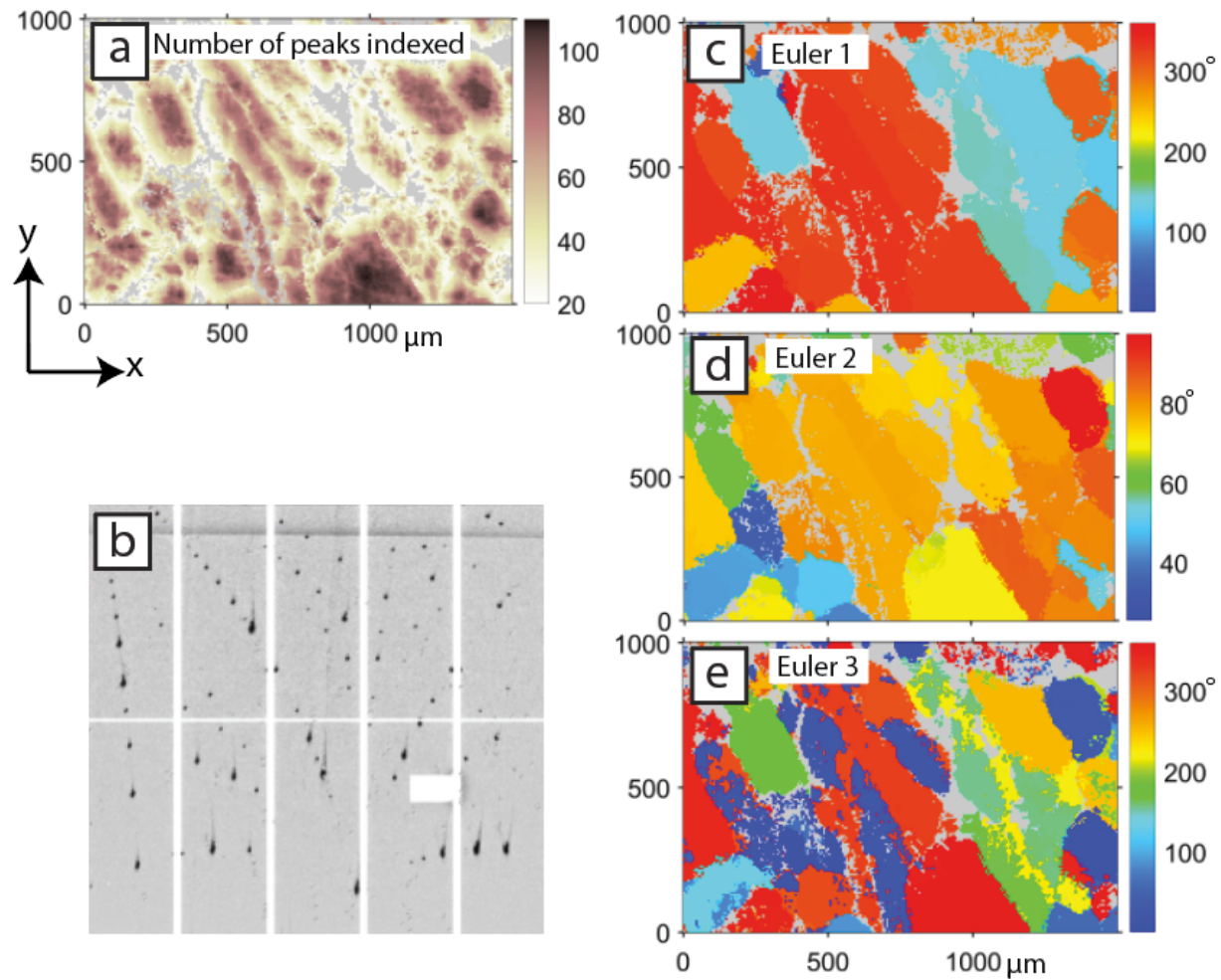
Figure 3.19: *Maps of HSM_1159A scan area plotted as 2D maps. Each pixel shows the data from one diffraction pattern. Gray pixels are those with number of peaks indexed below 20 and were thus removed from analysis. (a) map showing number of peaks indexed; (b) example of diffraction pattern from HSM_1159A; (c-e) maps of the three Euler angles that are rotations to bring crystal coordinates to coincidence with sample coordinates and define the grain orientations.*
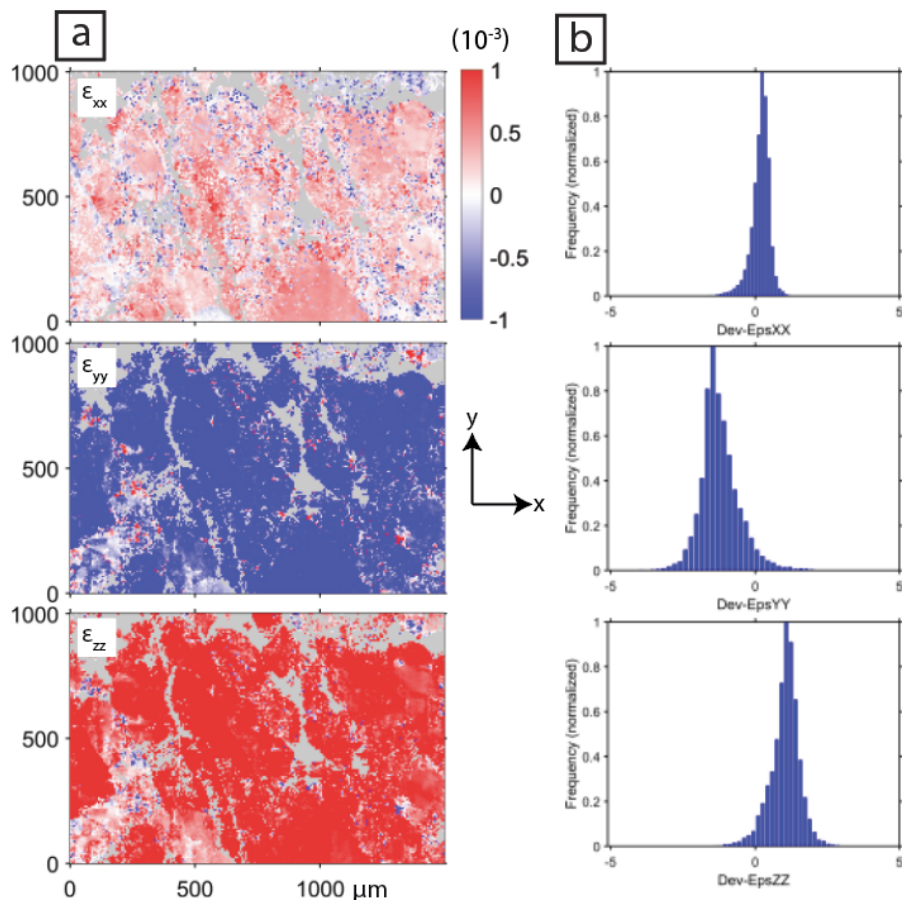
Figure 3.20: *Maps of HSM_1159A deviatoric strain in sample reference coordinates (x,y,z). (a) maps of the scan area showing the diagonal components of the deviatoric strain tensor. Color indicates magnitude of strain, red being positive (extension) and blue is negative (compression). (b) Histograms showing distribution of the deviatoric strain magnitude of the corresponding tensor component shown in (a).*
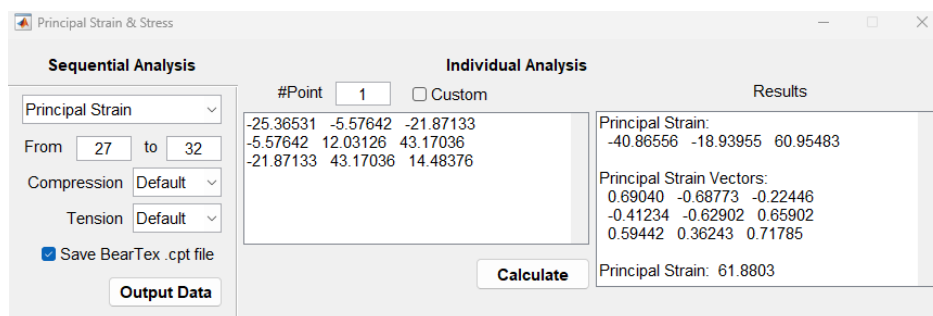
Figure 3.21: *Principal Strain & Stress window in XtalCAMP*
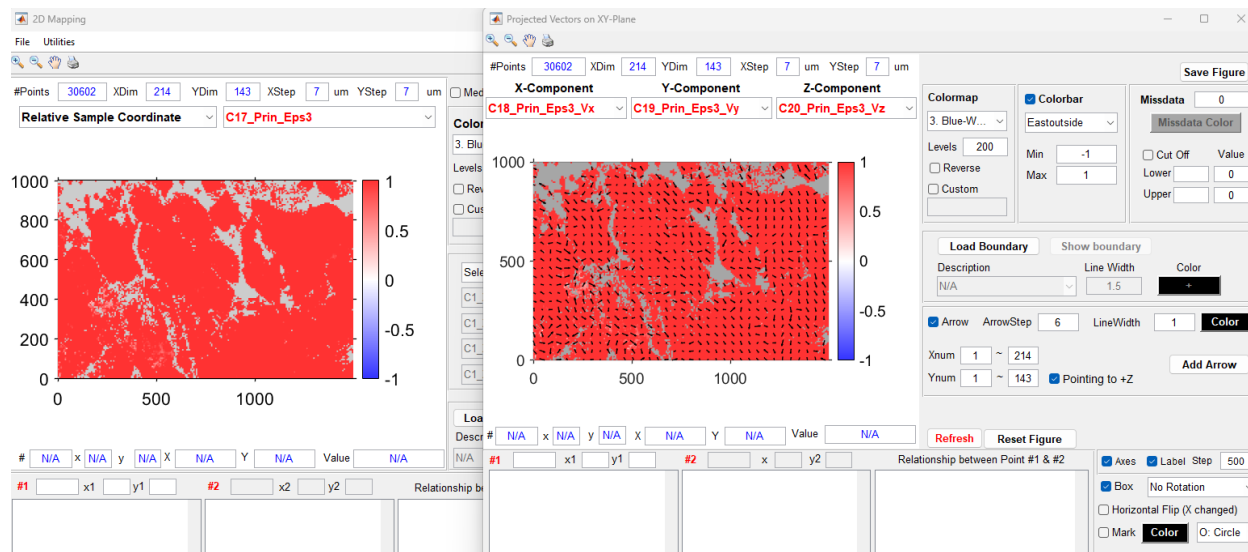
Figure 3.22: *XtalCAMP windows for plotting principal strain maps*

strain is calculated by (Liu, 2005):

$$\epsilon = \frac{1}{3}\sqrt{2[(\epsilon_1 - \epsilon_2)^2 + (\epsilon_2 - \epsilon_3)^2 + (\epsilon_3 - \epsilon_1)^2]}$$

where $\epsilon_1, \epsilon_2, \epsilon_3$ are principal strains. The equivalent strain for HSM was calculated to be approximately 2.5 x 10^{-3} (Fig. 3.24a). Equivalent stress is calculated by applying Hooke's law: $\sigma = \epsilon C_{ij}$; the strain tensor is converted to the stress tensor by multiplying the strain tensor by the material's elasticity tensor (C_{ij}). Equivalent stress calculated for HSM_1159A is approximately 375 MPa (Fig. 3.24b). Chan and Alvarez (2023) predict that an explosion structure that originates at 10 km depth along a geothermal gradient of 25°C/km would produce a pressure of 270 MPa upon conversion from liquid to gas as the volume ascends through the crust, which is on the same order as the measure of stress I measured. The equivalent strain is higher than that calculated for quartzite from the Vredefort impact site (Chen et al., 2011) which could be due to improvements in calibration and data analysis since 2011, as well as proximity to the force. The Vredefort quartzite was sampled 30 km NE of the impact site and may have partially recovered in the two billion years since its formation. Comparatively, HSM_1159A was collected from a silicified vein which contains explosion structures, and thus HSM could potentially have experienced a greater force than the quartzite from the Vredefort crater.

Pole figures are used to visualize the orientation of the principal strain axes over the entire scan relative to the sample coordinates in three dimensions for all diffraction patterns. BEARTEX software and the cpt output file created by XtalCAMP. are used to create pole figures. The cpt file is a text file that contains the set of Euler angles used to describe the orientation of the principal coordinate system for each diffraction pattern in the orient file.
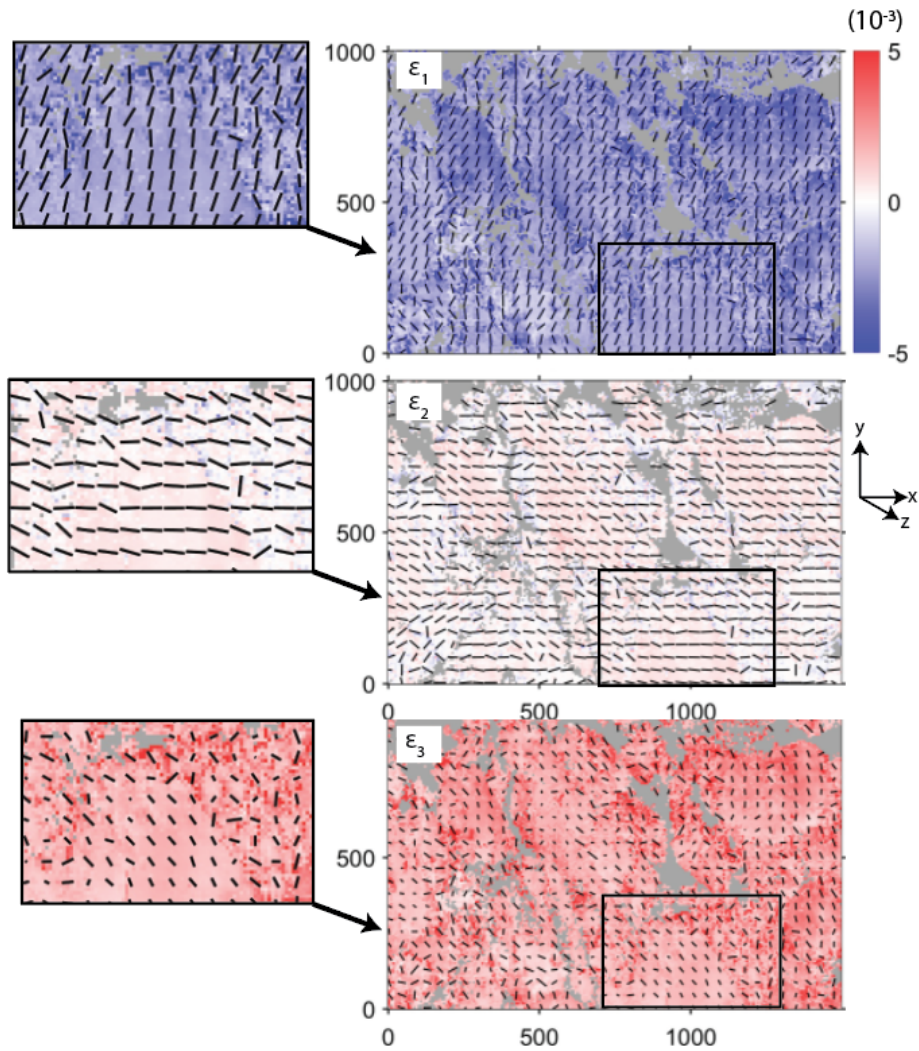
Figure 3.23: *Maps of HSM_1159A principal axes of compression (ϵ_1), extension (ϵ_3), and the intermediate axis (ϵ_2) plotted as maps in sample coordinate system (x,y,z). The area in the black rectangle has been magnified (left) for easier viewing. Color indicates the magnitude of compression (blue) and extension (red). Unindexed pixels removed from analysis are gray. The orientation of the principal axes are projected onto the xy plane as black lines for every 6th diffraction pattern. The greater the z-component, the shorter the line appears.*
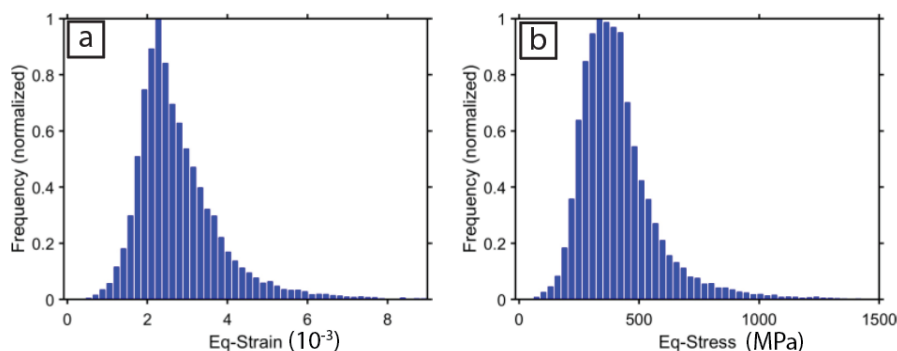
Figure 3.24: *Equivalent strain and equivalent stress distribution for HSM_1159A*
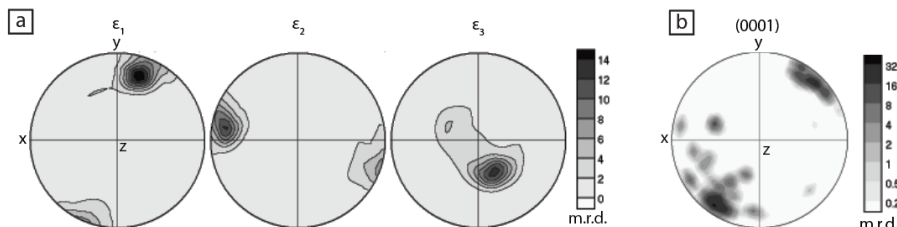
Figure 3.25: *HSM_1159A (a) crystallographic pole figure showing the orientation of c-axes (0001) relative to sample coordinates. (b) principal axes of compression (ϵ_1), intermediate (ϵ_2), and extension (ϵ_3) plotted as equal area projection pole figures relative to sample coordinates (x,y,z) (Fig. 3.19). Maxima are in multiples of random distribution (m.r.d.).*

This file is used to create the orientation distribution function for the principal axes using the INOR program, which is then smoothed using the SMOO program. The desired orientations are selected in the PCAL program, which are then plotted onto equal area projections using the PING program.

Principal strain pole figures show the orientation of principal strain data that is displayed as an overlay in 2D maps (Fig.3.23) as equal area plots in three dimensions (Fig. 3.25a). Pole figures can be useful to visualize the orientation of the overall strain ellipsoid for the scan because they can be used to plot the principal strain axes for every diffraction image, where as only a sub-sampling of the orientation data can be displayed on the 2D maps, as shown in Figure3.23, is every 6th image.

The principal axes of compression (Fig. 3.25a) are aligned with the c-axes of the quartz grains in HSM_1159A (Fig. 3.25b). Quartz grains often recrystallize with their c-axes aligned with the principal axis of compression (Hobbs, 1968) and the long axes of the grains are often oriented perpendicular to the axis of compression (Wenk et al., 2020). The principal axes of extension are perpendicular and are closely aligned with the z-axis. For this sample,

the paleostress orientation, especially the principal axis of compression, is in agreement with the presumed orientation of stress based on the crystallographic axes and grain morphology.

3.9   Results: Ko1_1553C

The same methodology used to measure the strain in HSM_1159A was applied to a sample from an explosion structure from the breccia dike (Ko1_1553C). A 200 x 400µm scan of Ko1_1553C was captured with a step size of 3µm. This area was selected because it scanned over a grain showing deformation lamellae (Fig. 3.26a, top grain) and a grain without deformation lamellae was chosen (Fig. 3.26a, bottom grain). The grains in this scan showed high levels of plastic deformation as evidenced by broad, non-uniform peak shapes (Fig. 3.26b) and as a result many diffraction patterns had less than 20 indexable reflections and were removed from analysis. The grain orientation measured by µXRD was confirmed using scanning electron microscopy electron backscatter detection (SEM-EBSD), as the Euler 2 angles are only 2 degrees off from the two methods (Fig. 3.26c), and Euler 3 maps show the same Dauphiné twin boundaries (Fig. 3.26d) with a misorientation of 60° (dark blue/light blue for µXRD and green/pink for EBSD). Compared to HSM_1159A, there is no clear directionality in the measured deviatoric strain for Ko1_1553C; the three diagonal components of the deviatoric strain tensor show an almost equal distribution of positive and negative strain (Fig. 3.27). While grain boundaries are visible in the Euler maps (Fig. 3.26c, d), grain boundaries are not visible in the deviatoric strain maps, and there appears to be no variation in intergranular and intragranular strain (Fig. 3.27).

The orientations of the principal strain axes are also ambiguous. Maps of the scan show that the principal axes of compression and extension are more or less oriented vertically along the y-axis (Fig. 3.28a). When plotted as pole figures, it becomes clear that the axes of compression and extension are coincident, with two maxima halfway between the y- and z-axes with minimal components in the x-direction (Fig. 3.28b). There is some variability, however, that distributes the principal compression and extension maxima as a ring around the three axes, with vectors inclined to the z-axis at approximately 45°. For completeness, the c-axes of the grains in the scan appear to have no relation to the principal axes of compression (Fig. 3.28c), as was observed in HSM_1159A(Fig. 3.25).

Ko1_1553C is a naturally deformed sample and its stress history is unknown. And unlike the recrystallized quartz in HSM_1159A, the grain morphology and c-axis orientation of Ko1_1553C show no clear relation to the measured strain. These results call into question the accuracy and of the methodology to determine the orientation of paleostress from measured residual strain.
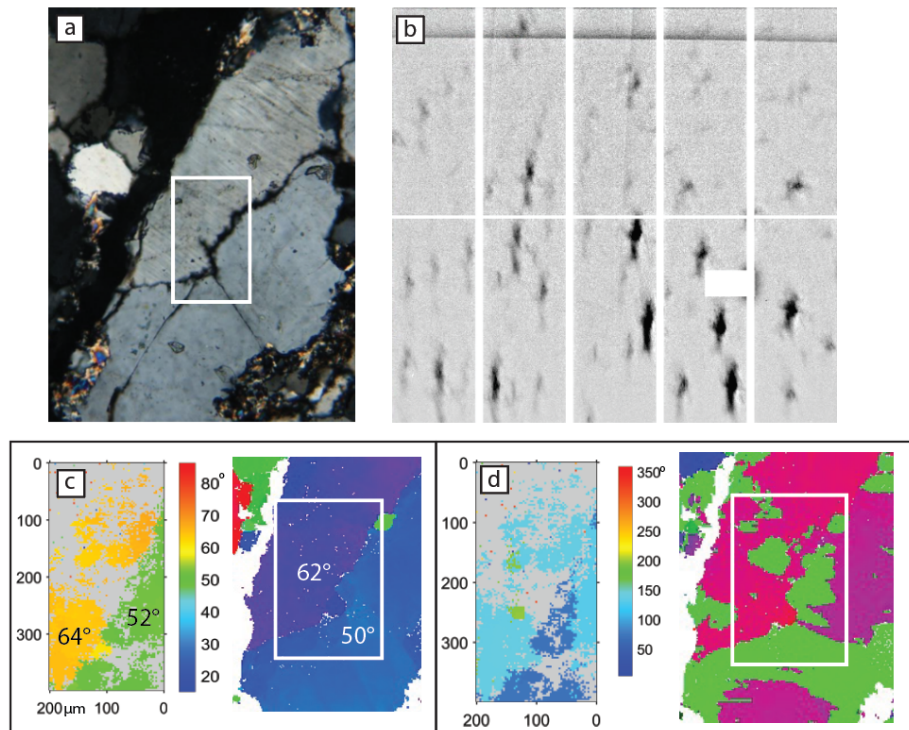
Figure 3.26: *Ko1_1553C (a) cross polarized micrograph. Scan area is indicated with a white rectangle. (b) Example diffraction pattern from Ko1_1553C. (c) Euler 2 angles as determined by µXRD (left) and EBSD (right). (d) Euler 3 map as determined by µXRD (left) and EBSD (right). Note that the µXRD scans have been rotated such that the grain boundaries are in the same orientation as the micrograph and EBSD scan.*
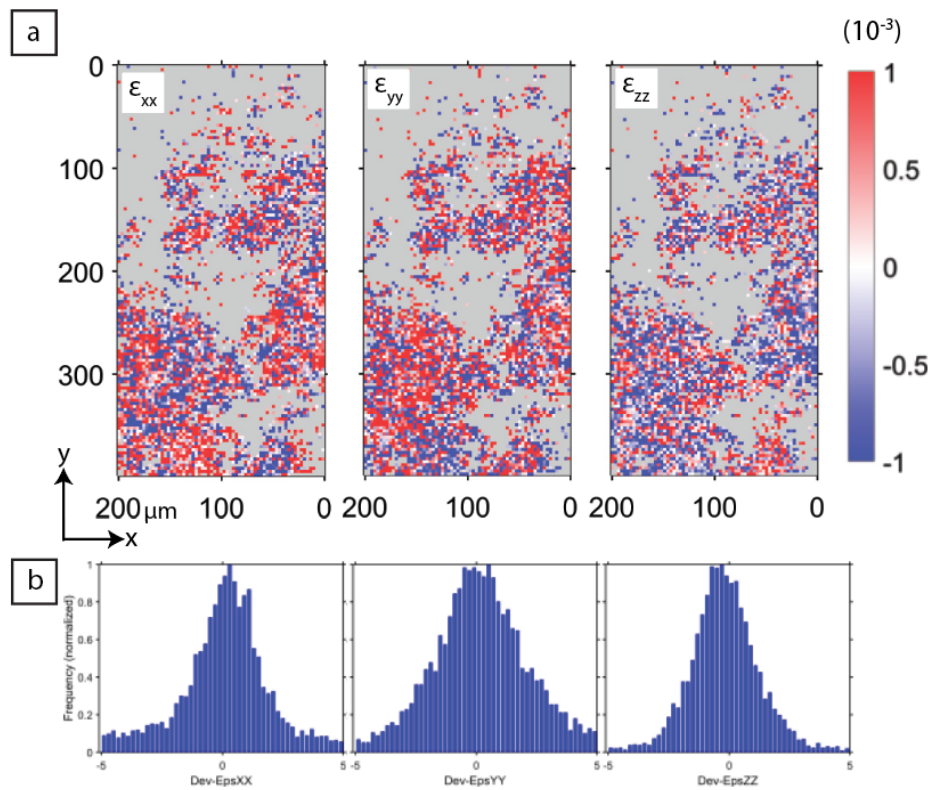
Figure 3.27: *(a) Maps of Ko1_1553C deviatoric strain components ϵ_{xx}, ϵ_{yy}, ϵ_{zz}. Unindexed pixels removed from analysis are gray. Blue represents compression, red is extension. (b) Histograms showing measured strain distribution in (a) for each component.*
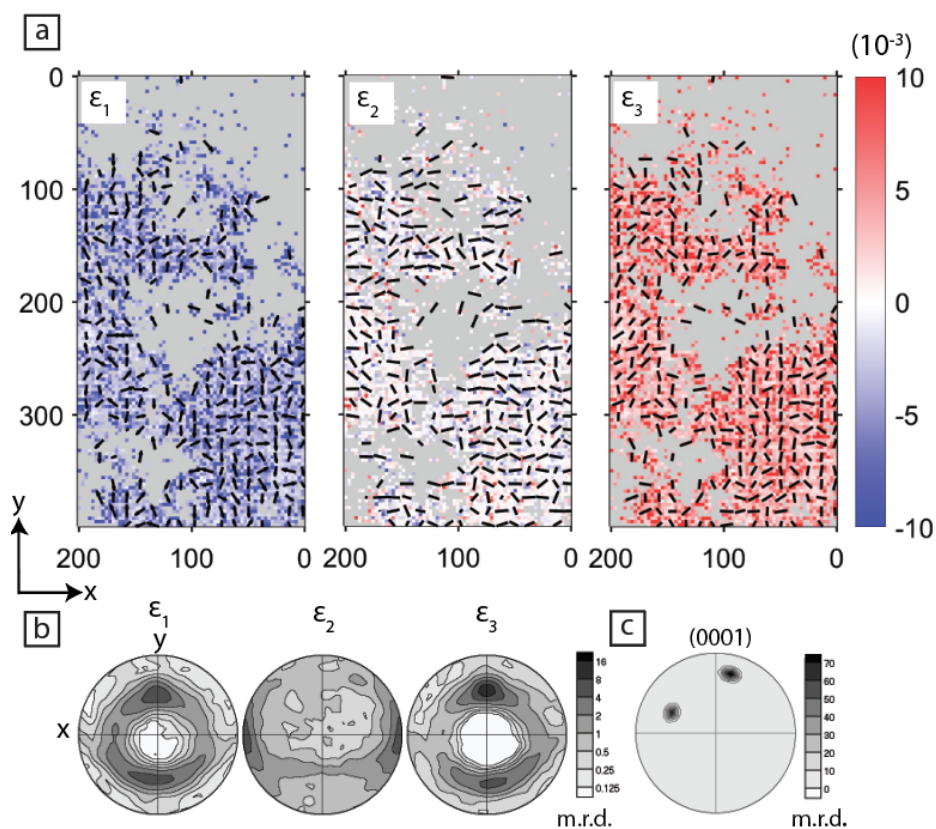
Figure 3.28: *Ko1_1553C (a) principal axes of of compression (ϵ_1), extension (ϵ_3), and the intermediate axis (ϵ_2) plotted as maps in sample coordinate system (x,y,z). Color indicates the magnitude of compression (blue) and extension (red). Unindexed pixels removed from analysis are gray. The orientation of the principal axes are overlain as black lines for every 4th diffraction pattern. The greater the z-component, the shorter the line appears. (b) Principal axes plotted as equal area pole figures in sample coordinate system x,y,z. (c) Crystallographic pole figure showing the orientation of (0001) axes relative to sample coordinates.*

3.10 Results: Experimentally deformed quartzites

The limits of scanning Laue microdiffraction residual strain resolution has also been tested with experimentally deformed quartzites. A first example is Brg127, a greenschist Triassic quartzite from the Bergell Alps that showed significant residual strain (Wenk et al., 2020, p. 1371).

Pre-deformation characterization

A 700 x 450 µm area of Brg1127 was scanned again with µXRD. The sample was mounted such that the foliation was oriented vertically, parallel with the scan y-axis, and thus the long axis of the grains were oriented vertically, as can be seen in the Euler 2 grain map (Fig. 3.29a). The sample showed some plastic deformation as observed by the broad and irregularly shaped diffraction peaks (Fig. 3.29b) indicative of deformation. Diffraction patterns on some areas of the scan did not have 30 or more indexable reflections and were excluded from analysis. This is either due to high amounts of plastic deformation or the peaks may belong to another phase present in the rock such as muscovite. Principal strain pole figures show the axis of compression is oriented horizontally along the x-axis, perpendicular to the foliation plane (Fig. 3.29c) and the principal axis of extension is perpendicular to it (more or less vertical along the y-axis). This agrees with the deformation conditions, as the axis of compression would be expected to be perpendicular to the plane of foliation which is oriented vertically in the scan. The c-axes are also more or less parallel to the principal axis of compression (Fig. 3.29d). The average equivalent strain is approximately 1.5×10^{-3} (Fig. 3.29e) and through application of Hooke's law, the average equivalent stress is approximately 200 MPa (Fig. 3.29f).

Deformation of Bergell quartzite

The Bergell quartzite was then deformed in uniaxial compression using a Paterson apparatus (Paterson, 1969) by Erik Rybacki at GFZ Potsdam. Rybacki determined the quartzite had a porosity of 1.1%. The 1 x 2 cm cylinders were cut from the rock such that the long axis of the cylinder and correspondingly the compression direction was parallel to the foliation plane. The reason for this was to explore if experimental compression perpendicular to the direction of natural residual strain compression switches the alignment of residual strain. A small piece of each cylinder was then cut off such that it was not subjected to deformation and was kept as an "undeformed" sample for comparative analysis. The samples were kept in an oven at 50°C until deformation to dry the samples. Prior to deformation, the cylinders were jacketed in Fe.

Two cylinders of Brg1127 were deformed, and will herein be referred to as H1 and H2. H1 was annealed at 1100°C and 400 MPa confinement pressure for 23 hours and 45 mins. At a temperature of 1100°C , β-quartz is stable. It was then deformed at a constant strain rate of 1×10^{-5}/sec. At 300 MPa differential stress, the load was switched to a constant load and the
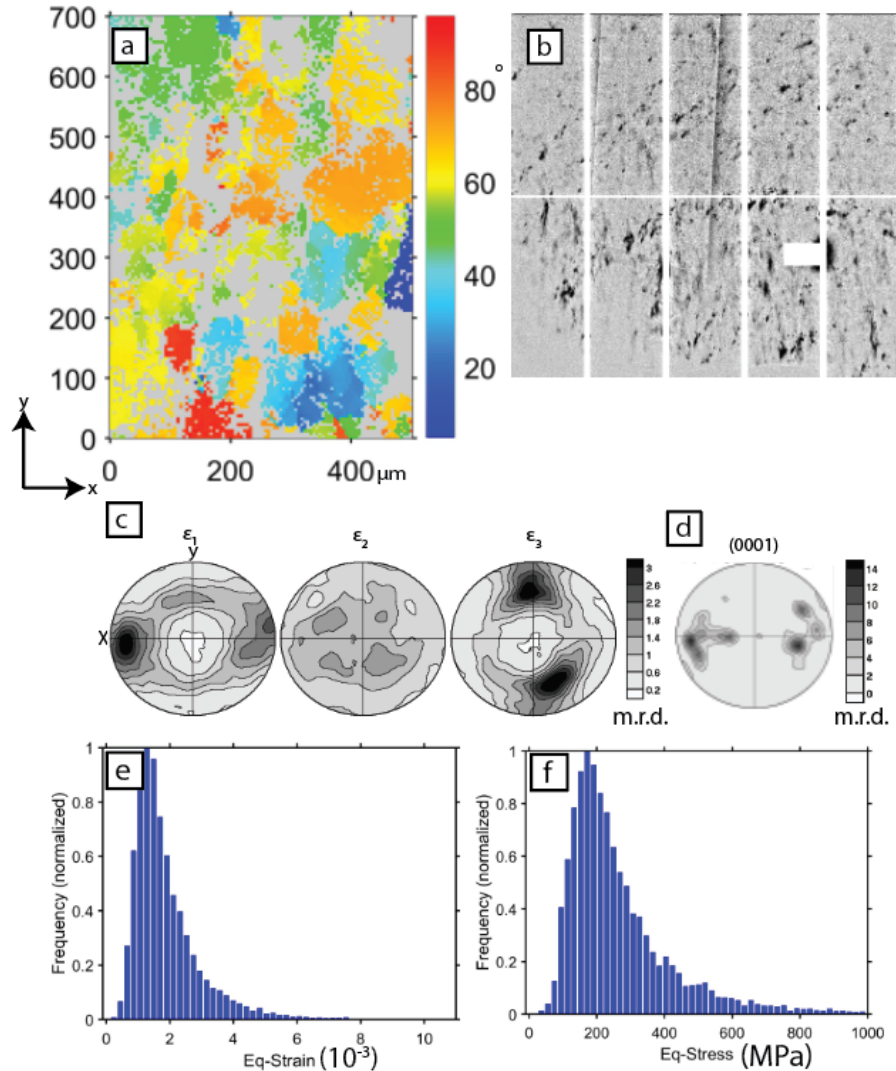
Figure 3.29: *µXRD results of Brg1127 prior to deformation. Scan is oriented such that foliation plane is aligned parallel with the y-direction (vertical) (a) Grain map of scan area, showing Euler 2 angles. (b) Example diffraction pattern. (c) Principal strain pole figures of primary axes of compression (ϵ_1), intermediate (ϵ_2), and extension (ϵ_3), plotted as equal area projections relative to sample coordinate system (x,y,z) reported in multiples of random distribution (m.r.d.). (d) Crystallographic pole figure of (0001) crystallographic poles (c-axes) in scan (a), reported in m.r.d. (e) Equivalent strain of scan area reported in millistrain. (f) Equivalent stress of scan area reported in MPa.*

sample began to creep at 275 MPa stress with an axial strain rate of $\sim$7.2 x10^{-7}/sec (Fig. 3.30a). The decrease in stress shown under constant load is due the increase in diameter of the cylinder with increasing strain with the assumption of constant volume. The cooling system failed overnight and the oven and the piston motor turned off (not shown on Fig. 3.30a). Sample bulging and cracks/grooves in the Fe jacket that seem to line up with the dark striations in the sample can be seen in the cylinder prior to removal of the Fe jacket (Fig. 3.30b). The Fe jacket was dissolved with acid, and dark striations visible in the sample that may be suggestive of partial melting (Fig. 3.30c).

H2 (another sample of Brg1127 deformed) was annealed at 1000°C for 24 hours and then deformed at 400 MPa and 1000°C for 28 hours (Fig. 3.31a). The drop in strain at around 20,000 seconds is due to a drop in confining pressure related to a leak in the intensifier. In this experiment, stress remained constant to about 446 MPa with a slight decrease seen due to increasing cylinder diameter with increasing strain. Total inelastic strain was 2.9%, and the strain rate during creep was calculated to be 2.7x10^{-7}/sec. This sample was also coated in Fe jacket prior to deformation. After deformation, bulging cracks/grooves can be seen through the Fe jacket (Fig. 3.31b), but unlike H1, cannot be correlated in the image captured by Erik Rybacki after the Fe jacket was dissolved (Fig. 3.31c), perhaps the cylinder was rotated between the two images.

The deformed cylinders were then shipped back to Berkeley. I epoxied the cylinders and made thin sections to scan using µXRD. H1 and H2 show significant undulatory extinction and irregular grain boundaries (Figs. 3.32, 3.33).
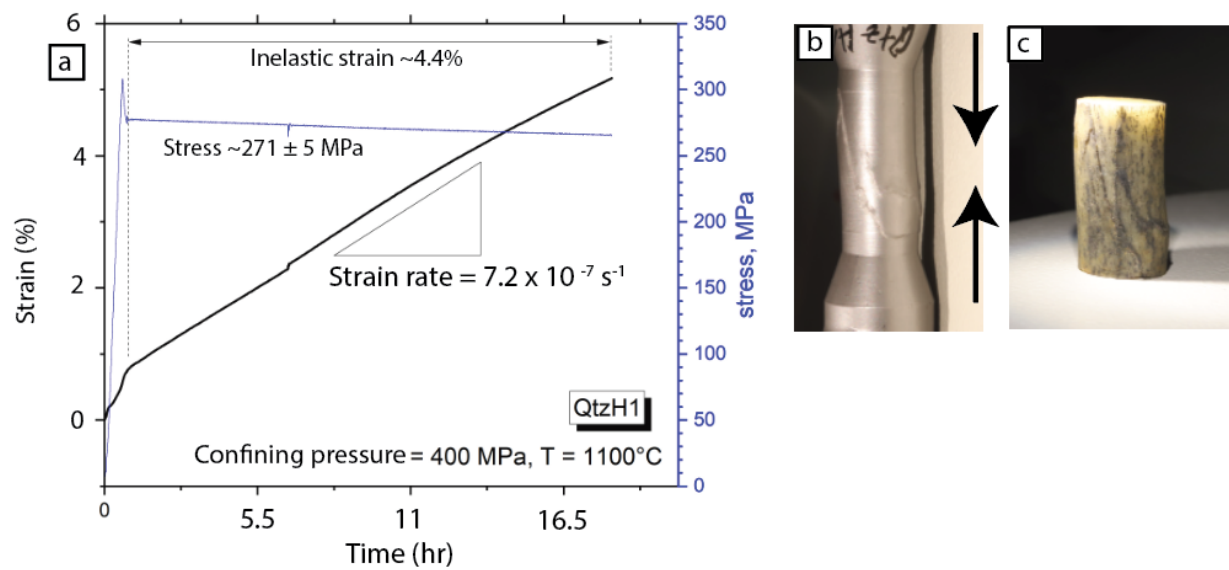
Figure 3.30: *H1 deformation details. (a) Stress (blue) strain (black) curve of deformation. (b) Deformed cylinder in Fe jacket. (c) Deformed cylinder after Fe jacket had been dissolved. Orientation of axis of compression indicated with black arrows. Confining pressure was 400 MPa, temperature = 1100° C. Inelastic strain shows the plastic regime and strain that could not be recovered. (Credit for stress-strain plot and photos: Erik Rybacki)*
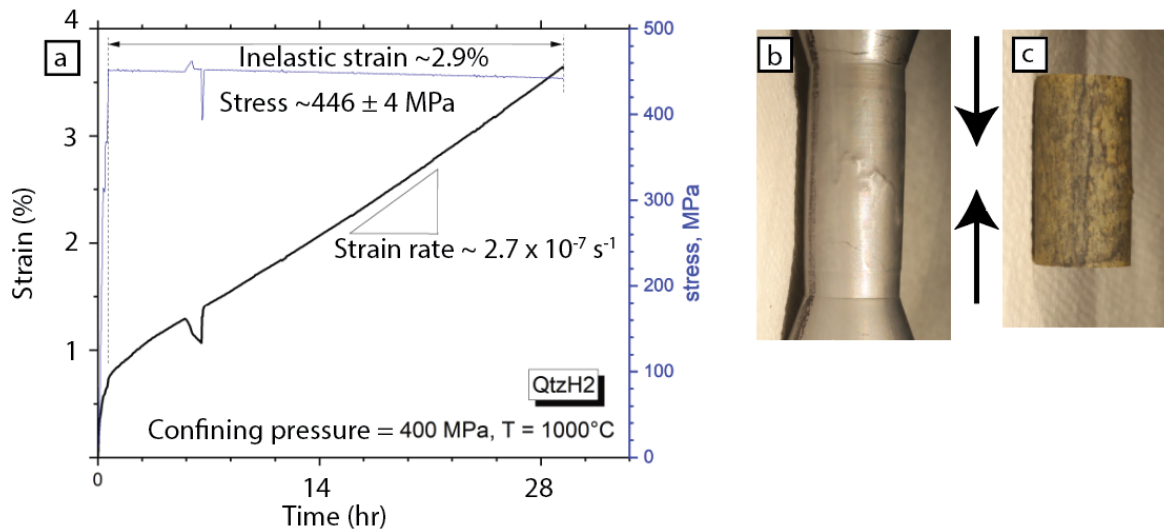
Figure 3.31: *H2 deformation details. (a) Stress (blue) strain (black) curve of deformation. Drop in strain observed around 7 hr due to pressure leak, decreased confining pressure to 378 MPa briefly. (b) Deformed cylinder in Fe jacket. (c) Deformed cylinder after Fe jacket had been dissolved. Orientation of axis of compression indicated with black arrows. (credit for stress-strain plot and photos: Erik Rybacki*
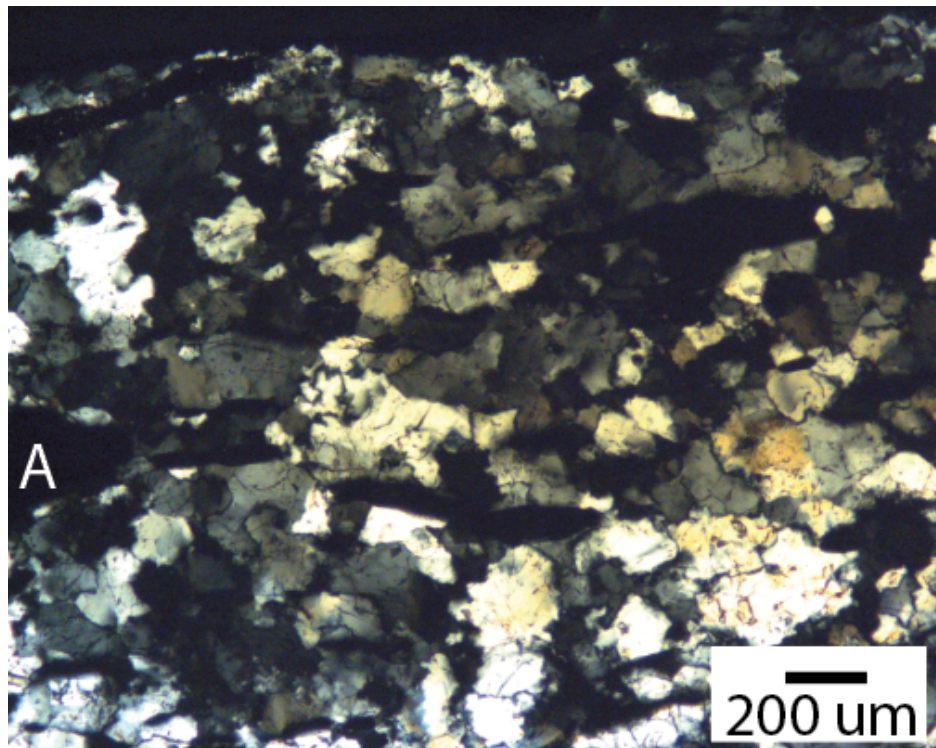
Figure 3.32: *Cross polarized photo micrograph of H1 thin section. The µXRD scan area is located to the right of the arrow tip (A). Yellow discoloration is due to x-ray beam irradiation during scan.*
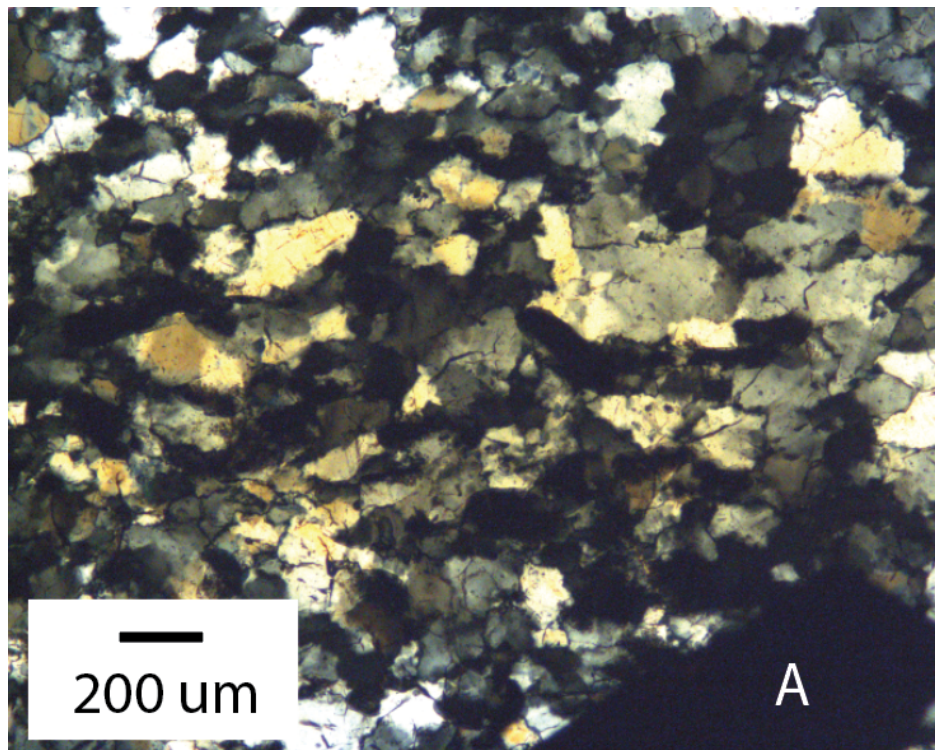
Figure 3.33: *Cross polarized photo micrograph of H2 thin section. The µXRD scan area is located above and to the left of the arrow tip (A). Yellow discoloration is due to x-ray beam irradiation.*

3.11 Deformed Bergell quartzite scanning Laue µXRD results

A 800 x 1000 µm area of H1 thin section was scanned using Laue microdiffraction (µXRD) that covered an area of several randomly oriented grains ranging in diameter between 50-400 µm (Fig. 3.34a). Over half the diffraction images could not be indexed above 20 peaks and thus were excluded from analysis (gray pixels in Fig. 3.34a). This could be due to high levels of plastic deformation as evidenced by the diffuse, broad, and irregularly shaped peaks in the diffraction patterns (Fig. 3.34b). The orientation of the principal strain axes appear to have a strong component in the z-direction which inclines the axis at approximately 45 degrees between the z and y axes. The expected axis of compression would be along the y-axis. Curiously, as seen with the Hong Kong quartzite Ko1_1553C, the axes of compression are coincident with the axes of extension (Fig. 3.34c), and show no correlation with the orientation of the crystallographic (0001) poles (c-axes) (Fig. 3.34d) and show now correlation with the orientation of the c-axes (Fig. 3.34d). Equivalent strain maximum is approximately $2x10^{-3}$ (Fig. 3.34e) and equivalent stress is approximately 300 MPa (Fig. 3.34f) which is similar to the maximum stress the sample endured during deformation of 270 MPa (Fig. 3.30a).

An 800 x 900 µm area of H2 was scanned with µXRD. Over half the diffraction patterns had less than 20 indexable diffraction peaks and thus were excluded from the analysis (gray pixels in Fig. 3.35). This could be due to the high amount of plastic deformation as evidenced by the broad, diffuse diffraction peaks (Fig. 3.35b). Similar to Ko1_1553C and H1, H2 also showed coincident axes of principal compression and extension, with compression inclined 45 degrees toward the z-axis and away from the expected axis of compression (y-axis) (black arrows in Fig. 3.35c). Some variability in principal strain orientations produces a "ring" at 45 degrees. The orientation of the c-axes show no correlation with the orientation of the principal strain (Fig. 3.35d). The average equivalent strain is approximately $2.25x10^{-3}$ (Fig. 3.35e) and a broad distribution of equivalent stress, between 0 and 1000 MPa with an average around 325 MPa (Fig. 3.35f) which is similar to the 446 MPa stress the sample endured during deformation (Fig. 3.31a).

I also measured the residual strain in a portion of the cylinder from which H1 was cut but was not deformed in the Paterson apparatus (H1_undef). I would expect this sample to produce the same results as Brg1127 (Fig. 3.29) because both samples were cut from the same host rock and were not subjected to laboratory deformation.

A 1500 x 500 µm area was scanned with µXRD, with approximately half of the diffraction images with less than 20 indexable diffraction peaks which were excluded from analysis (gray pixels in Fig. 3.36a). H1_undef shows diffraction images that appear to have broad and diffuse diffraction peaks (Fig. 3.36b). H1_undef also shows the same coincident axes of principal compression and extension as observed in the deformed samples, with some variability in orientation that produces a "ring" 45 degrees between the y- and z-axes. This indicates that this principal strain pattern of coincident compression and extension axes
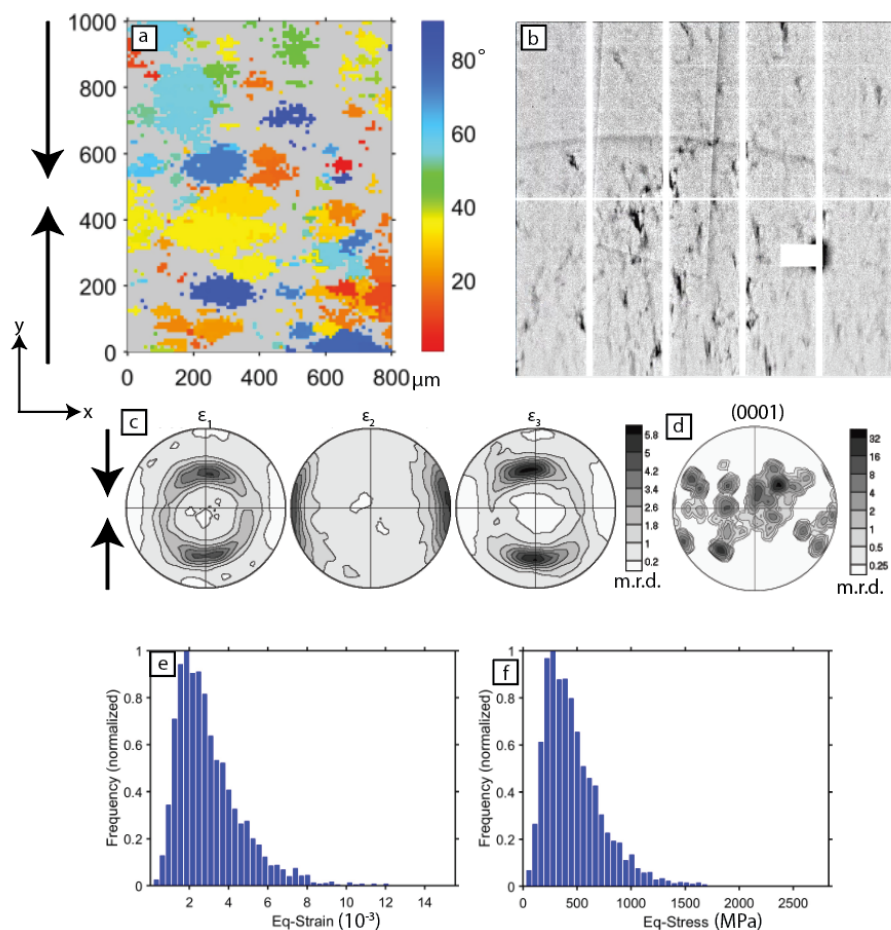
Figure 3.34: *μXRD results of H1 (Bergell quartzite Brg1127 that has been deformed uni-axially at GFZ Potsdam). (a) Grain map of scan area, showing Euler 2 angles. Direction of compression indicated by black arrows. (b) Example diffraction pattern. (c) Principal strain pole figures of primary axes of compression (ϵ_1), intermediate (ϵ_2), and extension (ϵ_3), plotted as equal area projections in sample coordinate system and reported in multiples of random distribution (m.r.d.). (d) Crystallographic pole figure of (0001) poles (c-axes) from scan shown in (a), plotted as equal area projection in sample coordinates. (e) Equivalent strain of scan area reported in millistrain. (f) Equivalent stress of scan area reported in MPa.*
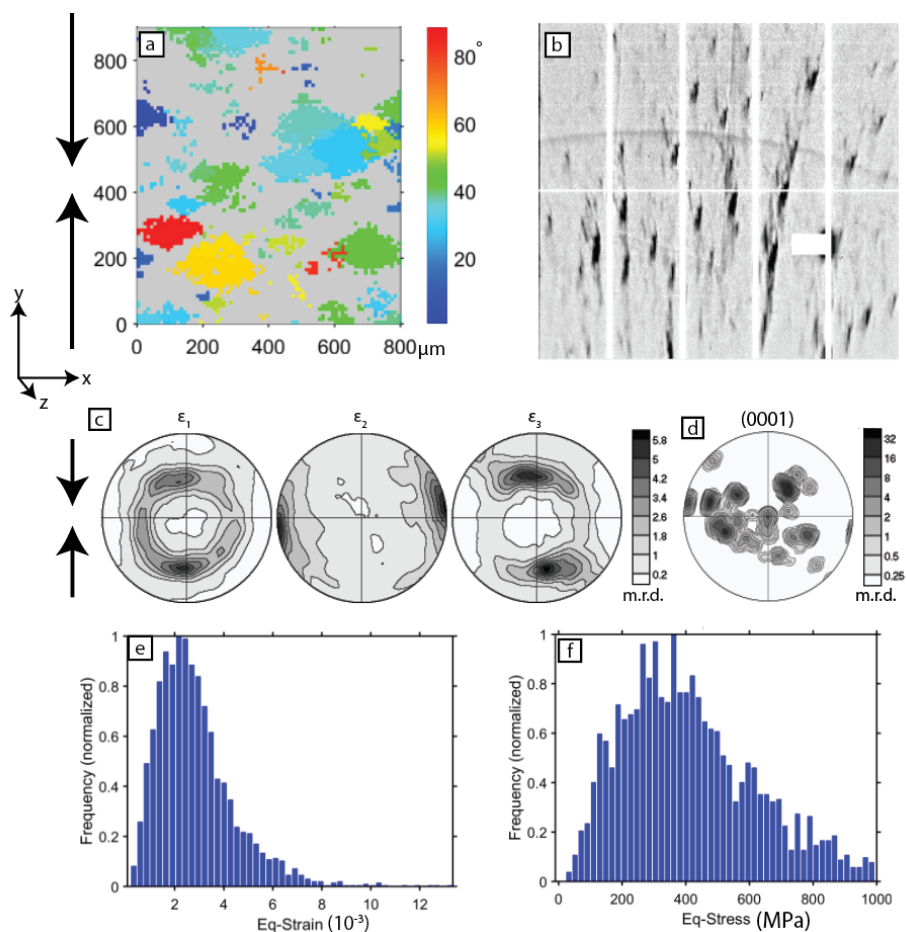
Figure 3.35: *µXRD results of H2 (Bergell quartzite Brg1127 that has been deformed uniaxially at GFZ Potsdam). (a) Grain map of scan area, showing Euler 2 angles. Direction of compression indicated by black arrows. (b) Example diffraction pattern. (c) Principal strain pole figures of primary axes of compression (ϵ_1), intermediate (ϵ_2), and extension (ϵ_3), in sample coordinate system (x,y,z) reported in multiples of random distribution (m.r.d.). (d) Pole figure of (0001) crystallographic axes (c-axes) of scan area in sample coordinates, reported in m.r.d. (e) Equivalent strain of scan area reported in millistrain. (f) Equivalent stress of scan area reported in MPa.*
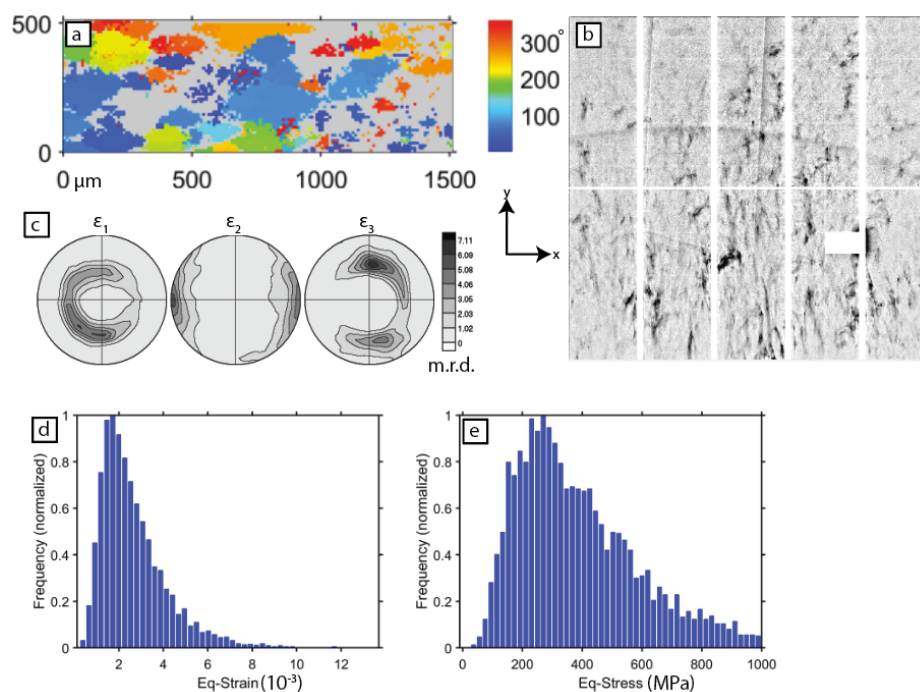
Figure 3.36: *μXRD results of H1_undef (portion of H1 cylinder not deformed). (a) Grain map of scan area, showing Euler 3 angles. (b) Example diffraction pattern. (c) Principal strain pole figures of primary axes of compression (ϵ_1), intermediate (ϵ_2), and extension (ϵ_3), reported in multiples of random distribution (m.r.d.). (d) Equivalent strain of scan area reported in millistrain. (e) Equivalent stress of scan area reported in MPa.*

are not related to deformation. Also curiously is that the equivalent strain and stress for H1_undef are not much different from H1, with average equivalent strain value around $2\text{x}10^{-3}$ (Fig. 3.36d) and equivalent stress around 300 MPa (Fig. 3.36e).

H1_undef and Brg1127 are sampled from the same host rock but show different principal strain patterns. H1_undef and Brg1127 were processed with the same calibrant (YAG) and therefore differences in calibrants could not cause this discrepancy. It is likely that the peaks with high levels of plastic deformation could not be fit accurately which resulted in this principal strain pattern.

3.12   Broad, irregular peak shape and strain calculation

The presence of plastic deformation that causes the peaks to broaden and become more diffuse complicates the peak fitting process in XMAS. XMAS is programmed to fit the peak intensities within a box of a certain size set by the user to a Gaussian, Lorentzian, or Pearson distribution. In my analyses, I fit the peaks to a Gaussian distribution. It is important at

this time to discuss detector resolution. The pixel size of the Dectris Pilatus 1M detector is 172 µm x 172 µm. If the peaks are free of plastic deformation and exhibit a normal Gaussian peak intensity distribution, the peaks can be fit using a Gaussian distribution and elastic shifts can be detected on the subpixel level. However, if the peaks become distorted due to plastic deformation, they no longer fit a Gaussian distribution, and subpixel shifts in intensity can no longer be accurately detected. Overall, this is the limitation of the method.

Considering this, it is worthwhile to demonstrate how the fit of broad diffuse peaks affects the strain measurement. If a peak box size is used that is smaller than the breadth of the intensity, often several peaks are "found" in a single, broad peak (Fig. 3.37a). Additionally if the "multigrain" option is turned on and XMAS is set to find more than one grain, it will consider the subpeaks found with the small peak box size and associate them with subgrains if possible. For example, in Figure 3.37b, two subgrains were found with slightly different orientations, and were indexed as the same *hkl* plane for the two grains. The details on the indexation can be seen in Table 3.2. Comparatively, if a large peak box size is used, it will result in a single peak within the area of intensity (Fig. 3.37c). Note that the peak fitted with the large box size (Fig. 3.37d) is the same as Subgrain 1 (Fig. 3.37b).

Let me elaborate on the details provided from the data in Table 3.2. Subgrain 1 (row 1) has more peaks indexed than subgrain 2 (row 2), and thus would be the subgrain chosen for principal strain analysis. The x and y coordinates of the experimental peak position [x(exp) and y(exp)] are provided, and the *hkl* assigned. The angular deviation (ang_dev) between the experimental peak position and the ideal, unstrained reference peak position, is given in degrees. The deviation in x and y coordinates between the experimental and the reference peak is also provided in pixels, which can be used to determine the reference peak position [xdev(pix) and ydev(pix)]. XMAS fits peaks in order of intensity starting with the brightest peaks first, and thus subgrain 1 has peaks of higher intensity than subgrain 2, and would also be the reason why the peak found for the larger box size is the same as that for subgrain 1.

The advantage of a smaller box size is that many subpeaks may be found within a broad peak. The story of what is actually going on in the big, broad peak can be interpreted in various ways. If the grain is a single, large grain, perhaps bent, with a dislocation structure responsible to produce such a peak shape, then a large peak box size that would find a single peak may be the most appropriate method to use. Alternatively, such a type of grain may be divided into subgrains which are considered individual scattering volumes. If the subvolumes have high plastic deformation, the subpeaks could conjoin into a single large, irregular peak. In my analyses, I used a small peak size box to fit the subpeaks, which generally resulted in a higher number of peaks indexed.

It is worth mentioning that another limitation of this method is that the stress responsible for breaking the original grain into subgrains 1 and 2 is not accounted for in the elastic strain measured using this methodology.

Three neighboring images collected in a scan of H2_A all with the same crystal orientation (Euler angles 1, 2, 3 = 290°, 44°, and 61°) appear to have very similar diffraction patterns (Fig. 3.38 top). Two peak fitting routines were applied to these images, one using a
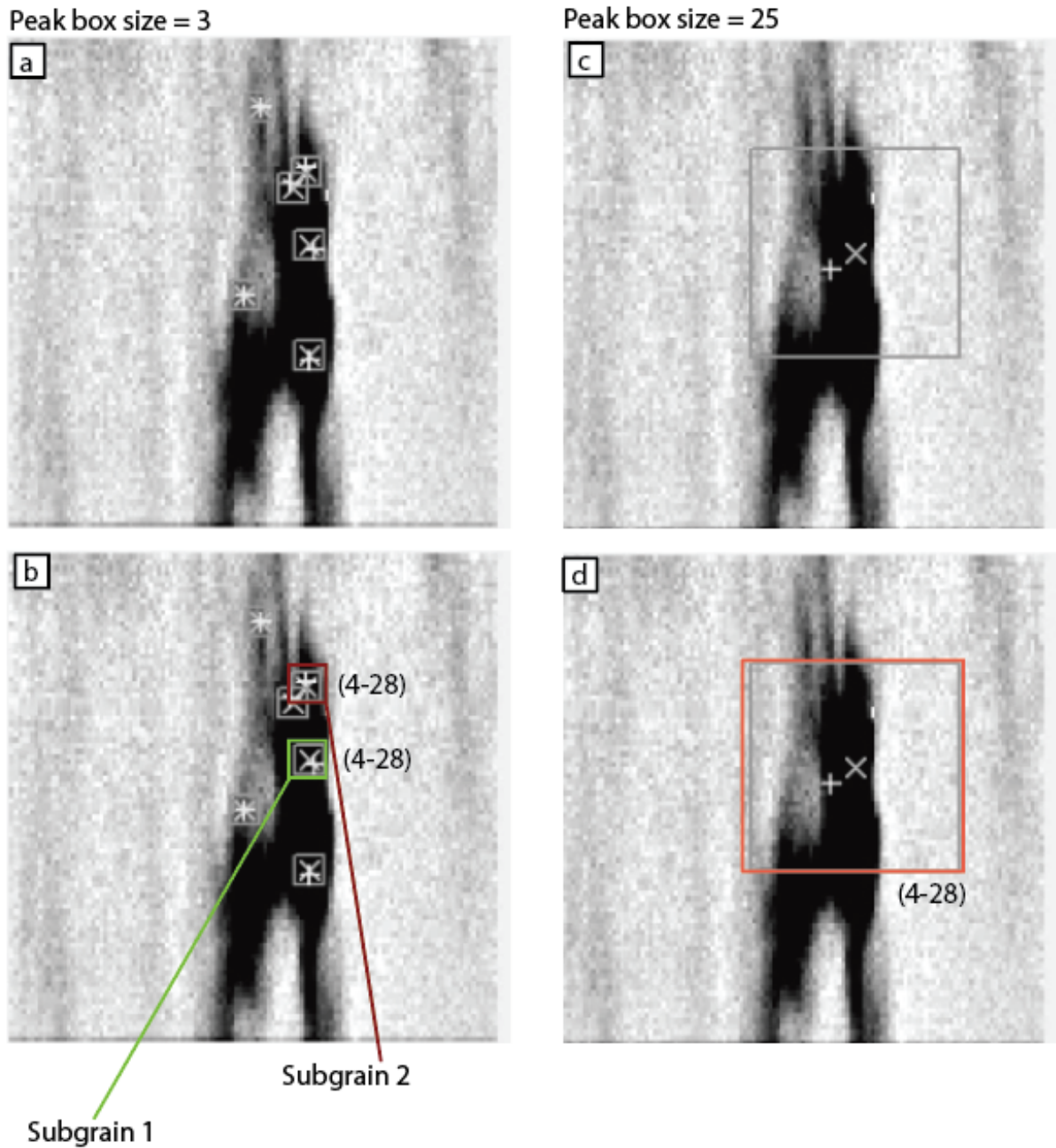
Figure 3.37: *Peak box size affects how peaks are indexed*

Peak box size	Sub-grain No.	No. peaks in-dexed	x(exp)	y(exp)	*hkl*	ang_dev (de-grees)	xdev (pix)	ydev (pix)	inten-sity
3	1	52	734.22	944.56	4-28	0.024	0.312	0.900	10087
3	2	24	733.18	925.90	4-28	0.014	0.224	0.307	3653
25	N/A	33	734.19	944.45	4-28	0.024	-0.078	1.230	10087

Table 3.2: *H2 image#1831 indexation results from Cluster automated analysis for the same image using multigrain indexation, finding 2 grains, and a peak box size of 3 for the same hkl peak (4-28) (rows 1 and 2). X(exp) and Y(exp) are the peak position coordinates, hkl is the Miller Index assigned to the peak, ang_dev is the angular deviation between the experimental peak position and the theoretical peak position, also expressed in pixels in xdev (pix) and ydev(pix), and peak intensity also shown (counts). Row 3 shows indexation results for the same hkl peak using a peak box size of 25 for comparison.*

peak box size of 3, the other a peak box size of 25 and the number of peaks indexed for each image is listed below the image. Indexation results for peak (4-28) using a box size of 25 is provided in row 3 of Table 3.2. The orientation of the principal strain axes were calculated for each diffraction image using both peak box sizes. Despite peak positions appearing to be very similar between the three images, principal strain orientations appear to significantly differ between the three images when fit with the same box size. Additionally, the same image produced different principal strain orientations when indexed with different box sizes (Fig. 3.38 bottom).

The same analysis was performed on three neighboring images from Ko1_1553C scan all with the same crystal orientation (Euler angles 1, 2, 3 = 245°, 52°, and 131°) (Fig. 3.39). Two peak fitting routines with box sizes of 5 (top row) and 50 (bottom row)were used. Principal strain orientations for neighboring images show very different principal strain patterns.

The question that remains is what exactly is causing this curious principal strain matter. I've demonstrated that there are different ways to peak fit and index an image (Fig. 3.37), and that the peak box size used can affect the strain measurement (Fig. 3.38). Because a similar principal strain pattern for the entire scan, which forms a ring, inclined at 45 degrees, around the z-axis with maxima along the y-axis, is observed across four different rock samples (Figs. 3.28, 3.34, 3.35, 3.36), it is unlikely that the four rock samples possess the exact same microstructure to produce the same principal strain pattern. Rather, it is likely related to the inability to detect elastic strain shifts in peak position when the peak possesses an irregular intensity distribution, such as peaks evidencing plastic deformation, as mentioned previously. However the exact source of why this causes a ring of principal

strains around the z-axis with maxima along the y-axis remains a question.
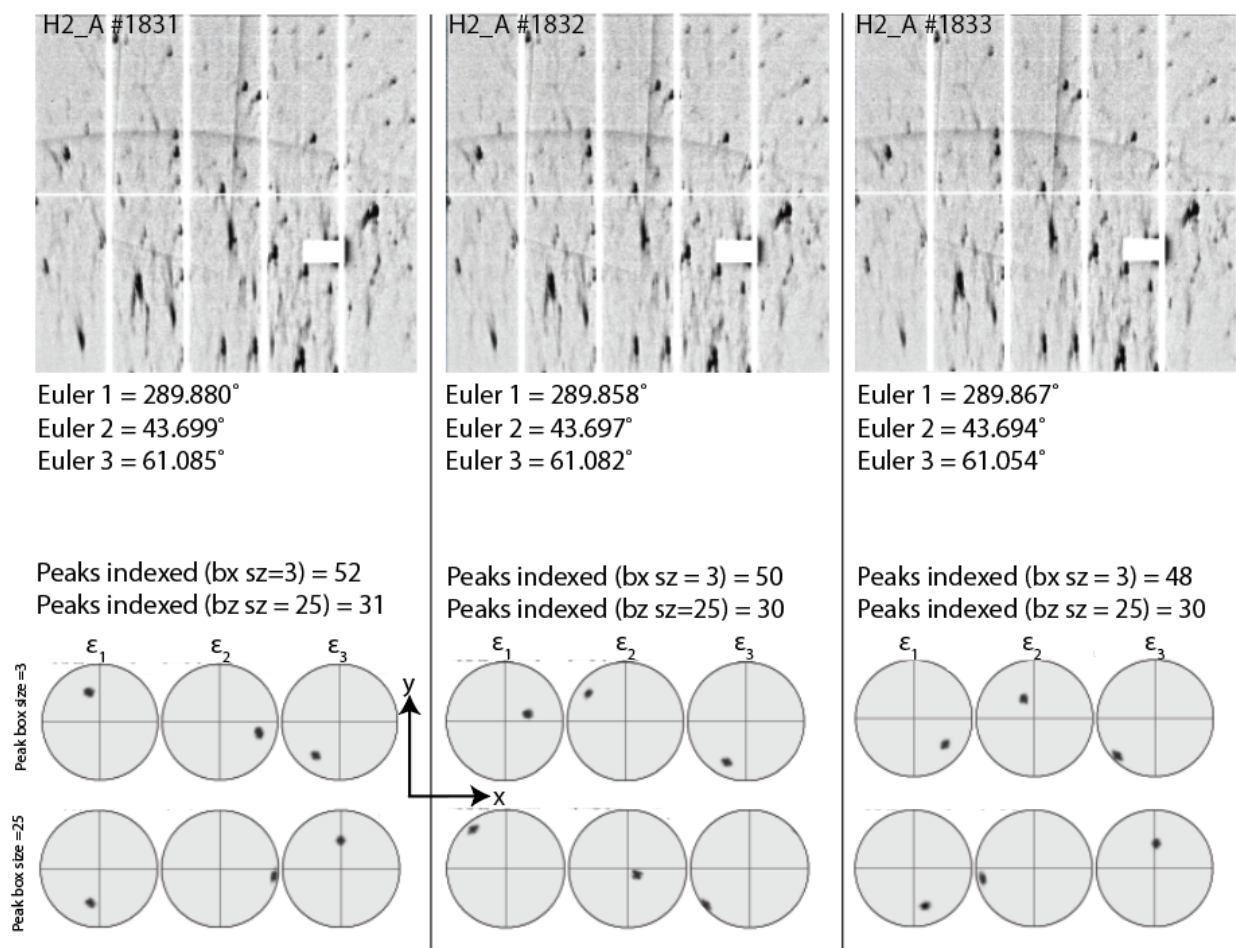
Figure 3.38: *H2_A image series showing three neighboring diffraction images with the same orientation (top row) from a scan. H2 was compressed parallel to the Y axis. The number of peaks indexed on the image using two different box sizes are listed below the images. The bottom half of the image shows principal strain pole figures showing the orientation of the axes of maximum compression (ϵ_1), intermediate (ϵ_2), and extension(ϵ_3) for a peak fitting routine using a box size of 3 (top row) and a box size of 25 (bottom row).*
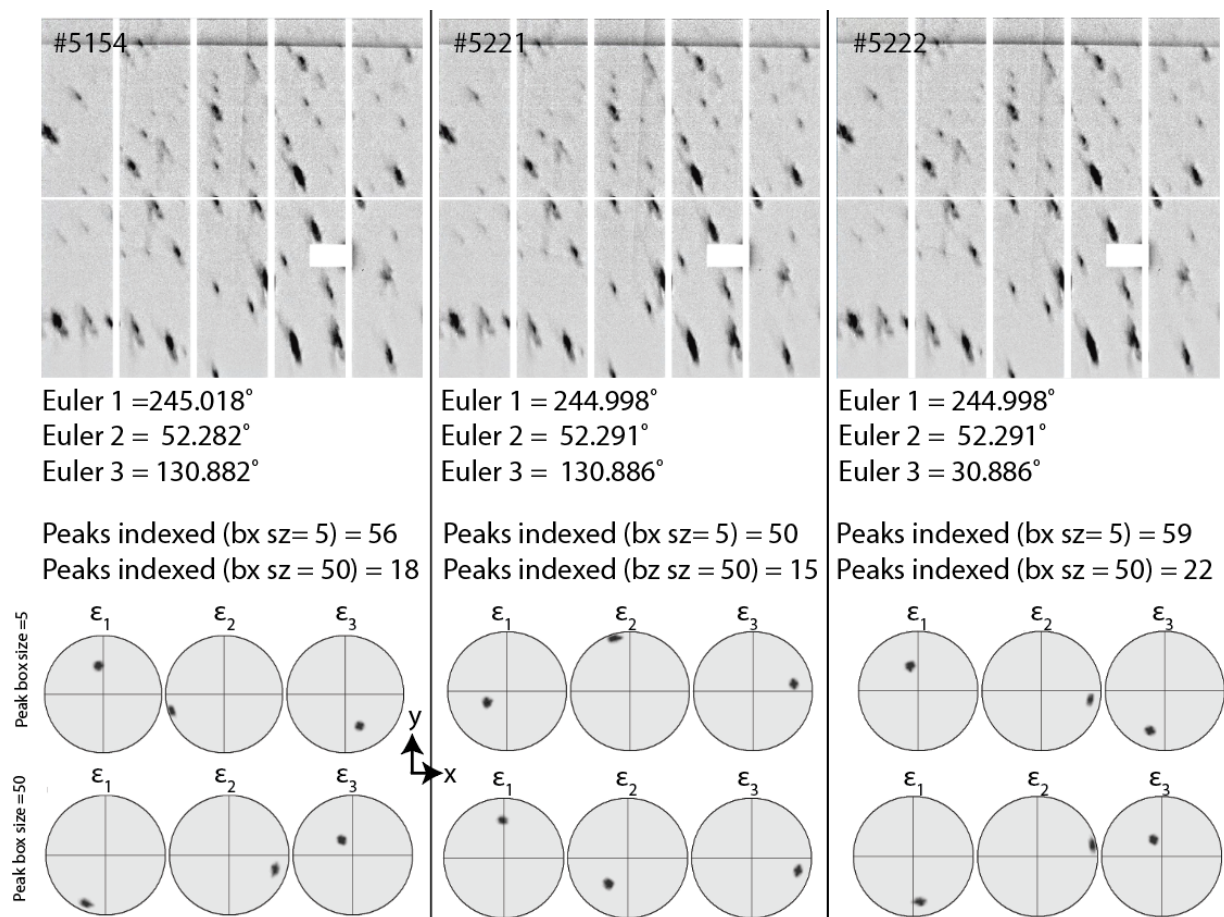
Figure 3.39: *Ko1_1553C image series showing three neighboring diffraction images with the same orientation (top row) from a scan. The number of peaks indexed on the image using two different box sizes are listed below the images. The bottom half of the image shows principal strain pole figures showing the orientation of the axes of maximum compression (ϵ_1), intermediate (ϵ_2), and extension(ϵ_3) for a peak fitting routine using a box size of 5 (top row) and a box size of 50 (bottom row).*

3.13 Results: Rolled titanium

I also tested the ability of scanning µXRD to determine the paleostress orientation on a non-geologic material, rolled titanium. Rolled Ti was chosen because its deformation history is known; the orientation of stress used to produce the material can be verified by looking at the alignment of the long axes of the grains.

A 1.2 mm thick sheet of ASTM B 295 Grade 4 commercially pure rolled Ti was cut to 1.8 x 1.4 cm and used for analysis. Grain sizes ranged from 5 - 30 µm with their long axis parallel to the rolling direction (i.e. the direction of motion of the rollers) and perpendicular to the normal direction (i.e. the direction perpendicular to the rollers) (Fig. 3.40). Two 1.5 x 2 mm areas of the rolled surface were collected, Ti_6 and Ti_6_90d, the second being the same area as the first rotated 90°. The reason for the 90° rotated scan is to ensure the rotation of the principal strain directions is also observed. A step size of 50µm was chosen to get a sample the strain over many grains. Polysilicon was the calibrant of choice at the time of the experiment and was used in this analysis. The diffraction images show small, uniform peaks lacking in heavy amounts of plastic deformation (Fig. 3.41).
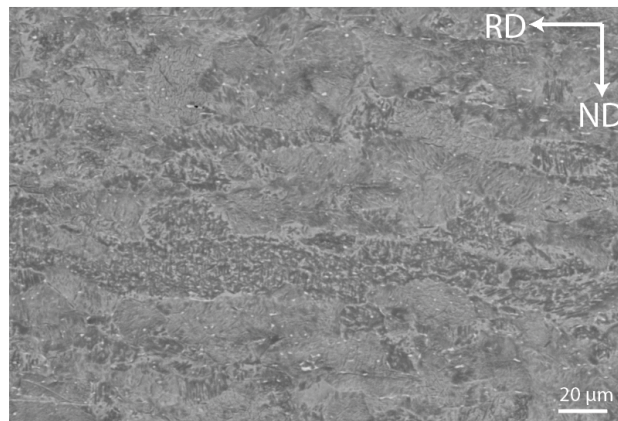
Figure 3.40: *Scanning electron microscope backscatter electron image of the cross section of rolled titanium. RD is the rolling direction, ND is the normal direction.*

The magnitude of the deviatoric strain tensor components suggest that compression (negative) occurred along the axis normal to the sample surface (ND), which would be the same direction the rolling force was applied to the sample, and extension (positive) primarily occurred along the rolling direction (RD) in both the non-rotated and rotated scans. Similarly, the orientation of the principal strain axes show that the axes of maximum compression are parallel with the normal direction, and maximum extension are parallel with the rolling direction.

The variability of deviatoric strain magnitudes, principal strain orientations (Figs. 3.42, 3.43, 3.44) and distribution of equivalent strain and stress (Fig. 3.45) suggests strain hetero-geneity across the scan area, as well as between the two scan areas. This could be related to
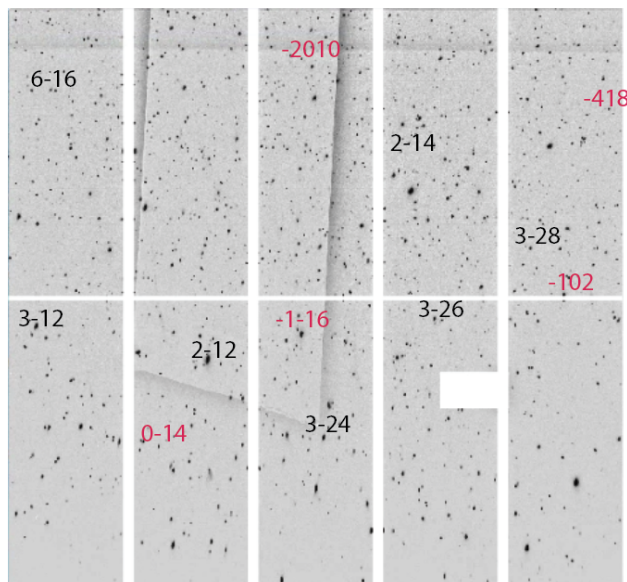
Figure 3.41: *Example diffraction pattern from scan Ti_6. Some peaks from two different grains (black, red) have been labeled with their Miller indices.*

grain statistics (the number of grains sampled during the scan), and heterogeneity of stress between the grains sampled which can be affected by the orientation of the crystal relative to the stress, grain boundary geometries, and grain-grain interactions. Additionally, only a small portion of the grain was measured during the experiment, and while a large step size of 50μm was used to try to sample several grains, still perhaps not a sufficient number of grains were probed to generate the same distribution of strain and stress between the two scans.

The equivalent strain for both scans was calculated to be ∼3.25 millistrain (Fig 3.45a). The equivalent stress calculated for Ti_6 is ∼575 MPa (Fig. 3.45a), and that for Ti_6_90d shows a broader distribution with two maxima at ∼450 MPa and ∼575 MPa (Fig. 3.45b). Strain heterogeneity in the sample and slight variations in scan area likely has led to the difference between these two scans. The magnitude of the equivalent stress calculations, between 400 and 600 MPa, is similar in magnitude of residual stress measured in Ti-Al-V alloy [Fig. 10 of Wang et al., 2020] and low-Fe-Ti alloys [Fig. 7.25 of Schajer, 2013].

The deformation texture measured in the Ti sheet from both scans is plotted as pole figures, displaying the (0001) pole relative to sample coordinates (Fig. 3.46a, b) and compared with literature deformation texture of rolled Ti (Fig. 3.46c).

The (0001) pole figures demonstrate a deformation texture that is consistent with that published by (Blicharski et al., 1979) (Fig. 3.46). The discrepancies between my values and the literature could be due to the fact the Ti measured in this experiment is a sampling of the surface rather than the bulk material. Additionally, inhomogeneous strain distribution throughout the sample, and between scan areas, could cause variability between scans. The
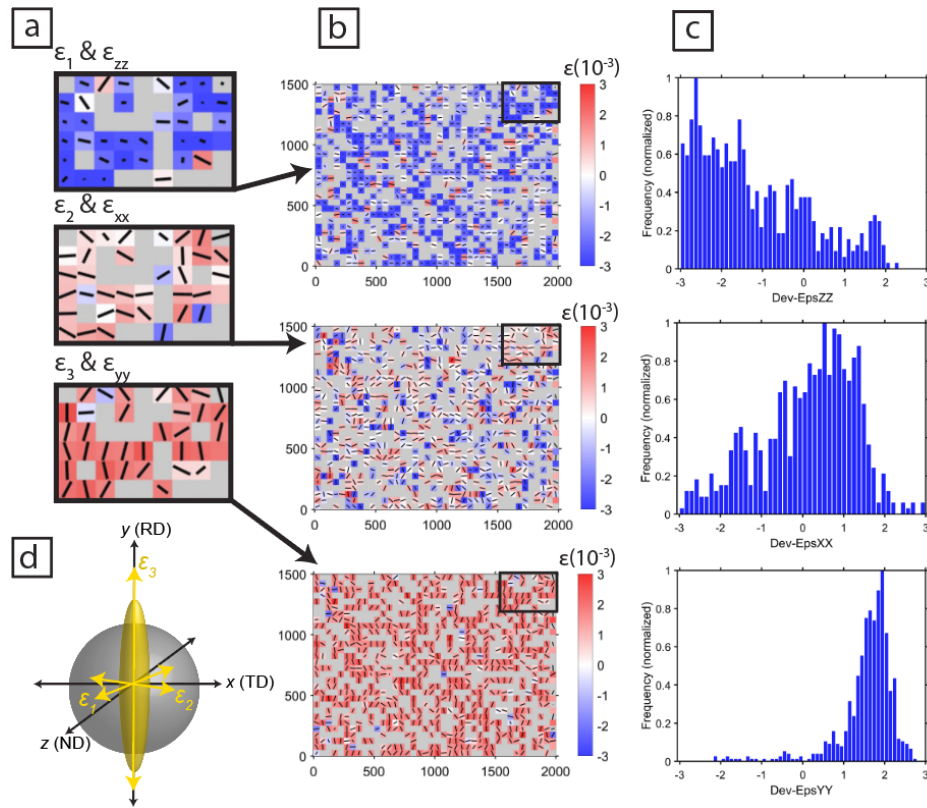
Figure 3.42: (a) Close up subsections of maps in (b) showing the magnitude of the ϵ_{xx}, ϵ_{yy}, and ϵ_{zz} components of the deviatoric residual strain tensor in sample coordinates (RD, TD, ND) for Ti_6 scan of dimensions 2000 x 1500 mm with a step size of 50 mm. Projections of principal strain axes ϵ_1, ϵ_2, and ϵ_3 are overlain onto each pixel as a black line. Each pixel represents one step in the scan and shows the data associated with the diffraction image collected at that step. The color of each pixel indicates the magnitude of the deviatoric strain at that position (10^{-3}). Red color (positive values) is extension, blue color (negative values) is compression. Gray pixels are diffraction images that have fewer than ten indexed reflections and were thus removed from analysis. (c) Normalized frequency distributions of residual strain values from plots in (b). (d) Principal strain ellipsoid showing overall orientation of maximum axis of compression ϵ_1 and extension ϵ_3 calculated from this scan.

Figure 3.43: *Scan area in Fig. 3.42 that has been 90° rotated. (a) Close up subsections of maps in (b) showing the magnitude of the ϵ_{xx}, ϵ_{yy}, and ϵ_{zz} components of the deviatoric residual strain tensor in sample coordinates (RD, TD, ND) for Ti_6_90d scan. Projections of principal strain axes ϵ_1, ϵ_2, and ϵ_3 are overlain onto each pixel as a black line. Each pixel represents one step in the scan and shows the data associated with the diffraction image collected at that step. The color of each pixel indicates the magnitude of the deviatoric strain at that position (10^{-3}). Red color (positive values) is extension, blue color (negative values) is compression. Gray pixels are diffraction images that have fewer than ten indexed reflections and were thus removed from analysis. (c) Normalized frequency distributions of residual strain values from plots in (b). (d) Principal strain ellipsoid showing overall orientation of maximum axis of compression ϵ_1 and extension ϵ_3 calculated from this scan.*

Figure 3.44: *Principal strain pole figures for Ti and Ti 90deg, in sample coordinates. Equal area projections. Contours are in multiples of random distribution (m.r.d.)*
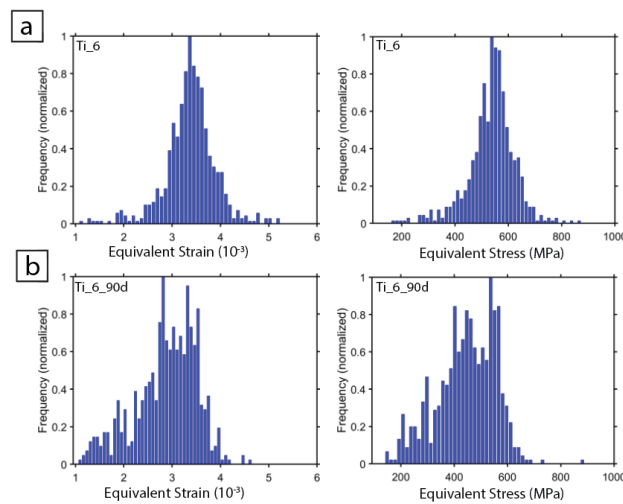
Figure 3.45: *Rolled Ti equivalent strain (a) and stress (b) distributions for Ti_6 and Ti_6_90d*
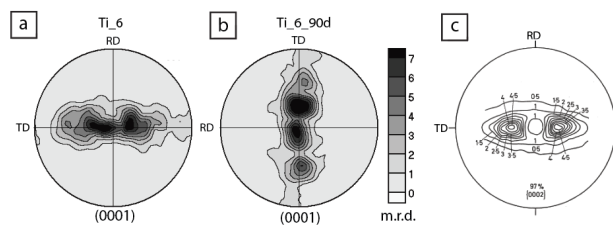
Figure 3.46: *Deformation texture of crystal (0001) poles for scan (a) Ti_6, and (b) Ti_6_90d. (c) is deformation texture of (0002) poles for rolled Ti reduced to 3% original thickness (Blicharski et al., 1979).*

deformation textures produced could be explained by basal and pyramidal slip and twinning (Zaefferer, 2003).

In this experiment, synchrotron x-ray Laue microdiffraction has been used to measure the residual strain in a sample with a known stress history. The orientation of the principal strain ellipsoid measured from the sample of rolled Ti is in agreement with the deformation conditions showing maximum compression aligned with the normal direction and maximum extension along the rolling direction. Additionally, the deformation texture of the (0001) axes is in agreement with that produced for rolled Ti reduced to 3% of its original thickness.

3.14 Further discussion and conclusions

For two samples, the vein quartzite from Hong Kong (HSM_1159A) and rolled Ti (Ti_6 and Ti_6_90d), the residual strain measured by scanning μXRD resulted in reasonable principal strain orientations inferred from the morphology and alignment of the grains (HSM), and the known sample deformation history (rolled Ti). The properties of these samples vary, in terms of material, crystal structure, and x-ray transparency, however they yielded reasonable results that support scanning μXRD as a method to measure the paleostress orientation in deformed crystalline materials. However, the quartzites from the Hong Kong explosion structure (Ko1_1553C), experimental deformation (H1 and H2), and a piece of Bergell quartzite (H1_undef), the principal strain orientations all show coincident axes of compression and extension, with variation that spread the maxima around a "ring" at 45 degrees inclined to the z-axis.

The observable trend amongst the scans that produce principal strain patterns in agreement with their presumed deformation conditions are that the diffraction patterns have sharp, uniform peaks lacking in plastic deformation. This is likely related to the ability to detect subpixel shifts in peak position related to elastic strain because the intensity distribution of the peak is still regular and Gaussian. Comparatively, the observable trend amongst scans that produce coincident axes of compression and extension is that their peaks are broad, diffuse, and irregularly shaped, demonstrating the presence of plastic deformation (Barabash et al., 2003). This strain artifact could be related to the detector resolution and the inability to detect shifts in elastic strain with non-Gaussian peak intensity distributions on the subpixel level. However the exact origin of this curious principal strain pattern remains a point of investigation.

Chapter 4

In-situ crack healing of a calcite single crystal

4.1   Introduction

The deformation of calcite ($CaCO_3$) and calcitic rocks such as marble have been studied since the late 1920s (e.g. Sander et al., 1929; Griggs, 1938; Knopf, 1946; Turner et al., 1954; Renner et al., 2002). The mineral has been a popular topic of study due to its abundance in crustal rocks, and its ability to deform without confining pressure. Today, calcite remains relevant due to its presence in hydrocarbon basins and geothermal reservoirs, as well as serving as a primary component of concrete and cementitious materials; fluid transport in calcite-containing rocks of hydrocarbon basins and geothermal reservoirs such as limestones and calcite-cemented sandstones are affected by the competing processes of crack growth and healing which modify the permeability of the units (McNamara et al. 2016). Subcritical crack growth (SCG), the process by which cracks propagate at stress values less than the critical value (Atkinson, 1984), is argued to be the primary mechanism of calcitic sediment compaction in hydrocarbon reservoirs (e.g. Royne et al., 2011; McNamara et al., 2016), and understanding crack propagation and closure is critical to controlling mineralization in such environments. Yet questions remain about these processes. SCG is influenced by stress corrosion, ion exchange, dissolution, diffusion, microplasticity, and residual stress in the crystal (Atkinson, 1984).

Compared to metallic materials, little is known about crack propagation and healing in brittle materials, such as calcite. Crack growth can be considered the competition between intrinsic microstructural damage ahead of the tip, which influence stress intensity and the driving forces of crack propagation, and extrinsic shielding mechanisms that occur behind the tip and reduce the crack tip driving force (Ritchie, 1988). In metallic materials, intrinsic mechanisms that occur ahead of the crack tip and promote crack growth include dislocation pileups, decohesion of the interface, brittle intergranular cracking, and microvoid coalescence. In the wake of the crack, extrinsic shielding mechanisms form a zone of plasticity that can

involve zone shielding mechanisms such as crack wake plasticity, crack field void formation, residual stress fields, crack tip dislocation shielding, as well as contact shielding mechanisms such as wedging or bridging between the crack surfaces (Ritchie, 1999). However, less is known about the influences of microplasticity on crack propagation and healing in brittle materials.

Several methods have been used to study the strain fields surrounding a crack, including strain gauges (Irwin, 1957), neutron diffraction (Hutchings et al., 1990) and synchrotron x-ray diffraction and microscopy (Steuwer & Daniels, 2011; Withers, 2015). When combined with a micro-focused x-ray beam, synchrotron x-ray microdiffraction produces high–resolution maps of the elastic strain in a material. Depending on the energy of the beam, the composition and thickness of the sample, the entire thickness of the bulk can be probed. This technique is particularly useful for studying the strain fields around cracks and has been used to study alloys (Croft et al., 2005; Steuwer et al., 2005).

In this study, a double-torsion device (Outwater & Gerry, 1969; Shyam & Lara-Curzio, 2006) was used to propagate a Mode I crack in a slice of single crystal calcite and synchrotron X-ray Laue microdiffraction at the Advanced Light Source (ALS) beamline 12.3.2 was used to measure the deviatoric elastic strain surrounding a crack tip while the sample was under load, and a series of scans collected upon unloading to determine the strain evolution during crack closure. Double-torsion is a common technique used to study fracture mechanics of brittle materials because the stress-intensity factor is a function of the applied load, specimen dimensions and Poisson's ratio, and is independent of crack length and thus allows for the controlled propagation of cracks in brittle material (Williams & Evans, 1973).

4.2   Methods

A slice (30 mm x 10 mm x 1 mm) was cut from an optical-grade natural single crystal of calcite (cutting performed by Crystran, LTD., UK). The orientation of the slice relative to the three cleavage planes is shown in Figure 4.1a. The slice was pre-notched to control the propagation direction. It was then loaded into a customized double-torsion device to propagate the crack. The slice was oriented such that the crack would propagate down the long axis of the slice, parallel to the {10-14} cleavage (Fig. 4.1b). The custom-designed double torsion device used in this experiment uses a small ball-bearing placed in the tip of a cup-tip set screw that is placed directly above the notch in the calcite slice to propagate a tensile crack via 3-point bending loading. The sample is considered as two, independent bars on either side of the crack, each experiencing torsion, hence "double" torsion.

The double-torsion device was modified such that it held the slice perpendicular to the x-ray beam (Fig. 4.2a), which requires four more ball bears on the top of the slice to hold it in place (Fig. 4.1). The top piece of the device was removed to reduce shadow from the device on the detector. Despite this removal, a shadow from the device still remained which prevented diffraction peaks from reaching the right-most panels of the detector (Fig. 4.2b). The center coordinate of the diffraction pattern, in diffraction pattern coordinate system x,
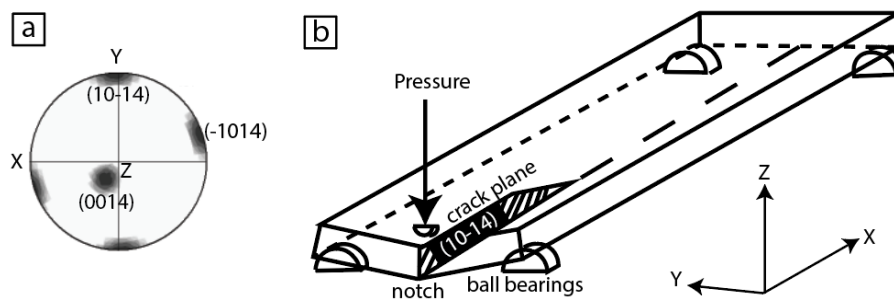
Figure 4.1: *(a) Pole figure showing orientation of calcite cleavage planes relative to sample coordinates X,Y,Z. The (10-14) plane is parallel with the X-axis. Equal area projection. (b) Schematic of the double-torsion device. Pressure exerted by a pin with a ball-bearing in the tip is exerted on the pre-notched slice, which propagates a crack down the (10-14) plane splitting the specimen into two "bars", which are considered as two, independent bars experiencing torsion, hence the name "double-torsion" device. In the device used in this experiment, four more ball bearings are placed on the top side of the slice to hold the sample in the device. Sample coordinates X,Y,Z shown.*

y, is marked with a red dot. This central coordinate marks the shortest distance between the detector and the origin of diffraction in the sample, and is determined during calibration. It is discussed in detail later.

The experimental setup used to measure residual strain in a standard thin section described in Chapter 3 uses reflection geometry with a 45° angle of incidence between the sample and the detector to increase the number of reflections received on the detector. Due to the goal of probing the strain around a planar feature (a fracture plane) in the calcite slice, the 45° angle of incidence produces an asymmetrical sampling of the planar feature (Fig. 4.3a) and produces an asymmetrical projection/reconstruction of the planar feature in the data. For this reason, a 90° angle of incidence was used in this experiment to sample the planar feature equally over the scan dimensions (Fig. 4.3b. Note that in Fig. 4.3, the origin of scattering is shown as the back surface of the slice for ease of demonstration, however in reality the origin of scattering can vary along the thickness of the slice, as discussed later.

The beamline geometry was calibrated with a YAG crystal mounted on a glass slice oriented at 45° to the incident beam. While the calcite slice is oriented 90° to the incident beam, the purpose of calibration is to refine the position of the detector relative to the scattering origin located at the focal point of the beam. The surface of the YAG crystal was placed at the focal point of the beam using a laser proxy and beamline camera to align. A small YAG scan was collected over a 100 µm x 100 µm area in 10 µm steps, and used to refine the 5 independent parameters defining the sample-detector geometry as explained in Chapter 3.

Prior to deformation, 1.5 mm x 2 mm control scan was collected and was positioned such
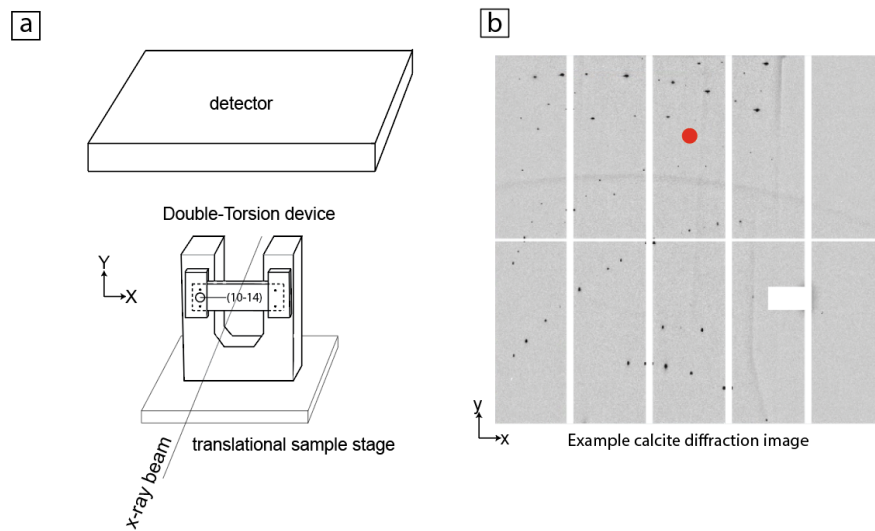
Figure 4.2: (a) Schematic of custom double-torsion device used to hold calcite slice perpendicular to the x-ray beam. The device is located beneath detector. Sample coordinate system X, Y, Z. Pin (parallel to the laboratory coordinate system Z-axis) propagates crack down the (10-14) plane. (b) Example diffraction image of calcite. Center coordinate of diffraction pattern marked with a red dot. Shadow from the double-torsion device is seen on the right-most panels. Diffraction pattern coordinate system x, y.
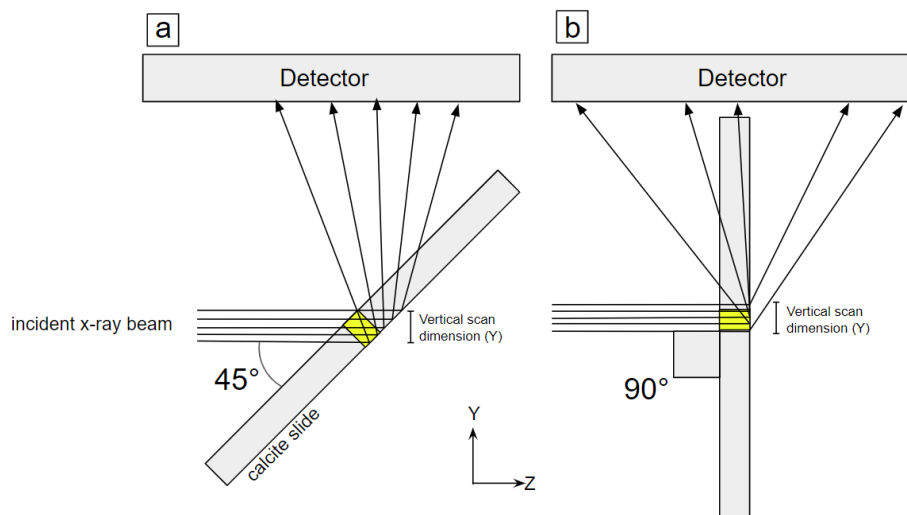
Figure 4.3: Schematic of the difference in sampling of a planar feature (yellow), such as the fracture plane in the calcite slice, in a sample oriented at (a) 45° to the incident beam, and (b) 90° degrees to the incident beam.
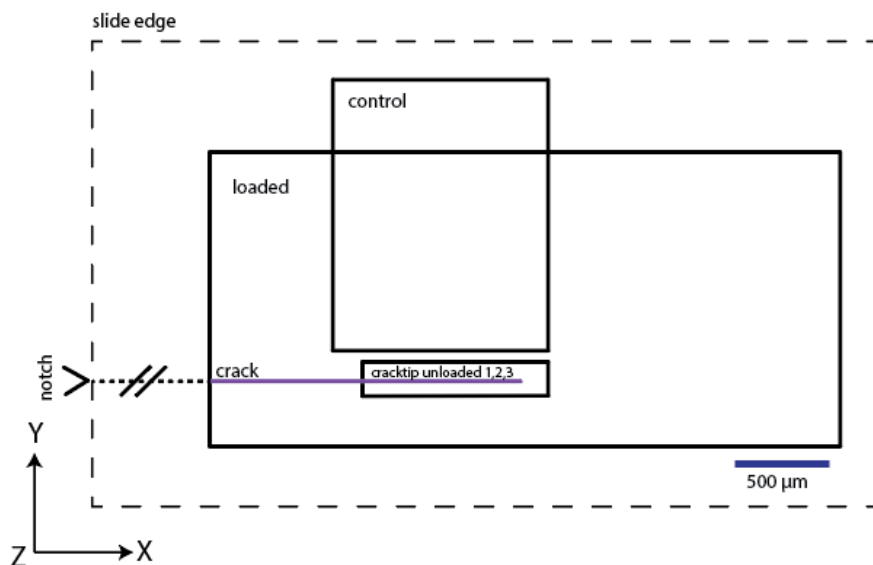
Figure 4.4: *Spatial relationships of scans collected during experiment. Note the area between the slice edge to the scan areas is not to scale. Sample coordinates X,Y,Z.*

that it would cover the area where the crack would propagate through, but it ended up being slightly above the actual crack plane (Fig. 4.4). Then, the sample was manually loaded using the ball-bearing-tipped pin. A crack had been previously propagated down the slice, and thus the crack was propagated beyond the previous crack area to create a fresh tensile crack along the (10-14), resulting in a crack ~15 mm in length. Permanent ink was used on the slice as fiducial markers to demarcate the tip area for future scans. A 3.4 mm x 1.6 mm scan was collected while the specimen was under load (calcite_loaded) (Fig. 4.4). The load was then reduced slightly, and the tip area of the crack visibly self–healed spontaneously; the former crack tip area could not be optically distinguished from the slice following unloading. Three consecutive 0.17 mm x 1.4 mm scans were collected just beyond the visible cracktip area following unloading to capture the evolution of residual strain at the self-healed cracktip area (cracktip_unloaded 1, 2, 3) (Fig. 4.4). The vertical dimension of cracktip_unloaded 3 was decreased by 50 µm to enable scan completion within the experimental time-frame. The polychromatic beam at ALS beamline 12.3.2 has a spot size of 1 µm, and an energy range from 5 keV to 24 keV.

The scan areas were programmed using the beamline software. The stage translates and a single diffraction pattern was collected at each step as explained in Chapter 3. Step sizes for the loaded and control scans were large (10-20 µm) to characterize a large area of the slice at the cost of resolution, while step sizes for the cracktip_unloaded scans were small (2 µm) to generate high-resolution strain maps of the area. Each scan took several hours to complete. Most notably, cracktip_unloaded scans 1 and 2 collected approximately 59,000 images and

each took 16 hours to complete, and cracktip_unloaded 3 collected approximately 45,000 images and took 12 hours to complete. For this reason, the scan maps need to be considered as a series of diffraction patterns collected with several hours between the first and last diffraction pattern.

4.3 Results

The diffraction images were indexed as described in Chapter 3. The indexation of the single crystal remains the same throughout the control, loaded, and unloaded scans (Fig. 4.5a, b, c), however the Loaded scan shows a few more peaks collected on the right side of the detector (Fig. 4.5b). This is because the shadow on the right side of the detector is caused double-torsion device, and because the Loaded scan is so large, the device translates significant distances and thus the shadow on the detector also moves.
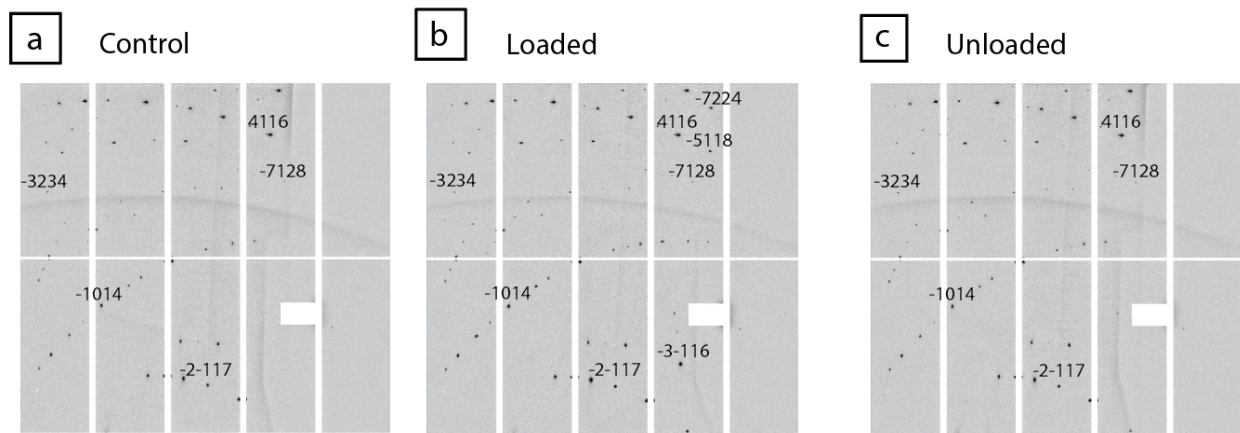
Figure 4.5: *Indexed diffraction images from the (a) control scan, (b) loaded scan, and (c) cracktip_unloaded scan #3. Indexation remains the same for all three scans, except the loaded scan shows a few more peaks to the right of the detector. This is because the scan is so large that shadow on the detector moves as the double-torsion device moves during the scan.*

The deviatoric strain tensor was calculated for each diffraction image as described in Chapter 3. The stress tensor (σ) is calculated from the strain tensor (ϵ) by applying Hooke's law $\sigma = \epsilon\, C_{ij}$ where C_{ij} is the elasticity tensor of calcite (Hearmon, 1979). Von Mises stress was also calculated for each scan:

$$\sigma_{vm} = \sqrt{\frac{(\sigma_{11} - \sigma_{22})^2 + (\sigma_{22} - \sigma_{33})^2 + (\sigma_{33} - \sigma_{11})^2 + 6(\sigma_{12}^2 + \sigma_{23}^2 + \sigma_{31}^2)}{2}}$$

The control scan showed values of strain higher than expected (Table 4.1), which suggests that the slice contains inherent strain prior to cracking, or that the beamline geometry

	Von Mises stress (MPa)	ϵ_{xx} (10^{-3})	ϵ_{yy} (10^{-3})	ϵ_{zz} (10^{-3})
Min value	366	1.69	0.734	-3.75
Max value	512	2.52	1.59	-3.00

Table 4.1: *Minimum and maximum values of calcite control scan*
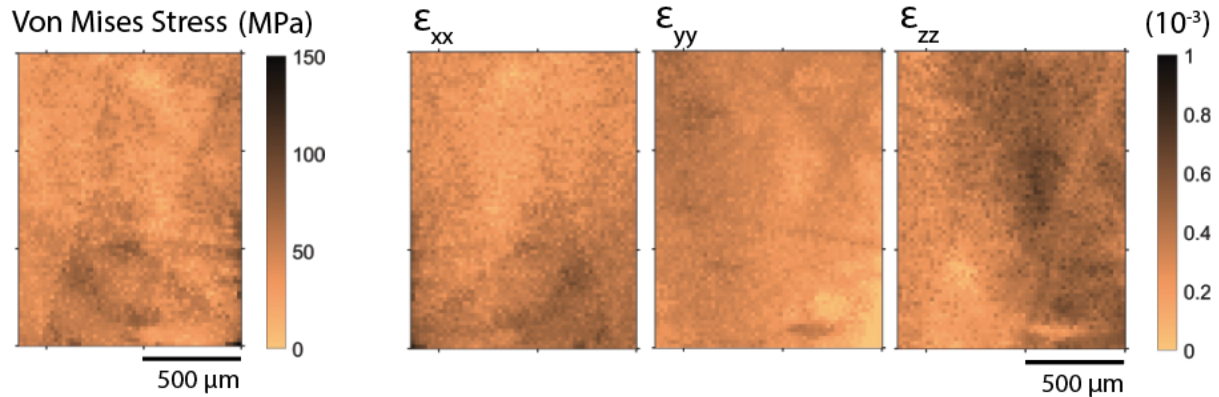
Figure 4.6: *Maps of control scan Von Mises stress (MPa), and deviatoric strain components ϵ_{xx}, ϵ_{yy}, ϵ_{zz} (10^{-3}) with minimum control values subtracted.*

produces strain artifacts in the diffraction pattern which could be due to the thickness of the sample and variability in the scattering origin, x-ray permeability of calcite and the index of refraction, discussed later. To correct for this high strain, the minimum value from each field of the control scan was subtracted from all values of each field of data presented here. Maps showing the effects of this subtraction on the control scan are shown in Fig. 4.6.

Following unloading, compressive strain in the Y direction perpendicular to the crack (ϵ_{yy}) is most diffuse in scan 1 and intensifies along the crack plane in scans 2 and 3. The deviatoric strain shows an accumulation of compressive strain in the Y direction, perpendicular to the crack plane (white line), and an accumulation of tensile strain in the Z direction (ϵ_{zz}), co-planar with the crack plane, is also observed with time. Deviatoric strain evolution in the X direction (ϵ_{xx}) appears to be negligible (Fig. 4.7).

The magnitude of strain also show a similar evolution of strain accumulation and re-laxation over the course of the three scans. Compressive strain perpendicular to the crack plane (ϵ_{yy}) becomes more negative between scan 1 to scan 3, from -2.759 millistrain to -3.372 millistrain, while the the maximum strain value concurrently becomes more positive between scans 2 and 3, from -1.365 millistrain to -0.053 millistrain (see Table 4.2). A similar trend is observed co-planar with the crack plane (ϵ_{zz}): tensile strain visibly accumulates along the crack plane. Maximum strain values increase slightly from scan 1 to scan 3, from 3.417
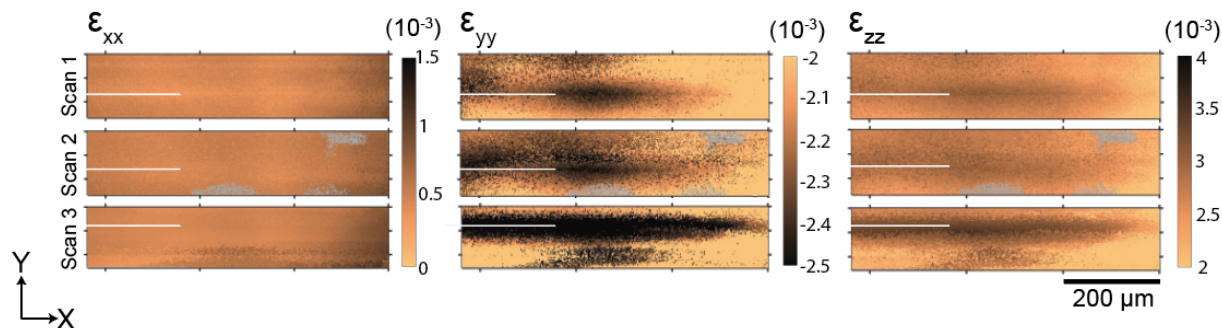
Figure 4.7: *Deviatoric strains (ϵ_{xx}, ϵ_{yy}, ϵ_{zz}) for calcite_unloaded scans 1 (top), 2 (middle) and 3 (bottom). Minimum value from the control scan for each ϵ_{xx}, ϵ_{yy}, ϵ_{zz} has been subtracted and the corrected values are plotted. The crack plane location in the scan is marked with a white line and is parallel to [10-14]. Gray pixels are those which were not indexed and removed from analysis.*

	ϵ_{xx} (10^{-3})			ϵ_{yy} (10^{-3})			ϵ_{zz} (10^{-3})			Von Mises stress (MPa)		
	Min	Max	Std Dev	Min	Max	Std Dev	Min	Max	Std Dev	Min	Max	Std Dev
Scan 1	0.2645	0.9870	±0.12	-2.759	-1.289	±0.19	1.464	3.417	±0.03	42	174	±19
Scan2	0.3121	1.041	±0.48	-2.946	-1.365	±0.31	1.357	3.545	±0.35	50	172	±96
Scan3	0.2868	1.432	±0.23	-3.372	-0.0529	±0.53	0.0763	3.796	±0.61	0	258	±43

Table 4.2: *Minimum and maximum deviatoric strain values and Von Mises stress values for cracktip_unloaded scans 1, 2, and 3.*

millistrain to 3.796 millistrain, but more notably strain relaxation occurs between scan 1 to scan 3 as the minimum tensile strain magnitude decreases from 1.464 millistrain to 0.076 millistrain.

Understanding the evolution of strain geometry and magnitude around the crack plane is aided by taking the profile of a line segment A to A' (Fig. 4.8a, b) and plotting the strain magnitudes (Fig. 4.8c, d) and stress magnitudes (Fig. 4.8e, f) relative to the Y stage coordinates. An increase in compressive strain magnitude in the Y-direction (ϵ_{yy}) is observed between scan 1 to scan 3 (Fig. 4.8c). A similar trend is observed in tensile strain magnitude in the Z direction (ϵ_{zz}) (Fig. 4.8d). Correspondingly, increasingly negative ϵ_{yy} stress values are observed with time, and the breadth of the crack area is clearly delineated with high stress magnitude by scan 3 (Fig. 4.8e). A similar trend is seen in ϵ_{zz} (Fig. 4.8f). Note that stress values are negative in ϵ_{zz} due to the auxetic nature of calcite.

Von Mises stress is used to represent the general stress present in the system because it considers both the normal and shear stress components. Similar to the deviatoric strain, an increase in magnitude of Von Mises stress is observed to accumulate around the crack plane
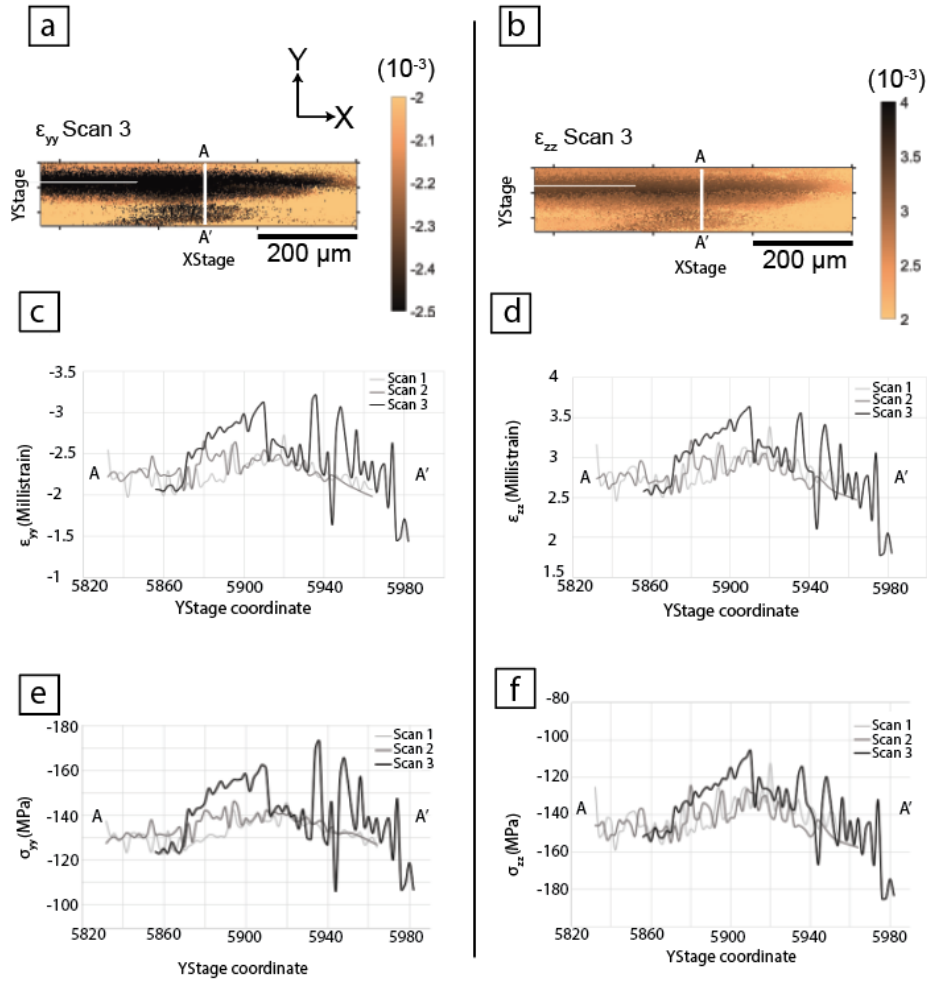
Figure 4.8: *Line profiles of deviatoric strain across cracktip_unloaded scans 1, 2, and 3. Location of line segment A to A' on cracktip_unloaded Scan 3 map of (a) ϵ_{yy} and (b) ϵ_{zz}. Magnitudes of (c) ϵ_{yy} (d) ϵ_{zz} , (e) σ_{yy} and (f)σ_{zz} along line segment A to A'.*
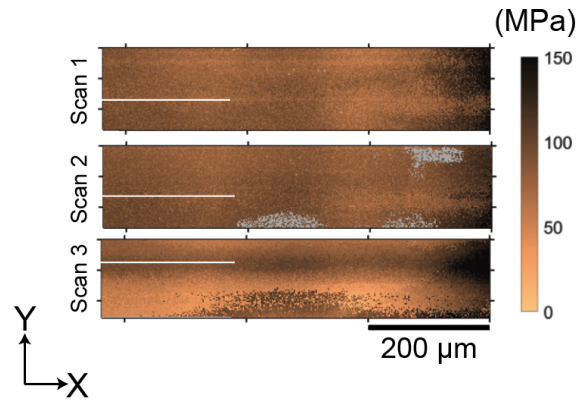
Figure 4.9: *a) Von Mises stress (MPa) of cracktip unloaded scans 1,2, and 3. Gray pixels are those which were not indexed and removed from analysis. The crack plane location is marked with a white or gray line and is parallel to (10-14).*

by scan 3 and relaxes elsewhere; correspondingly, maximum Von Mises stress values increase from 174 to 258 MPa and minimum stress values decrease from 50 MPa to 0 MPa over the course of the three scans (Fig. 4.9).

The prior discussion has only considered the elastic strains. The elastic strain and elastic strain evolution is linked to the evolution of plastic deformation in the lattice; it is the dislocations and defects that distort the lattice and cause the measurable changes in elastic strain, i.e. relative peak shifts. Plastic deformation manifests as peak broadening and change in peak shape (Barabash et al., 2003). Increase in peak width appears to be correlated to the same areas showing deviatoric strain (Figs. 4.7, 4.10). In scan 3, an overall decrease in peak width is observed across the entire scan, and particularly along the crack plane (Figs. 4.10). Peak width values are only displayed for scans 2 and 3, which have been corrected for beam decay, as explained above, to eliminate the dependency of the peak width on beam intensity. Because the beam was not decaying during scan 1, there was no dependency on peak width to beam intensity, and thus the peak width values could not be corrected in the same way and therefore are not shown.
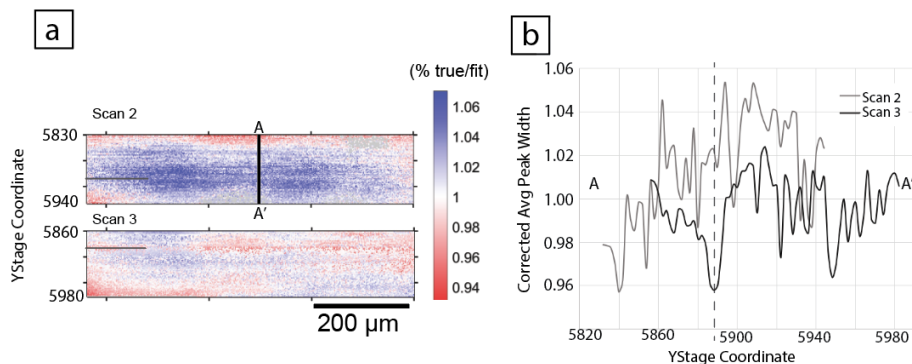
Figure 4.10: *(a) Map of corrected average diffraction peak width for cracktip_unloaded scans 2 and 3, (b) line profile of average peak width along line segment A to A' shown in (a). The crack plane location is marked with a gray line and is parallel to (10-14).*

4.4 Possible sources of error and data corrections

The entire thickness of the slice was penetrated by the polychromatic x-ray beam. Based on the composition and thickness of the slice (1 mm), only photons with energy greater than 10 keV could penetrate into the sample thickness, and only 40% of the 20 keV photons were transmitted through the entire thickness of the slice (source: CXRO X-ray Database). Therefore, diffraction can originate at any point along the x-ray path within the 1 mm thickness (t) (Fig. 4.11). This variability can produce a strain artifact by altering the true central coordinate of the diffraction pattern. Each diffraction pattern has a pair of x and y coordinates (xcent, and ycent, respectively) in the diffraction image coordinate system (x,y) (different from the laboratory coordinate system X,Y,Z) marking the shortest distance between the diffraction origin in the sample and the detector (dd). During calibration, the scattering origin (y_1) is determined, and its corresponding coordinate (ycent$_1$). The xcent coordinate is also assigned, but is not altered by thickness of the sample. Theoretical peak positions are calculated using this central coordinate position (xcent, ycent$_1$). Therefore, if the true point of diffraction origin occurs at a different point along the beam path (y_0), this results in a a deviation ($ydev$) between the experimental peak position and theoretical peak position caused by the difference in scattering location and unrelated to strain. This therefore manifests as artificial strain measured. Each pixel on the Dectris Pilatus 1M detector is 172 µm x 172 µm, so a deviation in peak position equivalent to the thickness of the sample $t = 1$ mm would span 5.81 pixels. As an example, the average deviation in y-coordinate position between experimental and theoretical peak positions for the control scan (Fig. 4.6) is 2.17 pixels. The exact source of the deviation of y-coordinates in this scan is uncertain, however the difference between the set ycent and the true ycent values could contribute. To account deviation in ycent due to sample thickness, the value of ycent can be refined to an extent during XMAS strain refinement to minimize this error (see Chapter 3) but was not refined
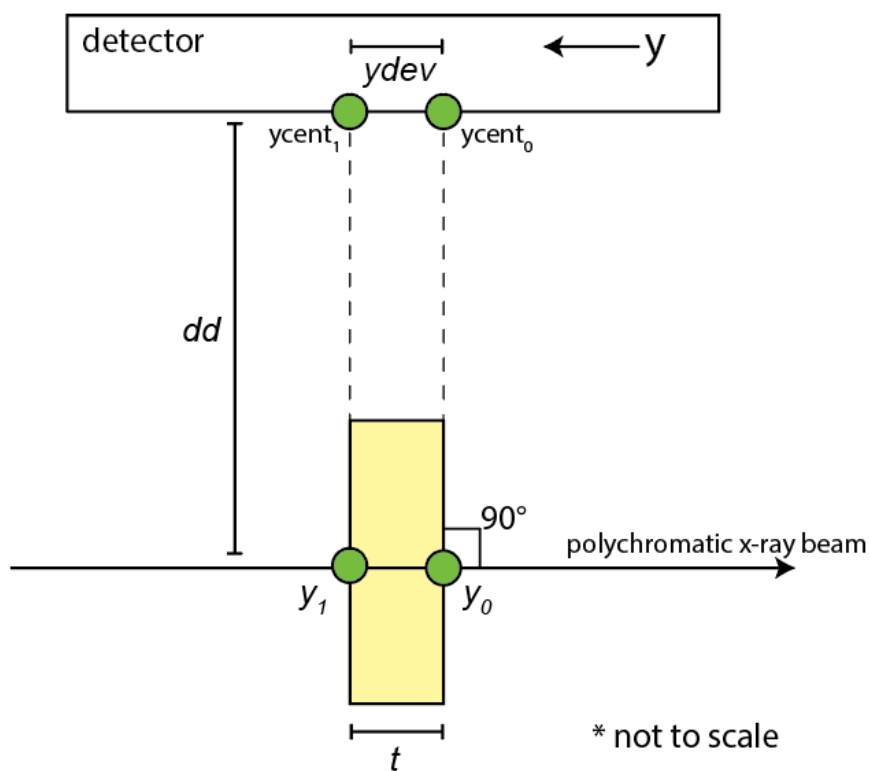
Figure 4.11: *Schematic showing how deviation in the origin of scattering, between y_0 and y_1, along thickness (t) of sample (yellow rectangle) some distance from the detector (dd) can cause deviation in the central y-coordinate of the diffraction pattern ($ycent_0$, and $ycent_1$).*

in this analysis so that all corrections could be applied systematically.

Because the sample can be completely penetrated by x-rays, as explained above, the effects on the travel path by calcite's index of refraction on rays originating from the crystal interior should be considered. Reflections originating from the interior of the crystal must exit the crystal through the crystal-air interface, compared to reflections that originate from the sample surface. This means that on a single diffraction pattern, reflected peaks and transmitted peaks are both present, but peak position from transmitted rays could be shifted due calcite's optical refractive index. However, the refractive index for x-ray radiation only differs a very small amount from unity (Attwood & Sakdinawat, 2016) and thus is generally considered negligible. Additionally, this was tested by removing the reflected peaks from analysis which did not produce a significant difference in overall strain values.

During the final two scans of the experiment, cracktip_unloaded scan 2 and 3, the synchrotron storage ring experienced injection issues and the beam went into "decay mode" during which the electrons slowly lose energy over time and there is no injection of high-energy electrons into the storage ring, and thus the intensity and flux of the beam decreases

gradually. Historically the beamline scientist had noticed a relationship between beam intensity and peak broadness in previous experiments conducted during beam decay. In this case, a relationship was found between beam intensity and peak width to correct for this phenomenon. For both scans cracktip_unloaded scans 2 and 3, a 2nd degree polynomial function was fit to describe the relationship between peak width and beam intensity, with beam intensity as the independent variable and peak width as the dependent variable. The measured peak width values were then divided by the function-generated peak width values to remove their dependency on beam intensity and replotted.

4.5   Discussion

Laue microdiffraction measures elastic strain, which is a result of the distortion of the lattice under stress. Such stress can be imposed externally, or also by the emplacement of alterations such as defects and dislocations that create areas of localized strain within the lattice. The accumulation of increasingly compressive strain perpendicular to the crack and tensile strain co-planar with the crack observed over the course of the three cracktip_unloaded scans following unloading (Fig. 4.7 suggests the mobilization of plasticity, i.e. dislocations and defects, in the lattice. Line profiles of the area reveal the "zone of plasticity," where elastic strain is the highest surrounding the crack plane (Fig. 4.8).

Without transmission electron microscopy (TEM) studies or sample surface etching to verify the presence of dislocations, plasticity is indicated by increased peak width in the diffraction patterns, as observed around the crack area (Barabash et al., 2003) (Fig. 4.10). The overall decrease in peak width from scan 2 to scan 3 suggest an overall decrease in defects and dislocations in the lattice of the bulk crystal, which corroborates the implication that dislocations are migrating towards the fracture surface where they are then released. This is further supported by the drastic decrease in peak width at the center of the zone of plasticity when traversing the crack surface.

This implies that the stress imposed on the system from the double-torsion device, and that which remained in the lattice following the propagation of the fracture, was high enough to overcome Peierls stress and mobilize dislocations (Nabarro, 1967; Meike, 1988; Lawn, 1993). Calcite has a number of dislocation glide systems (e.g. Barber & Wenk, 1976). Low temperature torsion of single crystal calcite has demonstrated slip along $\mathbf{r} = \{10\text{-}14\} <20\text{-}2\text{-}1>$ and $\mathbf{f} = \{\text{-}1012\} <0\text{-}22\text{-}1>$ systems, and twinning on $\mathbf{e} = \{\text{-}1018\} <40\text{-}41>$ (Barber et al., 2007). The crack plane is (10-14) and thus dislocation mobility along it could be probable. Additionally, the $\{\text{-}1012\}$ planes are oriented at an angle to the crack plane (Fig. 4.12), and therefore dislocation movement along these glide planes would intersect with the crack surface, suggesting that these glide planes could facilitate the movement of dislocations towards the crack surface, and also allow for dislocations to be released. While twinning was not observed during this experiment, the (-1018) twin plane could also serve as a conduit in dislocation mobility. Diffusion of vacancies toward the free surface (Lloyd & Nakahara, 1978) which can be activated with elastic stress fields (Pendl & Hochrainer, 2023) could also
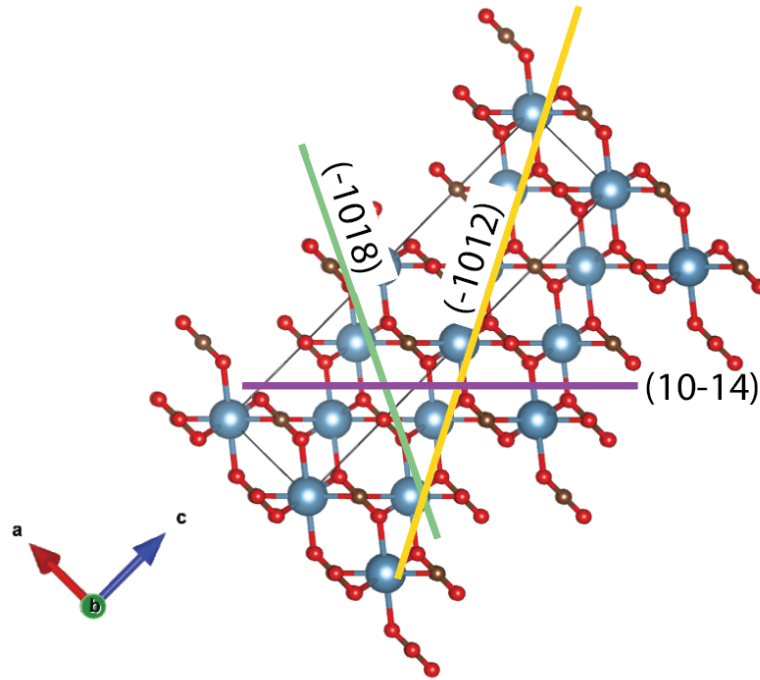
Figure 4.12: *Calcite crystal structure with crack plane (10-14), glide plane (-1012), and twin plane (-1018) labelled. Blue is Ca, C is brown, O is red. Crystal coordinate axes a,b,c shown. Note that calcite is trigonal and the angle between a and b is 120°, which cannot be seen due to the angle of the lattice in this view.*

be at play. With increasing time, the movement of the defects and dislocations is such that they produce an increasingly compressive stress perpendicular to the crack surface, forcing the fracture surface back together and promote healing. Future studies to visualize the dislocation mobility during crack healing such as by using TEM or sample surface etching would benefit this study.

4.6 Conclusions

The use of synchrotron x-ray Laue microdiffraction produced high resolution maps of the elastic strain around the crack tip following unloading of the calcite slice. The elastic strain field surrounding the crack displayed a strong compressive strength that increased in magnitude and accumulated closer to the crack plane as time progressed following unloading. Simultaneously increased peak width indicative of the presence of plastic deformation was observed in the same area showing high elastic strain magnitude, and by scan 3, the crack plane showed a dramatic decrease in peak width suggesting the removal of dislocations from

the crack surface. These findings suggest that the stress exerted on the system from the double-torsion device was great enough to initiate the mobility of the dislocations throughout the lattice and possibly migrate towards the free surface possibly facilitated by the {10-14} and {-1012} glide planes. This new synchrotron x-ray diffraction technique presents novel findings on the movement of plasticity surrounding a crack plane in calcite.

Chapter 5

Concluding remarks

In this dissertation, three different projects exploring microstructures in geologic materials investigated with synchrotron-based x-ray diffraction techniques have been presented: the deformation behavior of hydrous high-pressure phases D, Egg, and δ-AlO(OH) at mantle conditions using a DAC in radial diffraction geometry; the ability of scanning Laue microdiffraction to measure residual strain and determine the paleostress orientation in natural and experimentally deformed quartzites and the limitations of the methodology were elucidated; and the strain field around a crack in a single crystal of calcite was studied using scanning Laue microdiffraction to measure and visualize the mobilization of plasticity during crack healing.

The well-established radial DAC technique was used to investigate the deformation behavior of high-pressure hydrous phases and their potential contribution to mid-mantle seismic anisotropy. Starting materials of serpentine and kaolinite were used in a radial DAC set up and brought to 20+ GPa and transformed to hydrous phases D, Egg, and δ-AlO(OH) using a double-sided infrared laser heating system. Following transformation, the pressure was increased and diffraction patterns were captured to track the evolution of texture development. Phases D and Egg demonstrated an (001) maxima of 7.37 m.r.d. and 10.33 m.r.d., respectively, aligned parallel to the compression direction indicating basal slip as the primary deformation mechanism. VPSC modeling confirmed that dominant slip along (001) at 50% strain in phase D produces an excellent fit with the observed texture of the deformed aggregate. For δ-AlO(OH), an (010) maxima of 2.97 m.r.d. was observed aligned parallel to the compression axis. In trigonal phase D, monoclinic phase Egg and orthorhombic δ-AlO(OH), sheet-like planes of their crystal structures appear to align themselves perpendicular to the principal axis of compression when a differential stress is applied. VPSC modeling is needed to confirm the potential deformation mechanisms responsible for the deformation texture in phase Egg and δ-AlO(OH). The calculated single crystal P-wave anisotropy and shear-wave splitting for all three phases is comparable to or greater than other mantle phases suggesting that they could significantly affect seismic anisotropy in the mantle transition zone. Further investigation is needed to estimate the volume percentage of hydrous phases present in the mid-mantle. Incorporating these deformation behaviors into geodynamic models would

aid in understanding whether or not texture development and deformation mechanisms of these phases improves the simulations. Further investigations are needed to investigate the deformation behavior of δ-AlO(OH), which is more anisotropic than many mantle phases including bridgmanite, and its significance on anisotropy in the lower mantle.

Scanning Laue microdiffraction was used to measure the residual strain in quartzites. The technique, holds a thin section of quartzite at 45° to the incident beam and collects diffraction images in reflection geometry during a raster scan. The deviatoric strain tensor is measured from the relative peak shifts in the diffraction images from an ideal, unstrained lattice, which is then used to determine the principal strain tensor. This technique had been used to estimate the magnitude of paleostress (Kunz et al., 2009), and then the orientation of the paleostress (Chen et al., 2016; Wenk et al., 2020). In this study, the limitations of the methods ability to infer the paleostress orientation were explored. The technique can infer reasonable paleostress orientations from samples without heavy plastic deformation, exhibiting small, uniform diffraction peaks, such as vein quartzite (HSM from Hong Kong) or rolled Ti that had recrystallized during the hot-rolling process. For HSM, the axis of compression was oriented perpendicular to the long axes of the grains, and for the rolled Ti, the axis of compression was parallel with the normal direction and the principal axis of extension was parallel with the rolling direction, as evidenced by the grain shape. However, for samples with high amounts of plastic deformation, the diffraction peaks broaden and become irregularly shaped. Because the elastic strain is measured based on relative peak shifts, if the peak intensity distribution does not fit the Gaussian distribution due to irregular shape, the subpixel shifts in peak location caused by elastic strain in the lattice cannot be detected. Therefore, for quartzites showing high amounts of plastic deformation with broad, irregular peaks, such as quartzite from explosion structures (Ko1) and quartzite deformed in a piston apparatus (H2), the principal strain patterns exhibit incomprehensible strain patterns that show two maxima of compression and extension along the vertical axis and inclined 45° to the Z axis. Exactly why this pattern shows up across a number of samples exhibiting heavy plastic deformation needs to be investigated further.

Scanning Laue microdiffraction was also used to measure the strain field around a Mode I crack along the (10-14) in calcite in a series of three scans collected over 44 hours following load removal. This was a new experimental geometry with a custom built double-torsion device that held the slice of calcite perpendicular to the incident beam. The scans demonstrated an increasing compressive stress perpendicular to the crack plane over the three scans, and the migration of compressive strain towards the crack plane. A corresponding tensile stress was observe din the Z direction (coplanar with the crack surface). This suggests the mobility of defects towards the crack plane over time. The same trend observed with strain around the crack was observed with peak broadening, indicative of plastic deformation. A decrease in plastic deformation was observed on the crack plane by the third scan, suggesting that the defects were being eliminated along the crack plane. Common low temperature glide planes $\mathbf{r} = \{10\text{-}14\}$ <20-2-1> and $\mathbf{f} = \{\text{-}1012\}$<0-22-1> systems, and twinning on $\mathbf{e} = \{\text{-}1018\}$<40-41> (Barber et al., 2007), in calcite are oriented to intersect with the (10-14) and could facilitate the migration of defects in the lattice observed in the

study. This study suggests that the stress imposed on the lattice from the double-torsion device was high enough to generate plasticity in the lattice, and also to overcome the Peierls stress and mobilize dislocations. However, the mobility of dislocations was only inferred based on measures of elastic and plastic strain. Future studies to visualize the mobility of plastic strain using TEM or surface etching would be useful to verify the conclusions made in this study.

Synchrotron x-ray diffraction techniques offer the ability to conduct experiments using high intensity and high brightness x-ray beam that allows the collection of data for experiments that could not be collected using benchtop x-ray beams. These include high-pressure high-temperature texture studies on mantle phases in a diamond anvil cell, and scanning Laue microdiffraction to study the elastic strain in quartzites and around cracks in calcite. These techniques allow the study of microstructure in these crystalline geologic materials which study possible sources of anisotropy in the mid-mantle, the paleostress orientations of surficial rocks like quartzite to help verify the forces that shaped the landscapes, and fracture mechanics in calcite, a necessity to understand and control mineralization in geothermal reservoirs and hydrocarbon basins.

Bibliography

Atkinson, B. (1984). Subcritical crack growth in geological materials. *J. Geophys. Res.*, *89*, 4077–40414.

Attwood, D., & Sakdinawat, A. (2016). *X-rays and Extreme Ultraviolet Radiation: Principles and Applications*. Cambridge University Press.

Barabash, R., Ice, G., & Walker, F. (2003). Quantitative microdiffraction from deformed crystals with unpaired dislocations and dislocation walls. *J. Appl. Phys.*, *93*, 1457–1464.

Barber, D., & Wenk, H.-R. (1976). Defects in deformed calcite and carbonate rocks. In H.-R. Wenk (Ed.), *Electron Microscopy in Mineralogy* (pp. 428–442). Springer-Verlag.

Barber, D., Wenk, H.-R., Gomez-Barreiro, J., Rybacki, E., & Dresen, G. (2007). Basal slip and texture development in calcite new results from torsion experiments. *Phys. Chem. Minerals*, *34*, 73–84.

Blackman, D., Kendall, J.-M., Dawson, P., Wenk, H.-R., Boyce, D., & Morgan, J. (1996). Teleseismic imaging of subaxial flow at mid-ocean ridges: Traveltime effects of anisotropic mineral texture in the mantle. *Geophys. J. Int.*, *127*, 415–426.

Blackman, D., Wenk, H.-R., & Kendall, J. (2002). Seismic anisotropy of the upper mantle 1. Factors that affect mineral texture and effective elastic properties. *Geochem. Geophys. Geosystems*, *3*, 8601.

Blicharski, M., Nourbakhsh, S., & Nutting, J. (1979). Structure and properties of plastically deformed α-Ti. *Geochem. Geophys. Geosystems*, *13*, 516–522.

Bragg, W. (1913). The reflection of X-rays by crystals. II. *Proc. Roy. Soc. A*, *88*, 246–248.

Bragg, W., & Bragg, W. (1913). The reflection of X-rays by crystals. *Proc. Roy. Soc. A*, *88*, 428–438.

Britton, T., & Wilkinson, A. (2011). Measurement of residual strain and lattice rotations with high resolution electron backscatter diffraction. *Ultramicroscopy*, *111*, 1395–1404.

Chan, L., & Alvarez, W. (2023). Natural explosion structures in rocks. *J. Struct. Geol.*, *174*, 104933.

Chandler, B., Bernier, J., Diamond, M., Kunz, M., & Wenk, H.-R. (2021a). Exploring microstructures in lower mantle mineral assemblages with synchrotron x-rays. *Sci. Adv.*, *7*, eabd3614.

Chandler, B., Chen, L.-W., Li, M., Romanowicz, B., & Wenk, H.-R. (2021b). Seismic anisotropy, dominant slip systems and phase transitions in the lowermost mantle. *Geophys. J. Int.*, *227*, 1665–1681.

Chen, K., Kunz, M., Li, Y., Sintubin, M., Zepeda, E., & Wenk, H.-R. (2016). Compressional residual stress in Bastogne boudins revealed by synchrotron X-ray microdiffraction. *Geophys. Res. Lett., 43*, 6178–6185.

Chen, K., Kunz, M., Tamura, N., & Wenk, H.-R. (2011). Evidence for high stress in quartz from the impact site of Vredefort, South Africa. *Eur. J. Mineral., 23*, 169–178.

Chen, K., Kunz, M., Tamura, N., & Wenk, H.-R. (2015). Residual stress preserved in quartz from the San Andreas Fault Observatory at Depth. *Geology, 43*, 219–222.

Croft, M., Zhong, Z., Jisrawi, N., Zakharchenko, I., Holts, R., Skaritka, J., Fast, T., Sadananda, K., Lakshmipathy, M., & Tsakalakos, T. (2005). Strain profiling of fatigue crack overload effects using energy dispersive X-ray diffraction. *Int. J. Fatigue, 27*, 1408–1419.

Currie, C., Cassidy, J., Hyndman, R., & Bostock, M. (2004). Shear wave anisotropy beneath the Cascadia subduction zone and western North American craton. *Geophys. J. Int., 157*, 341–353.

Dawson, P., & Wenk, H.-R. (2000). Texturing of the upper mantle during convection. *Philosophical Magazine A, 80*, 572–598.

Eggleton, R., Boland, J., & Ringwood, A. (1978). High pressure synthesis of a new aluminum silicate: $Al_5Si_5O_{17}(OH)$. *Geochem. J., 12*, 191–194.

Frenzel, M., & Woodcock, N. (2014). Cockade breccia: Product of mineralisation along dilational faults. *J. Struct. Geol., 68*, 194–206.

Friedrich, W., Knipping, P., & Laue, M. (1912). Interferenz-Erscheinungen bei Röntgenstrahlen. *Sitzungsberichte der Kgl. Bayer. Akad. der Wiss*, 303–322.

Girard, J., Ukelele, G., Farla, R., Mohiuddin, A., & Karato, S. (2016). Shear deformation of bridgmanite and magnesiowustite aggregates at lower mantle conditions. *Science, 351*, 144–147.

Goryaeva, A., Carrez, P., & Cordier, P. (2016). Low viscosity and high attenuation in $MgSiO_3$ post-perovskite inferred from atomic-scale calculations. *Sci. Rep., 6*, 34771.

Goryaeva, A., Carrez, P., & Cordier, P. (2017). Modeling defects and plasticity in $MgSiO_3$ post-perovskite: Part 3- Screw and edge [001] dislocations. *Phys. Chem. Minerals, 44*, 521–533.

Griggs, D. (1938). Deformation of single calcite crystals under high confining pressures. *Am. Min., 23*, 28–33.

Hearmon, R. (1979). The elastic constants of crystals and other anisotropic materials. In K. Hellwege & A. Hellwege (Eds.), *Landolt-Bornstein Numerical Data and Functional Relationships in Science and Technology, iii/11* (pp. 1–244). Springer-Verlag.

Helffrich, G. (2000). Topography of the transition zone seismic discontinuities. *Rev. Geophys., 31*, 141–158.

Hirth, G., & Tullis, J. (1992). Dislocation creep regimes in quartz aggregates. *J. Struct. Geol., 14*, 145–159.

Hobbs, B. (1968). Recrystallization of single crystals of quartz. *Tectonophysics, 6*, 353–401.

Hosford, W. (2005). *Mechanical Behavior of Materials*. Cambridge University Press.

Hull, D., & Bacon, D. (2011). *Introduction to Dislocations*. Elsevier Science Technology.

Hutchings, M., Hippsley, C., & Rainey, V. (1990). Neutron diffraction measurement of the stress field during fatigue cycling of a cracked test specimen. *Mat. Res. Soc. Symp. Proc.*, *166*, 317–321.

Irwin, G. (1957). Analysis of stresses and strains near the end of a crack traversing a plate. *J. Appl. Mechanics*, 361–364.

Ita, J., & Stixrude, L. (1992). Petrology, elasticity, and composition of the mantle transition zone. *J. Geophys. Res.*, *97*, 6849–6866.

Iwamori, H. (2004). Phase relations of peridotites under H_2O-saturated conditions and ability of subducting plates for transportation of H_2O. *Earth Planet. Sci. Lett.*, *227*, 57–71.

Jeanloz, R., & Thompson, A. (1983). Phase transitions and mantle discontinuities. *Rev. Geophys. Space Phys.*, *21*, 51–74.

Kantor, I., Prakapenka, V., Kantor, A., Dera, P., Kurnosov, A., Sinogeikin, S., Dubrovinskaia, N., & Dubrovinsky, L. (2012). BX90: A new diamond anvil cell design for X-ray diffraction and optical measurements. *Rev. Sci. Instrum.*, *83*, 125102.

Kelleher, J., Prime, M., Buttle, D., Mummery, P., Webster, P., Shackleton, J., & Withers, P. (2003). The measurement of residual stress in railway rails by diffraction and other methods. *J. Neutron Res.*, *1*, 187–193.

Kinsland, G., & Bassett, W. (1975). Modification of the diamond cell for measuring strain and the strength of materials at pressures up to 300 kilobar. *Rev. Sci. Instrum.*, *47*, 130–133.

Knopf, E. (1946). Study of experimentally deformed rocks. *Science*, *103*, 99–103.

Kohlstedt, D., & Goetze, G. (1974). Low-stress high-temperature creep in olivine single crystals. *J. Geophys. Res.*, *79*, 2045–2051.

Komatsu, K., Kuribayashi, T., Sano, A., Ohtani, E., & Kudoh, Y. (2006). Redetermination of the high-pressure modification of AlOOH from single-crystal synchrotron data. *Acta Cryst.*, *E62*, i216–i218.

Kunz, M., Chen, K., Tamura, N., & Wenk, H.-R. (2009). Evidence for residual stress in deformed natural quartz. *Am. Min..*, *94*, 1059–1062.

Kunz, M., Yan, J., Cornell, E., Domning, E., Yen, C., Doran, A., Beavers, C., Treger, A., Williams, Q., & MacDowell, A. (2018). Implementation and application of the peak scaling method for temperature measurement in the laser heated diamond anvil cell. *Rev. Sci. Instrum.*, *89*, 083903.

Laue, M. v. (1920, December). Concerning the Detection of X-ray Interferences [Nobel Lecture, June 3, 1920, [Accessed: April 22, 2014]]. https://www.nobelprize.org/prizes/physics/1914/laue/lecture/

Lawn, B. (1993). *Fracture of Brittle Solids*. Cambridge University Press.

Lebensohn, R., & Tomé, C. (1993). A self-consistent anisotropic approach for the simulation of plastic deformation and texture development of polycrystals: Application to zirconium alloys. *Acta. metall. mater.*, *41*, 2611–2624.

Li, Y., Chen, K., Zhang, F., Tamura, N., Ku, C.-S., & Wenk, H.-R. (2020). XtalCAMP: A comprehensive program for the analysis and visualization of scanning Laue X-ray micro-/nanodiffraction data. *J. Appl. Cryst.*, *53*, 1392–1403.

Liu, A. (2005). *Mechanics and Mechanism of Fracture: An Introduction*. ASM International.

Liu, L.-G. (1986). Phase transformations in serpentine at high pressures and temperatures and implications for subducting lithosphere. *Phys. Earth. Planet. Int.*, *42*, 255–262.

Lloyd, J., & Nakahara, S. (1978). On the diffusion of excess vacancies to free surfaces and voids in thin films. *J. Electrochem. Soc.*, *125*(2037).

Long, M. (2013). Constraints on subduction geodynamics from seismic anisotropy. *Rev. Geophys.*, *51*, 76–112.

Long, M., & Silver, P. (2008). The subduction zone flow field from seismic anisotropy: A global view. *Science*, *319*, 315–318.

Long, M., & van der Hilst, R. (2006). Shear wave splitting from local events beneath Ryuku arc: Trench-parallel anisotropy in the mantle wedge. *Phys. Earth and Planet. Int.*, *155*, 300–312.

Lunt, J., & Korsunsky, A. (2015). A review of micro-scale focused ion beam milling and digital image correlation analysis for residual stress evaluation and error estimation. *Surf. Coat. Technol.*, *283*, 373–388.

Lutterotti, L., Matthies, S., Wenk, H.-R., Schultz, A., & Richardson, Jr., J. (1997). Combined texture and structure analysis of deformed limestone from time-of-flight neutron diffraction spectra. *J. Appl. Phys.*, *81*, 594–600.

Lutterotti, L., Vasin, R., & Wenk, H.-R. (2014). Rietveld texture analysis from synchrotron diffraction images. I. Calibration and basic analysis. *Powd. Diff.*, *29*, 76–84.

Madrigal, P., Gazel, E., Flores, K., Bizimis, M., & Jicha, B. (2016). Record of massive upwellings from the Pacific large low shear velocity province. *Nature Comm.*, *7*, 13309.

Mainprice, D., Page, Y. L., Rodgers, J., & Jouanna, P. (2007). Predicted elastic properties of the hydrous D phase at mantle pressures: Implications for anisotropy of subducted slabs near 670-km discontinuity and in the lower mantle. *Earth Planet. Sci. Lett.*, *259*, 283–296.

Marone, C., Vidale, J., & Ellsworth, W. (1995). Fault healing inferred from time dependent variations in source properties of repeating earthquakes. *Geophys. Res. Lett.*, *22*, 3095–3098.

Matthies, S. (1996). Moment pole figures in residual stress analysis. *Text. and Microstr.*, *25*, 229–236.

Matthies, S., & Humbert, M. (1995). On the principle of a geometric mean of even-rank symmetric tensors for textured polycrystals. *J. Appl. Cryst.*, *28*, 254–266.

Matthies, S., & Vinel, G. (1982). On the reproduction of the orientation distribution function of texturized samples from reduced pole figures using the conception of a conditional ghost correction. *Phys. Stat. Sol. (b)*, *112*, K11.

McNamara, D., Lister, A., & Prior, D. (2016). Calcite sealing in a fractured geothermal reservoir: Insights from combined EBSD and chemistry mapping. *J. Volc. Geotherm. Res.*, *323*, 38–52.

Meike, A. (1988). Heterogeneous deformation resulting from stress gradients in calcite single crystals. *Phys. Chem. Minerals*, *16*, 148–156.

Merkel, S., Hemley, R., Mao, H.-k., & Teter, D. (2000). Finite-element modeling and ab initio calculations of megabar stresses in the diamond anvil cell. In M. Manghani, W. Nellis, & M. Nicol (Eds.), *Science and Tech. of High Pressure, Proceedings of the AIRAPT-17* (pp. 68–73).

Merkel, S., Kubo, A., Miyagi, L., Speziale, S., Duffy, T., Mao, H.-k., & Wenk, H.-R. (2006). Plastic deformation of $MgGeO_3$ post-perovskite at lower mantle pressures. *Science*, *311*, 644–646.

Merkel, S., & Yagi, T. (2005). X-ray transparent gasket for diamond anvil cell high pressure experiments. *Rev. Sci. Instru.*, *76*, 046109–3.

Miyagi, L., Kanitpanyacharoen, W., Kaercher, P., Lee, K., & Wenk, H.-R.-. (2010). Slip systems in $MgSiO_3$ post-perovskite: Implications for D" anisotropy. *Science*, *329*, 1639–1641.

Miyagi, L., & Wenk, H.-R. (2016). Texture development and slip systems in bridgmanite and bridgmanite + ferropericlase aggregates. *Phys. Chem. Mins.*, *43*, 597–613.

Montagner, J.-P. (1998). Where can seismic anisotropy be detected in the Earth's mantle? In boundary layers. *Pure Appl. Geophys.*, *151*, 223–256.

Mookherjee, M., Panero, W., Wunder, B., & Jahn, S. (2019). Anomalous elastic behavior of phase egg, $AlSiO_3(OH)$, at high pressures. *Am. Min.*, *104*, 130–139.

Nabarro, F. (1967). *Theory of Crystal Dislocations*. Oxford University Press.

Nishi, M., Irifune, T., Tsuchiya, J., Tange, Y., Nishihara, Y., Fujino, K., & Higo, Y. (2014). Stability of hydrous silicate at high pressures and water transport to the deep lower mantle. *Nature Geo.*, *7*, 224–227.

Noyan, I., & Cohen, J. (1987). *Residual Stress*. Springer.

Ohtani, E., Litasov, K., Hosoya, T., Kubo, T., & Kondo, T. (2004). Water transport into the deep mantle and formation of a hydrous transition zone. *Phys. Earth Planet. Int.*, *143-144*, 255–269.

Outwater, J., & Gerry, D. (1969). On the fracture energy, rehealing velocity and refracture energy of cast epoxy resin. *J. Adhesion*, *1*, 290–298.

Panning, M., & Romanowicz, B. (2006). A three-dimensional radially anisotropic model of shear velocity in the whole mantle. *Geophys. J. Int.*, *167*, 361–379.

Paterson, M. (1969). A high-pressure, high-temperature apparatus for rock deformation. *Int. J. Rock Mech. Min. Sci.*, *7*, 517–526.

Pendl, K., & Hochrainer, T. (2023). Coupling stress fields and vacancy diffusion in phase-field models pure vacancy phase. *Computational Materials Science*, *224*, 112157.

Prescher, C., & Prakapenka, V. (2015). DIOPTAS: A program for reduction of two-dimensional X-ray diffraction data and data exploration. *High Press. Res.*, *35*, 223–230.

Raleigh, C. (1968). Mechanisms of plastic deformation of olivine. *J. Geophys. Res.*, *73*, 5391–5406.

Renner, J., Evans, B., & Siddiqi, G. (2002). Dislocation creep of calcite. *J. Geophys. Res.*, *107*, 2364.

Ringwood, A., & Major, A. (1967). High-pressure reconnaissance investigations in the system Mg_2SiO_4 MgO H_2O. *Earth. Planet. Sci. Lett.*, *2*, 130–133.

Ritchie, R. (1988). Mechanisms of fatigue crack propagation in metals, ceramics and composites: Role of crack tip shielding. *Mat. Sci. Engin.*, *A103*, 15–28.

Ritchie, R. (1999). Mechanisms of fatigue crack propagation in ductile and brittle solids. *Int. J. Fracture*, *100*, 55–83.

Rosa, A., Sanchez-Valle, C., Nisr, C., Evans, S., Debord, R., & Merkel, S. (2013). Shear wave anisotropy in textured phase D and constraints on deep water recycling in subduction zones. *Earth. Planet. Sci. Lett.*, *377-378*, 13–22.

Royne, A., Bisschop, J., & Dysthe, D. (2011). Experimental investigation of surface energy and subcritical crack growth in calcite. *J. Geophys. Res.*, *116*, B04204.

Sander, B., Felkel, E., & Drescher, F. (1929). Festigkeit und Gefügeregel am Beispiele eines Marmors. *Neues Jahrb. Mineral. Geol.*, *59*, 1–26.

Schajer, G. (2013). *Practical Residual Stress Measurement Methods*. Wiley.

Schulze, K., Pamato, M., Kurnosov, A., Ballaran, T., Glazyrin, K., Pakhomova, A., & Marquardt, K. (2018). High-pressure single crystal structural analysis of $AlSiO_3OH$ phase egg. *Am. Min.*, *103*, 1975–1980.

Shyam, A., & Lara-Curzio, E. (2006). The double-torsion testing technique for determination of fracture toughness and slow crack growth behavior of materials: A review. *J. Mater. Sci.*, *41*(41), 4093–4104.

Singh, A., Mao, H.-k., & ad R.J. Hemley, J. S. (1998). Estimation of single-crystal elastic moduli from polycrystalline x-ray diffraction at high pressure: Application from FeO and iron. *Phys. Rev. Lett.*, *80*, 2157–2160.

Staron, P., Kocak, M., & Williams, S. (2002). Residual stresses in friction stir welded Al sheets. *Appl. Phys.*, *A*, *74*, S1161–2.

Steuwer, A., & Daniels, J. (2011). In-situ stress and strain measurements around cracks using synchrotron X-ray diffraction. *J. Strain Anal.*, *46*, 593–606.

Steuwer, A., Santisteban, J., Turski, M., Witers, P., & Buslaps, T. (2005). High-resolution strain mapping in bulk samples using full-profile analysis of energy dispersive synchrotron X-ray diffraction data. *Nuclear Inst. Methods in Phys. Res. B*, *238*, 200–204.

Suzuki, A., Ohtani, E., & Kamada, T. (2000). A new hydrous phase δ-AlOOH synthesized at 21 GPa and 1000°C. *Phys. Chem. Min.*, *27*, 689–693.

Tamura, N. (2014). XMAS: A versatile tool for analyzing synchrotron x-ray microdiffraction data. In R. Barabash & G. Ice (Eds.), *Strain and Dislocation Gradients from Diffraction* (pp. 125–155). Imperial College Press.

Tamura, N., MacDowell, A., Spolenak, R., Valek, B., Bravman, J., Brown, W., Celestre, R., Padmore, H., Batterman, B., & Patel, J. (2003). Scanning X-ray microdiffraction with submicrometer white beam for strain/stress and orientation mapping in thin films. *J. Synchrotron Rad.*, (10), 137–143.

Taylor, G. (1934a). The mechanism of plastic deformation of crystals. Part I. Theoretical. *Proc. Roy. Soc. of London Series A*, *145*, 362–387.

Taylor, G. (1934b). The mechanism of plastic deformation of crystals. Part II. Comparison with observations. *Proc. Roy. Soc. of London Series A*, *145*, 388–404.

Thompson, E., Campbell, A., & Tsuchiya, J. (2022). Calculated elasticity of Al-bearing phase D. *Minerals*, *12*, 922.

Tsuchiya, J., & Tsuchiya, T. (2009). Elastic properties of δ-AlOOH under pressure: First principles investigation. *Phys. Earth Planet. Int.*, *174*, 122–127.

Tsuchiya, J., Tsuchiya, T., & Tsuneyuki, S. (2005). First-principles study of hydrogen bond symmetrization of phase D under high pressure. *Am. Min.*, *90*, 44–49.

Tsujino, N., Nishihara, Y., Yamazaki, D., Seto, Y., Higo, Y., & Takahashi, E. (2016). Mantle dynamics inferred from the crystallographic preferred orientation of bridgmanite. *Nature*, *539*, 81–84.

Turner, F., Griggs, D., & Heard, H. (1954). Experimental deformation of calcite crystals. *GSA Bulletin*, *65*, 883–934.

Ungar, T., Gubicza, J., Ribarik, G., & Borbely, A. (2001). Crystallite size distribution and dislocation structure determined by diffraction profile analysis: Principles and practical application to cubic and hexagonal crystals. *J. Appl. Cryst.*, *34*, 298–310.

Van der Lee, S., & Nolet, G. (1997). Seismic image of the subducted trailing fragments of the Farallon plate. *Nature*, *386*, 266–269.

Van Puymbroeck, E., Nagy, W., Schotte, K., Ul-Abdin, Z., & DeBacker, H. (2019). Determination of residual stresses in a steel bridge component by finite element modeling of the incremental hold drilling method. *MDPI, Appl. Sci.*, *9*, 536.

Vernooij, M., & Langenhorst, F. (2005). Experimental reproduction of tectonic deformation lamellae in quartz and comparison to shock-induced planar deformation features. *Meteoritics Planetary Sci.*, *40*, 1353–1361.

Wang, B., Zhang, Y., Fu, S., Yan, W., Takahashi, E., Li, L., Lin, J.-F., & Song, M. (2022). Single-crystal elasticity of phase Egg $AlSiO_3OH$ and δ-AlOOH by Brillouin spectroscopy. *Am. Min.*, *107*, 147–152.

Wang, F., Men, X., Liu, Y., & Fu, X. (2020). Experiment and simulation on influence of ultrasonic rolling parameters on residual stress of Ti-6Al-4V alloy. *Simulation Modelling Practice and Theory*, *104*, 102121.

Wang, Y., & Wen, L. (2007). Geometry and P and S velocity structure of the "African Anomaly". *J. Geophys. Res.*, *112*, B05313.

Wenk, H.-R., Chandler, B., Chen, K., Tamura, N., & Yu, R. (2020). Residual lattice strain in quartzites as a potential palaeo-piezometer. *Geophys. J. Int.*, *222*, 1363–1378.

Wenk, H., Cottaar, S., Tomé, C., McNamara, A., & Romanowicz, B. (2011). Deformation in the lowermost mantle: From polycrystal plasticity to seismic anisotropy. *Earth. Planet. Sci. Lett.*, *306*, 33–45.

Wenk, H.-R., Lonardelli, I., Merkel, S., Miyagi, L., Pehl, J., Speziale, S., & Tommaseo, C. (2006a). Deformation textures produced in diamond anvil experiments, analyzed in radial diffraction geometry. *J. Phys.: Condensed Matter*, *18*, S933–S947.

Wenk, H.-R., Lonardelli, I., Pehl, J., Devine, J., Prakapenka, V., Shen, G., & Mao, H.-K. (2004). In situ observation of texture development in olivine, ringwoodite,

magnesiowustite and silicate perovskite at high pressure. *Earth. Planet. Sci. Lett.*, *226*, 507–519.

Wenk, H.-R., Lutterotti, L., Kaercher, P., Kanitpanyacharoen, W., Miyagi, L., & Vasin, R. (2014). Rietveld texture analysis from synchrotron diffraction images. II. Complex multiphase materials and diamond anvil cell experiments. *Powd. Diff.*, *29*, 507–519.

Wenk, H.-R., Matthies, S., Donovan, J., & Chateigner, D. (1998). BEARTEX: A Windows-based program system for quantitative texture analysis. *J. Appl. Cryst.*, *31*, 262–269.

Wenk, H.-R., Matthies, S., Hemley, R., Mao, H.-k., & Shu, J. (2000). The plastic deformation of iron at pressures of the Earth's inner core. *Nature*, *405*, 1044–1047.

Wenk, H.-R., Rybacki, E., Dresen, G., Lonardelli, I., Barton, N., Franz, H., & Gonzalez, G. (2006b). Dauphiné twinning and texture memory in polycrystalline quartz. Part 1: Experimental deformation of novaculite. *Phys. Chem. Minerals*, *33*, 667–676.

Williams, D., & Evans, A. (1973). A simple method for studying slow crack growth. *J. Testing and Evaluation*, *1*, 264–270.

Withers, P. (2015). Fracture mechanics by three-dimensional crack-tip synchrotron X-ray microscopy. *Phil. Trans. R. Soc. A*, *373*, 20130157.

Withers, P., & Webster, P. (2001). Neutron and synchrotron X-ray strain scanning. *Strain*, *37*, 19–31.

Wookey, J., Kendall, J.-M., & Barruol, G. (2002). Mid-mantle deformation inferred from seismic anisotropy. *Nature*, *415*, 777–780.

Yang, H., Prewitt, C., & Frost, D. (1997). Crystal structure of the dense hydrous magnesium silicate, phase D. *Am. Min.*, *82*, 651–654.

Zaefferer, S. (2003). A study of active deformation systems in titanium alloys: Dependence on alloy composition and correlation with deformation texture. *Mat. Sci. Eng.*, *A3444*, 20–30.